

A SUPERDARN STUDY OF STEADY  
MAGNETOSPHERIC CONVECTION

A Thesis Submitted to the  
College of Graduate Studies and Research  
in Partial Fulfillment of the Requirements  
for the degree of Master of Science  
in the Institute of Space and Atmospheric Studies of Physics  
University of Saskatchewan  
Saskatoon

By  
Jeffrey Bruce Pfeifer

©Jeffrey Bruce Pfeifer, July/2008. All rights reserved.

# PERMISSION TO USE

In presenting this thesis in partial fulfilment of the requirements for a Post-graduate degree from the University of Saskatchewan, I agree that the Libraries of this University may make it freely available for inspection. I further agree that permission for copying of this thesis in any manner, in whole or in part, for scholarly purposes may be granted by the professor or professors who supervised my thesis work or, in their absence, by the Head of the Department or the Dean of the College in which my thesis work was done. It is understood that any copying or publication or use of this thesis or parts thereof for financial gain shall not be allowed without my written permission. It is also understood that due recognition shall be given to me and to the University of Saskatchewan in any scholarly use which may be made of any material in my thesis.

Requests for permission to copy or to make other use of material in this thesis in whole or part should be addressed to:

Head of the Department of Physics and Engineering Physics

116 Science Place

University of Saskatchewan

Saskatoon, Saskatchewan

Canada

S7N 5E3

# ABSTRACT

Intervals of Steady Magnetospheric Convection (SMC) are loosely defined as times when convection in the magnetosphere as a whole is enhanced and there are no substorm signatures. A lack of substorm signatures implies that the large scale structure of the magnetotail is maintained. There have been several quantitative methods developed to detect SMC events. None of these methods are based on observations of convection. The Super Dual Auroral Radar Network (SuperDARN) is a useful tool for studying SMC, because it gives a direct measurement of convection on a global scale.

Previous SMC selection methods have made use of ground based magnetometer responses to auroral currents in the atmosphere. These methods resulted in a strong seasonal dependence in SMC occurrence due to seasonal changes in ionospheric conductivity.

A new SMC selection criterion was developed to improve upon the previous criteria. This new method identifies all the events found using currently accepted methods plus additional intervals that reduce the seasonal dependence in SMC occurrence. SuperDARN was used to evaluate the old and new selection methods. According to SuperDARN convection observations, the new SMC selection criterion largely eliminated ionospheric conductivity effects. A conceptual model of the conductivity effects on the traditional SMC selection method was developed, and the occurrence of modelled SMC events agrees well with observations.

Statistical studies have revealed that the additional SMC intervals have similar properties as events selected using traditional methods. Case studies confirmed the statistical results that SMCs selected by the new criterion have SMC properties. Both SMC events sets have a moderate solar wind driver, enhanced convection, and stable polar cap size. Statistical studies have also shown there was good SuperDARN data coverage during SMC, which is not typical of SuperDARN observations during

enhanced and disturbed conditions in the magnetosphere. It is therefore shown to be an excellent tool with which to study SMC.

# ACKNOWLEDGEMENTS

Typically, people at least thank their supervisor so “props” go to Kathryn McWilliams for knowing what’s going on, because for a long time I didn’t.

Besides the support provided by Kathryn, this thesis would not have been possible without the following individuals, Chad Bryant, Wilson Brenna, Paul and Eddie Kulyk, Robin Barnes, and last but not least Bob McPherron.

Funding for this research was provided by an NSERC Discovery Grant and NSERC CRO fund for the Canadian SuperDARN Program. I would also like to express gratitude to the WDC-C2 Kyoto AE index service for providing AE index data, the National Geophysical Data Center for providing GOES data, and the Coordinated Data Analysis Web for providing ACE data.

This thesis is for my folks, because they've put up with me for longer than anyone.

# CONTENTS

<b>Permission to Use</b>	<b>i</b>
<b>Abstract</b>	<b>ii</b>
<b>Acknowledgements</b>	<b>iv</b>
<b>Contents</b>	<b>vi</b>
<b>List of Figures</b>	<b>viii</b>
<b>1 General Introduction</b>	<b>1</b>
1.1 Objectives . . . . .	1
1.2 The Solar Wind and the Magnetosphere . . . . .	2
1.3 Thesis Outline . . . . .	9
<b>2 Magnetospheric Dynamics</b>	<b>12</b>
2.1 Magnetospheric Convection . . . . .	12
2.2 Convection States of the Magnetosphere . . . . .	18
2.2.1 Substorms . . . . .	18
2.2.2 Sawtooth Events . . . . .	21
2.2.3 Steady Magnetospheric Convection . . . . .	22
<b>3 The Ionosphere</b>	<b>25</b>
3.1 Introduction . . . . .	25
3.2 The Neutral Atmosphere . . . . .	26
3.3 The Ionosphere . . . . .	27
3.4 Electrical Conductivity in the Ionosphere . . . . .	32
3.5 Regions of the Ionosphere . . . . .	38
<b>4 Ionospheric and Magnetospheric Convection</b>	<b>41</b>
4.1 Observational Techniques . . . . .	41
4.1.1 Auroral Electrojet Indices . . . . .	41
4.1.2 SuperDARN . . . . .	44
4.2 Previous SMC Results . . . . .	48
<b>5 Evaluation of SMC Selection Methods</b>	<b>53</b>
5.1 AE Solar Cycle Dependence . . . . .	54
5.2 AE Dependence on Season . . . . .	55
5.3 Improving SMC Selection Criteria . . . . .	57
5.4 SuperDARN and Seasonal Effects On SMC . . . . .	62

5.5	Conceptual Model of Conductivity Effects on SMC Selection . . . . .	67
<b>6</b>	<b>Statistical Studies of SMC</b>	<b>78</b>
6.1	Superposed Epoch Study . . . . .	78
6.1.1	Interplanetary Magnetic Field Conditions . . . . .	79
6.1.2	Convection Electric Field and Transpolar Voltage . . . . .	82
6.1.3	SuperDARN Data Coverage . . . . .	87
6.2	Scatter Plot Study of Association Between SMC Parameters . . . . .	89
6.2.1	IMF Conditions . . . . .	89
6.2.2	Polar Cap Voltage and Electric Field Values . . . . .	91
6.3	Statistical Study Summary . . . . .	95
<b>7</b>	<b>SMC Case Study</b>	<b>96</b>
7.1	SMC Case Study 1: October 20, 2001 . . . . .	97
7.2	SMC Case Study 2: October 30, 2001 . . . . .	107
7.3	Sawtooth Case Study: October 21, 2001 . . . . .	116
7.4	Case Study Results . . . . .	125
<b>8</b>	<b>Conclusion and Future Work</b>	<b>126</b>
8.1	Summary . . . . .	126
8.2	Future Work . . . . .	133

# LIST OF FIGURES

1.1	Regions of the magnetosphere . . . . .	3
2.1	The IMF and neutral current sheet. . . . .	13
2.2	The convection cycle. . . . .	15
2.3	Magnetic reconnection for different IMF By orientations. . . . .	17
2.4	Idealised northern hemisphere ionospheric convection patterns for different IMF By orientations. . . . .	18
2.5	Seasonal variation of the geomagnetic $aa$ and $aa_m$ indices. . . . .	19
2.6	The different phases of a substorm as seen in the visible aurora . . . . .	20
3.1	An example of an ionospheric equipotential contours in the northern hemisphere from SuperDARN. . . . .	26
3.2	Modelled electron density as a function of height. . . . .	28
3.3	The flat earth approximation. . . . .	29
3.4	The coordinate system for the magnetic and electric fields in the ionosphere for the high latitude case. . . . .	34
3.5	Ionospheric conductivity as a function of height. . . . .	37
3.6	Three cases of charged particle motion in the ionosphere in the presence of electromagnetic fields and collisions. . . . .	39
4.1	The auroral electrojet currents. . . . .	42
4.2	The location of the magnetometers used to derive the AE indices. . . . .	43
4.3	SuperDARN radar coverage. . . . .	44
4.4	Line of site SuperDARN data and the corresponding convection map. . . . .	47
5.1	Yearly number of SMC events compared to the yearly number of sunspots observed. . . . .	54
5.2	Occurrence of SMC events for each month for available years from 1966 to 2001 selected with $AE \geq 200$ nT. . . . .	56
5.3	The total distribution of SMC events selected using the constant AE cutoff of 200 nT. . . . .	57
5.4	The brute force comparison of variable SMC selection methods. . . . .	59
5.5	An example of AE data with reasonable baseline adjustment and an example of AE data with baseline errors. . . . .	61
5.6	Occurance of SMC events per month for $AE \geq 200$ nT and Equation 5.2. . . . .	63
5.7	Total distribution of SMC events for $AE \geq 200$ nT and Equation 5.2. . . . .	64
5.8	Average interval values of SuperDARN PCPD for several data sets. . . . .	65
5.9	The geometry of the Sun-Earth system in spherical coordinates. . . . .	68
5.10	Comparison of the conceptual model to experimental data. . . . .	74
5.11	The number of magnetometer pairs that contribute over 3 hours to the AE index. . . . .	76

6.1	Cumulative distributions of IMF Bz as a function of superposed epoch time. . . . .	79
6.2	Cumulative distributions of IMF By as a function of superposed epoch time. . . . .	81
6.3	Cumulative distributions of PCPD as a function of superposed epoch time. . . . .	83
6.4	Cumulative distributions of the convection electric field as a function of superposed epoch time. . . . .	84
6.5	Cumulative distributions of the distance between voltage extrema as a function of superposed epoch time. . . . .	86
6.6	Cumulative distributions of the SuperDARN data points as a function of superposed epoch time. . . . .	88
6.7	Scatter plots of IMF By verses IMF Bz. . . . .	90
6.8	Scatter plots of PCPD verses IMF Bz. . . . .	92
6.9	Scatter plots of PCPD verses distance between voltage extrema. . . . .	93
6.10	Scatter plots of convection electric field verses IMF Bz. . . . .	94
7.1	The AE indices for October 20, 2001. . . . .	98
7.2	Auroral image obtained from the IMAGE satellite by WIC with the shaded region indicating the estimated polar cap area. . . . .	99
7.3	The polar cap area and corresponding keograms for October 20, 2001. . . . .	101
7.4	The IMF components for October 20, 2001. . . . .	104
7.5	Solar wind properties for October 20, 2001. . . . .	105
7.6	Properties of the SuperDARN convection maps for October 20, 2001. . . . .	106
7.7	The AE indices for October 30, 2001. . . . .	108
7.8	The polar cap area and corresponding keograms for October 30, 2001. . . . .	109
7.9	The IMF components for October 30, 2001. . . . .	111
7.10	The solar wind properties for October 30, 2001. . . . .	112
7.11	Properties of the SuperDARN convection maps for October 30, 2001. . . . .	114
7.12	The northward magnetic field component measured at the GOES-8 and GOES-10 satellites on October 30, 2001. . . . .	115
7.13	The AE indices for October 21, 2001. . . . .	117
7.14	The polar cap area and corresponding keograms for October 21, 2001. . . . .	118
7.15	Solar wind properties for October 21, 2001. . . . .	119
7.16	The IMF components for October 21, 2001. . . . .	121
7.17	The northward magnetic field component measured at the GOES-8 and GOES-10 satellites on October 21, 2001. . . . .	122
7.18	Properties of the SuperDARN convection maps for October 21, 2001. . . . .	124

# CHAPTER 1

## GENERAL INTRODUCTION

### 1.1 Objectives

The fundamental objective of near-Earth space science has been to understand the dynamics of the magnetosphere. Space weather, like surface weather, can have a profound effect on human activity. These effects can be negative, as in the case of magnetic storms which can destroy satellites, disrupt radio communications, and damage power grids. If one had the ability to forecast the occurrence of such storms, preventative measures could be taken to minimise the damage.

Unravelling magnetospheric dynamics is not easy. The magnetosphere is strongly influenced by the solar wind, which has a highly variable plasma density, plasma velocity, and magnetic field. In addition to external variability, processes intrinsic to the magnetosphere make predictions about its state a daunting task. The most fundamental questions regarding the dynamics of the magnetosphere are related to its stability. Is a stable configuration possible? What conditions lead to stability? What characterises stability? Answering these questions would greatly improve the understanding of magnetospheric dynamics.

Stability in the magnetosphere can occur and can take two forms: a quiescent state with little activity and a state of dynamic equilibrium where the magnetosphere is active and steady. The special case of active but stable magnetospheric convection (e.g., *Pytte et al. (1978)* and *Sergeev et al. (1995)*) is the focus of the research presented in this thesis.

## 1.2 The Solar Wind and the Magnetosphere

The solar wind, which flows outward from the Sun, is a plasma composed mainly of hydrogen ions and helium ions at a number density ratio of 20:1 (*Hundhausen, 1995*). The solar wind moves at speeds typically of the order of  $400 \text{ km s}^{-1}$  (*Gonzalez et al., 1999*). Along with the protons and alpha particles that make up the solar wind, there are enough electrons that the solar wind is electrically neutral. *Parker (1958)* suggested that the solar wind is formed by the steady expansion of the solar corona and demonstrated that this was mathematically possible. *Parker (1958)* used pressure balance arguments showing that the outward force of the plasma pressure gradient was larger than the inward pull of the Sun's gravity. With this conjecture, *Parker (1958)* was successful in showing that the solar wind flow is also supersonic at distance of  $1.5 \times 10^{11} \text{ m}$  from the Sun. The Explorer 10 spacecraft later verified that the solar wind was indeed supersonic (*Bonetti et al., 1963*).

As this supersonic plasma propagates away from the Sun it carries with it the magnetic field of the Sun. In the solar system the Sun's magnetic field is referred to as the interplanetary magnetic field, or IMF, and it has a typical magnitude of about  $5 \text{ nT}$  (*Gonzalez et al., 1999*). The IMF is bound to the solar wind according to Faraday's Law, which states that changing the magnetic flux passing through a conductor will induce a voltage. The solar wind is a nearly perfect conductor and will not support an ambient electric field. This means the magnetic flux through a given volume of solar wind plasma will remain constant. So as a parcel of solar wind plasma propagates, to ensure constant magnetic flux, the IMF is carried along. This is referred to as the "frozen-in" approximation, because each IMF field line acts as if it were frozen to the parcel of solar wind plasma it permeates.

Like the Sun, the Earth has a magnetic field. The Earth's dipolar magnetic field is tilted with respect to the geographic pole. The south pole of the magnetic dipole is located in the Canadian high Arctic, near the geographic North Pole. At the Earth's surface the magnetic field strength is about  $50 \mu\text{T}$ , and in the equatorial plane of the Earth the planetary field points in the northward direction.

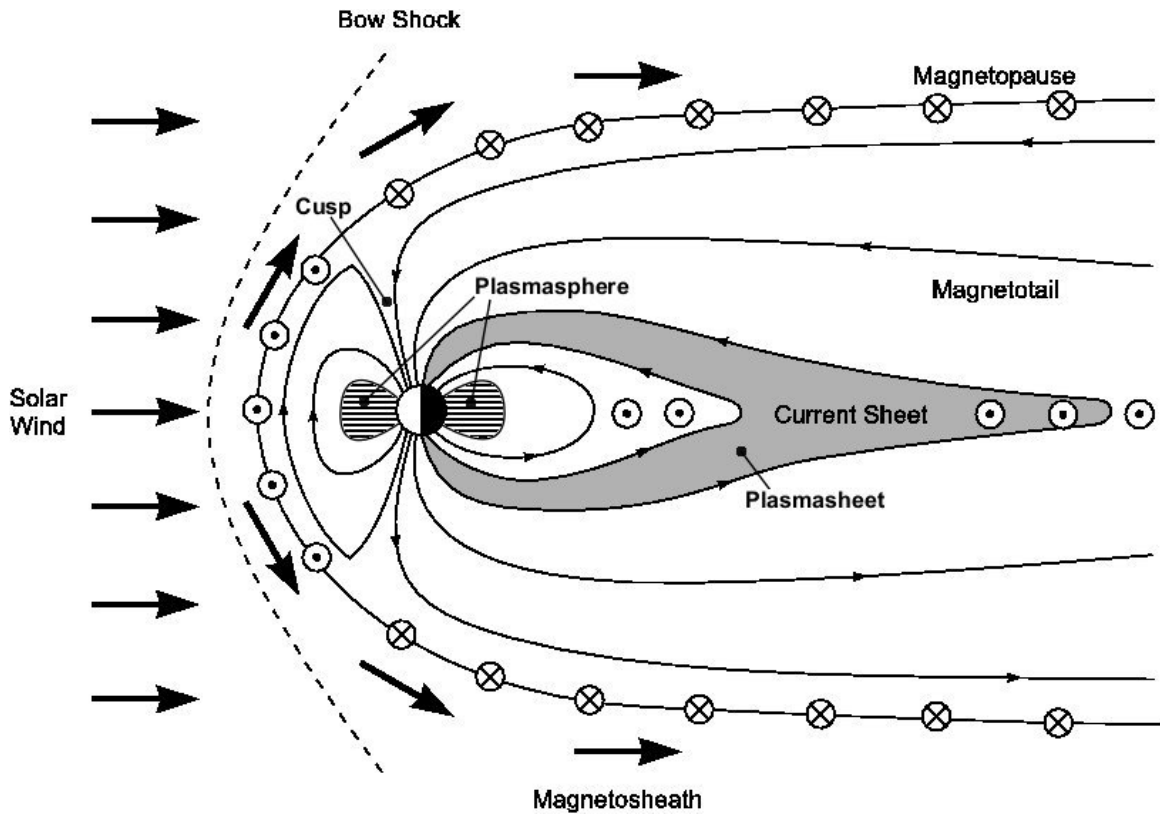


**Figure 1.1:** Regions of the magnetosphere as adapted from *Hughes* (1995). The different regions of the magnetosphere are shown. Currents flowing out of the plane of this image are represented by circled dots, and inward currents circled crosses.

The solar wind and IMF encounter the planetary magnetic field. In the absence of the solar wind the Earth’s magnetic field is mainly dipolar. The Earth’s magnetic field acts as an obstacle to the solar wind, so the IMF and the planetary field are deformed. According to the “frozen-in” approximation, the solar wind and the plasma of the Earth’s magnetic field cannot mix, because the plasma cannot flow across the magnetic field lines. The Lorentz force acts on the solar wind plasma to oppose the bending of the IMF field lines. Therefore the solar wind-IMF combination exerts a dynamic pressure on the magnetosphere, compressing the planetary field lines on the dayside. The dynamic pressure of the solar wind will balance the magnetic pressure of the planetary field. Satellite measurements, reveal that, on average, the sunward boundary of the magnetosphere is located about 10 Earth radii upstream of the Earth (*Bonetti et al.*, 1963).

The solar wind is deflected by the planetary magnetic field forming a bowshock upstream of the magnetopause. It is roughly symmetrical about a line that runs from the Earth to the Sun. The plasma that flows between the bow shock and the magnetopause is referred to as magnetosheath plasma. Near the dayside magnetopause the magnetosheath plasma has a density of the order of  $10 \text{ cm}^{-3}$ , and the magnetic field has a strength of about 15 nT. The ions in the region typically have energies of 150 eV (*Hughes, 1995*).

The boundary between the IMF and the planetary magnetic field is called the magnetopause. In this region currents must flow according to Ampère’s Law. These magnetopause currents serve to support the geometry of the deformed IMF and planetary magnetic fields. On the dayside of the magnetosphere the magnetopause current flows from dawn to dusk. On the nightside of the magnetopause the currents flow from dusk to dawn. These currents are illustrated along the magnetopause in Figure 1.1 which represents a dusk side view of the magnetosphere. The duskward currents (circled dots) along the front side of the magnetopause serve to support the compression of the dayside magnetosphere while dawnward surface currents further down stream (circled crosses) contribute to supporting the magnetotail structure. Figure 1.1 is not to scale, but does illustrate schematically the regions and currents of the magnetosphere.

The “frozen-in” approximation implies that the solar wind and the magnetosphere interact only in a minimal way. In this closed magnetosphere some energy, mass, and momentum can be exchanged through viscous interaction with the solar wind. Viscous interaction involves the transfer of momentum from the solar wind to just inside the magnetosphere. There is still much debate as to what role the viscous interaction plays in driving the magnetosphere (*Farrugia et al., 2001*).

*Dungey (1961)* presented a different hypothesis of solar wind-magnetosphere coupling that could occur if the frozen-in approximation were to break down. The hypothesis allows the IMF magnetic field to merge with the planetary field. In this open system, the IMF is connected to the magnetic field of the planet, so a significant amount of mass, momentum, and energy from the solar wind can enter the magneto-

sphere. This constitutes the second way in which mass, energy, and momentum can be transferred from the solar wind into the magnetosphere. Many ground-based and satellite observations have been interpreted as signatures of magnetic reconnection (e.g., *McWilliams et al.*, 2004).

If the IMF is southward, magnetic reconnection with the northward planetary field can occur on the dayside of the Earth. After reconnection a field line is created that is neither entirely an IMF field line nor entirely a magnetospheric field line. It is called an open field line, because it is part of the planetary magnetic field but does not close itself inside the Earth; rather is connected to the IMF. Solar wind particles that were originally confined to IMF can now flow into the magnetosphere on these open field lines. Entry of the solar wind into the magnetosphere is most direct in the cusp region (e.g., *Fritz and Zong*, 2005).

The open field lines that result from the reconnection process are drawn by the solar wind across the northern and southern polar regions. These open flux tubes continue to flow behind the Earth to form a long tail, which is referred to as the magnetotail. The lobes of the magnetotail have a field strength of about 20 nT. The magnetotail acts as a reservoir of magnetic energy and plasma in the magnetosphere. The length of the tail can be estimated based on the speed of the solar wind and the time that a given flux tube remains open. It is estimated that the magnetotail has a length of several hundred Earth radii (*Hughes*, 1995). In the northern portion of the tail the magnetic field is directed toward the Earth, while in the southern portion it is directed away from the Earth. These two magnetic lobes, as they are called, are separated by the plasma sheet. The plasma concentration in the lobes of the magnetotail is of the order of  $0.01 \text{ cm}^{-3}$ , and the ions have energies of 300 eV (*Hughes*, 1995).

The plasma sheet is a region in the equatorial plane of the magnetotail with higher concentrations, of the order of  $0.1 \text{ cm}^{-3}$ , and with ion energies about 5 keV. The field strength in the central plasma sheet is of the order of 10 nT (*Hughes*, 1995). In the equatorial plane the cross tail current sheet flows from dawn to dusk through the central plasma sheet, as illustrated in Figure 1.1. This duskward current closes

the dawnward magnetopause currents on the nightside, forming a double solenoid current configuration. It is this night side current system that serves to support the nearly anti-parallel magnetic fields of the north and south tail lobes.

Closer to the Earth in regions of more dipolar closed field lines exists the plasmasphere, which co-rotates with the Earth. The plasmasphere is identified in Figure 1.1. This doughnut-shaped region is populated by plasma primarily of ionospheric origin (*Hughes, 1995*). The particle density here is much higher than in other regions of the magnetosphere because the field lines in the plasmasphere are perpetually closed. The plasma concentration is of the order of  $10^3 \text{ cm}^{-3}$ , and particles energies are of the order of 1 eV (*Hughes, 1995*).

As magnetospheric field lines were opened on the dayside by reconnection with the IMF, so they must be closed. Open field lines can close in the magnetotail because the magnetic field in the north and south tail lobes points in opposite directions. When the frozen-in approximation once again breaks down, the open field lines in the magnetotail merge to form closed field lines connected to the Earth and IMF field lines downstream of the Earth. The tension on the highly stretched and newly closed field lines in the magnetotail causes them, along with the associated frozen-in plasma, to slingshot back towards the Earth. Much of this plasma precipitates into the Earth's upper atmosphere, imparting energy to the atoms and molecules there. These excited upper atmospheric particles release energy as photons to create the aurora.

The merged field lines that close in the magnetotail convect towards the Earth and then progress around to the dayside magnetosphere where the reconnection process can begin anew. The process of magnetic field reconnection is cyclic in nature, with geomagnetic field lines being connected to and disconnected from the IMF. This reconnection transport process is called magnetospheric convection, and it can occur in several distinct ways.

The progression of the convection cycle is always the same. The IMF merges with the planetary field on the dayside. Magnetic energy is stored in the magnetotail and eventually this energy is released through reconnection in the magnetotail. How

this energy is released defines the mode of convection. It can occur in a relatively steady fashion, but more often it happens explosively when the convection cycle becomes unstable. The unstable modes are referred to as substorms and sawtooth events. A substorm occurs when the open field lines that have gradually accumulated in the magnetotail rapidly merge, leading to an explosive release of the stored energy. This catastrophic release is referred to as the onset of the expansion phase of a substorm and is observed as a brightening of the aurora. The second unstable convection mode, sawtooth, is similar to the first. Sawtooth events are series of semi-periodic substorms that result when the IMF remains strongly southward for long periods of time (*Henderson et al.*, 2006). They are referred to as sawtooth events because plots of the large amplitude oscillations of energetic particle fluxes observed at geosynchronous orbit resemble sawblades. Both unstable convection modes result in a large scale reconfiguration of the magnetotail. When reconnection rates on the dayside are balanced by the reconnection rates in the magnetotail, a stable mode of convection is achieved. This stable convection mode was originally referred to as a convection bay (*Pytte et al.*, 1978), and it is now commonly referred to as steady magnetospheric convection (SMC) (*Sergeev et al.*, 1995). It has been found that SMC results from solar wind conditions similar to but somewhat more moderate than those causing sawtooth events. The difference is believed to be that during sawtooth events the magnetosphere is too strongly driven to dissipate energy in a steady fashion (*Henderson et al.*, 2006).

Studying magnetospheric convection on a large scale can be difficult due to the large size of the magnetosphere. Fortunately, the ionosphere is coupled to the magnetosphere through the Earth's magnetic field (e.g., *Wolf*, 1995). Due to this coupling, one can observe the convection cycle in the ionosphere and from that develop a picture of convection in the magnetosphere. This is highly advantageous since the dimensions of the ionosphere are much smaller, and ground based instruments can be more easily deployed to observe ionospheric convection.

The ionosphere is an electrically conducting layer that exists in the Earth's upper atmosphere. This charged layer is the region of the magnetosphere closest

to the Earth and is mainly produced by photo-ionisation, which is the process by which light from the Sun ionises the neutral atmosphere. There are three regions of the ionosphere that are distinguished from each other by their chemical and physical properties, such as plasma number density, collision frequency, and conductivity. The deepest layer is called the D region and exists from roughly 50 km to 90 km. The middle ionospheric layer is called the E region and is roughly from 90 - 150 km altitude. The final region is referred to as the F region and exists above 150 km altitude.

The production of plasma in the ionosphere is highly dependent on the amount of solar radiation present. Therefore, substantial variations in the plasma density can occur on many different time scales. The variation due to the Earth's daily rotation leads to low plasma density in the nightside ionosphere in comparison to the higher densities in the daylight hours. Variations also occur on the yearly scale, because the Earth's axis of rotation has a tilt with respect to the plane of its orbit. During summer months the plasma number density is enhanced in the summer hemisphere. Since ionospheric conductivity is dependent on the plasma density, variations in charged particle content cause conductivity variations.

Dynamics in the ionosphere are strongly controlled by electromagnetic effects due to magnetospheric convection. Collisions between plasma particles and neutral particles also play a large role in influencing particle motion in the ionosphere. In the F region, which exists at the highest altitude in the ionosphere, collisions are negligible and therefore both ions and electrons are magnetically controlled. In the E region the neutral density has increased to the point where ions will endure far more collisions. Ion motion here is controlled by collisions, while electrons are still controlled by the electric and magnetic fields that permeate the ionosphere. This discrepancy in ion-electron motion results in E-region currents, which depend heavily on the amount of convection in the magnetosphere. These currents depend not only on the convection-induced electromagnetic forces present in the ionosphere but on ionospheric conductivity as well. Because of this, variations in ionospheric conductivity can affect the magnitude of these currents. Magnetometer arrays are

often deployed on the surface to measure these currents.

This introduction has touched only briefly on the complexities of magnetospheric and ionospheric dynamics, providing the groundwork for understanding the research presented in this thesis.

## 1.3 Thesis Outline

Qualitatively Steady Magnetospheric Convection (SMC) has been defined as times where convection is enhanced and there are no substorm signatures. This simple qualitative definition has yet to be translated into a robust quantitative definition. Several methods have been developed to identify SMC but none have been universally accepted in the space science community. These methods all have one underlying problem: none are based on actual convection measurements. Instead these methods rely on phenomena related to SMC to identify events. Direct convection measurements would greatly improve quantitative SMC definitions. The SuperDARN radar network directly measures convection in the ionosphere on a global scale and would be an appropriate tool for studying SMC. SuperDARN convection measurements will make it possible to address the two most important questions about SMC: (1) do the quantitative selection methods currently being used to identify SMC properly identify events with steady enhanced convection, and (2) if these methods are indeed correctly identifying SMC, what convection characteristics define steady convection in the magnetosphere? The research presented in this thesis aims to address these questions.

The physics behind magnetospheric and ionospheric dynamics will be expanded, beginning with a more detailed discussion in Chapter 2 of convection in the magnetosphere. The IMF will be discussed in the context of geomagnetic activity followed by a detailed description of the modes of convection in the magnetosphere: substorms, sawtooth events, and SMC.

Since the ionosphere plays a large role both in SuperDARN measurements and SMC detection, Chapter 3 will be devoted to the processes that give rise to the iono-

sphere. The process of photo-ionisation will be studied with special emphasis placed on how variations in sunlight intensity affect the ambient plasma number density. The details of conductivity are explained for the high latitude ionosphere. The relative drift velocities of the ions and electrons are important for understanding how ionospheric convection and currents are related and used to quantify magnetospheric convection.

The tools used to quantify geomagnetic activity will be presented in Chapter 4. The method by which the Auroral Electrojet indices are derived is explained first, since SMC selection methods based on these indices are the most widely used. A discussion of SuperDARN, a radar network devoted to measuring the drift velocities of plasma in the high latitude ionosphere, follows. The method used to obtain SuperDARN global convection maps is detailed in this section.

In Chapter 5 the SMC definition developed by *O'Brien et al. (2002)* was evaluated. The list of events obtained revealed that this selection method was influenced by not only the amount of magnetospheric activity but also by ionospheric conductivity. SMC is a convection based phenomenon, and therefore in order to take into account the role of ionospheric conductivity a new SMC selection criterion was developed. SuperDARN was used to show that with this new SMC selection method the list of events obtained had been selected with a minimum convection threshold. Additional proof was needed to show the effectiveness of the new SMC selection method. A conceptual model of SMC occurrence based solely on ionospheric conductivity was developed. The results of this model were compared to the experimental results obtained using the method of *O'Brien et al. (2002)*. This comparison between the model and experimental results provided additional evidence that the improved SMC selection method was using a minimum convection threshold.

With an improved SMC selection method, it was important to show these new events satisfied the qualitative criteria of SMC. Chapter 6 contains the first approach, which was statistical in nature and focuses on SuperDARN convection data. This new list of SMC events was found to possess enhanced convection.

A case study of two SMC events is presented in Chapter 7. The purpose of

this work is to compare a traditional SMC event with one that would not previously have been identified as SMC but which the new SMC selection method deems to be SMC. The results of this case study show that the new SMC events do possess steady convection. The case study provided additional insight into magnetospheric activity during SMC not found statistically. A sawtooth event was also included to contrast stable convection with unstable convection.

# CHAPTER 2

## MAGNETOSPHERIC DYNAMICS

### 2.1 Magnetospheric Convection

Magnetospheric convection is driven by magnetospheric reconnection. In Section 1.2 it was suggested that for reconnection to occur on the dayside of the magnetosphere the IMF should be anti-parallel to the Earth's magnetic field. There are many possible scenarios that can lead to reconnection, and the amount and state of convection in the magnetosphere depend heavily on the direction and magnitude of the IMF (e.g., *Ruohoniemi and Baker, 1998*).

The IMF is twisted into an Archimedean spiral which is similar to the streamlines produced by the water ejected from a spinning lawn sprinkler. The Sun is rotating and emitting solar wind plasma with the embedded IMF, analogous to the water emitted by the sprinkler head. Figure 2.1 is an illustration of the process by which the IMF archimedean spiral geometry is formed. Panel (a) of Figure 2.1 is a two dimensional representation of the actual three dimensional structure of the IMF's archimedean spiral and panel (b) displays the neutral current sheet. The solar wind plasma is ejected radially, but the rotation of the Sun leads to a twisting of the frozen-in IMF. This three dimensional structure results because the IMF spiral is ordered in the solar equatorial coordinate system (GSEQ), with field lines being directed out of the Sun in one hemisphere and into the Sun in the opposite hemisphere. The geometry of oppositely directed magnetic field lines is supported by the neutral current sheet which flows between them. This current sheet does not lie perfectly in the solar equatorial plane. Because of this and the rotation of the Sun, undulations form in the neutral current sheet which bear resemblance to a ballerina's

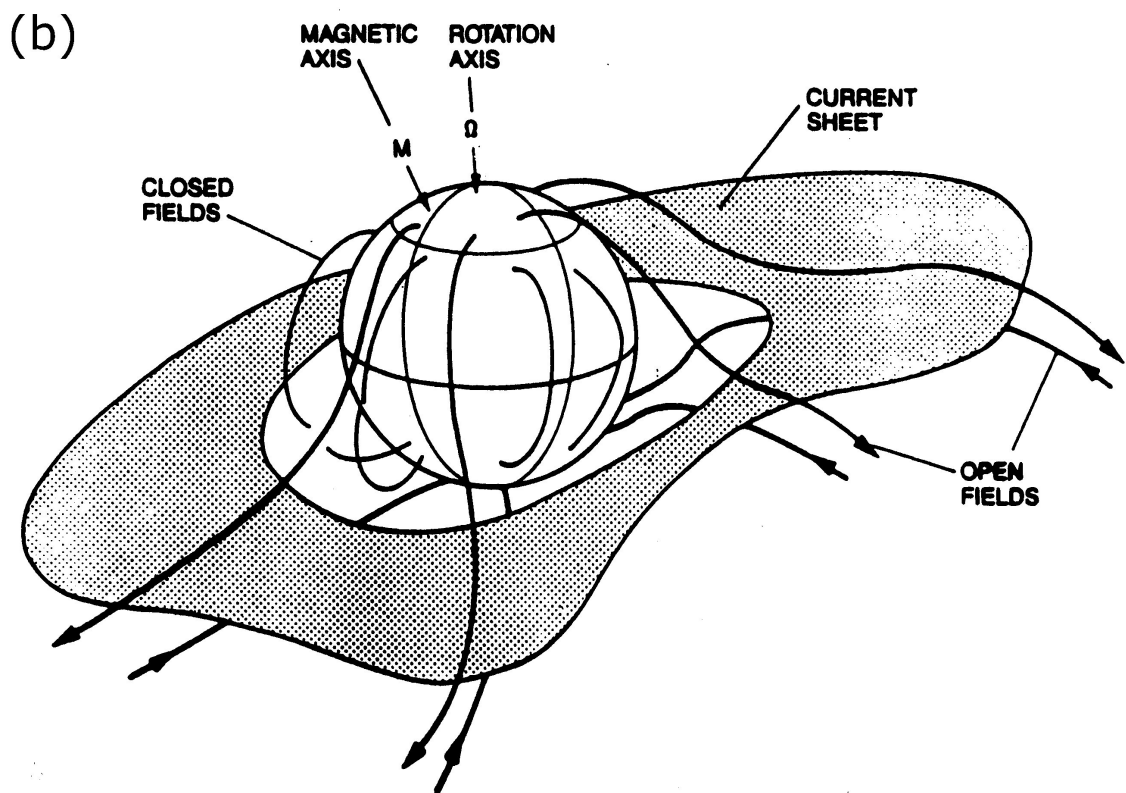
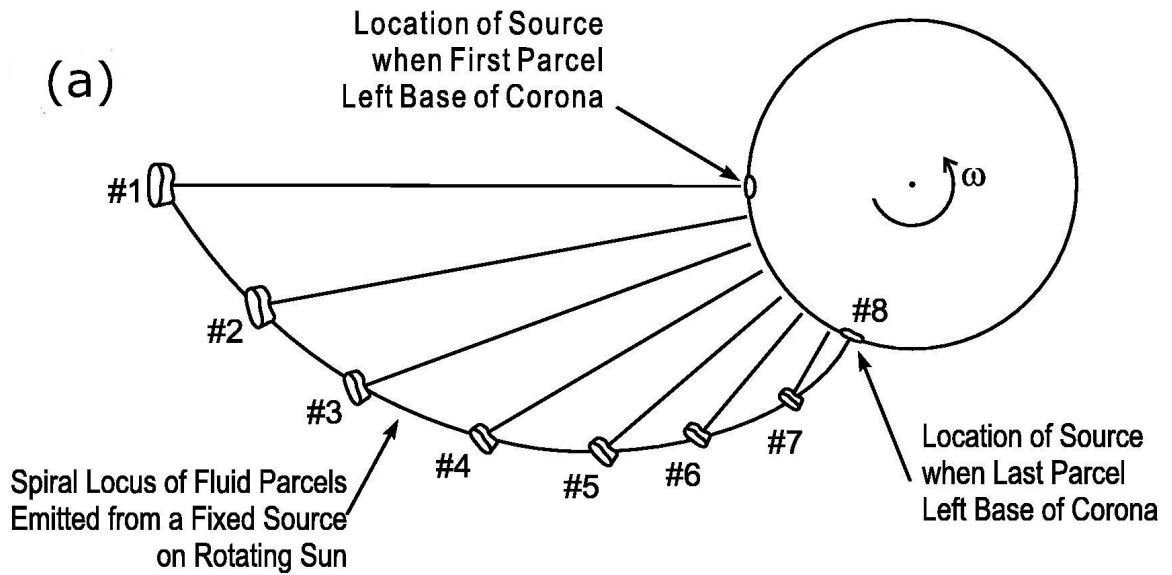


**Figure 2.1:** (a) The loci of plasma parcels emitted radially from the rotating Sun takes the form of an Archimedean spiral (after *Hundhausen, 1995*). (b) Open and closed field lines emanating from the Sun with both the rotational and magnetic axis displayed. The oppositely directed field lines are separated by the neutral current sheet (after *Smith et al., 1978*).

skirt. These undulations give rise to the three dimensional structure of the IMF and can be seen in panel (b) of Figure 2.1.

The direction of the IMF is usually defined with respect to the Geocentric Solar Magnetospheric (GSM) coordinate system (*Russell and McPherron, 1973*). This coordinate system has an  $x$  axis that points from the centre of the Earth toward the Sun and a  $y$  axis is in the Earth's orbital plane. The  $x$  and  $y$  directions are perpendicular by definition. The  $z$  component completes the set right-handed coordinate system such that the north magnetic pole lies in the  $x$ - $z$  plane. A negative IMF  $B_z$  component plays a large role in driving convection but convection is also affected by the IMF  $B_y$  component. Two factors affect convection: (1) magnetic tension on newly reconnected magnetic field lines, and (2) solar wind flow in the magnetosheath, carrying the geomagnetic field lines across the polar cap of the Earth in the anti-sunward direction. When the IMF  $B_y$  component is approximately zero, convection is expected to be symmetric about the line running from the Sun to the Earth. The case of symmetric convection is illustrated in Figure 2.2 with the convection cycle beginning when a southward pointing IMF field line (field line 1') reconnects with the closed, northward pointing field line (field line 1) of the Earth. Numbered field lines 2 to 5 show the anti-sunward flow of the solar wind dragging the open field lines behind the Earth to form the magnetotail. The oppositely directed field lines of the lobes of the magnetotail eventually close (field lines 6 and 6') and then progress back to the dayside (field lines 7, 8, 9). Where each numbered field line maps to in the ionosphere is displayed in the bottom right portion of Figure 2.2. This figure illustrates the basic convection cycle in both the magnetosphere and the ionosphere. Convection is symmetric in the case of Figure 2.2, as both the magnetic tension and the solar wind flow act in the anti-sunward direction. When IMF  $B_y$  is not zero, an asymmetry results in convection. The difference lies in the magnetic tension exerted on the newly opened field line. This tension will no longer act entirely in the anti-sunward direction due to the addition of the IMF  $B_y$  component. The zonal portion of the motion is the result of the highly kinked, newly open field line straightening out, while the subsequent anti-sunward motion over the

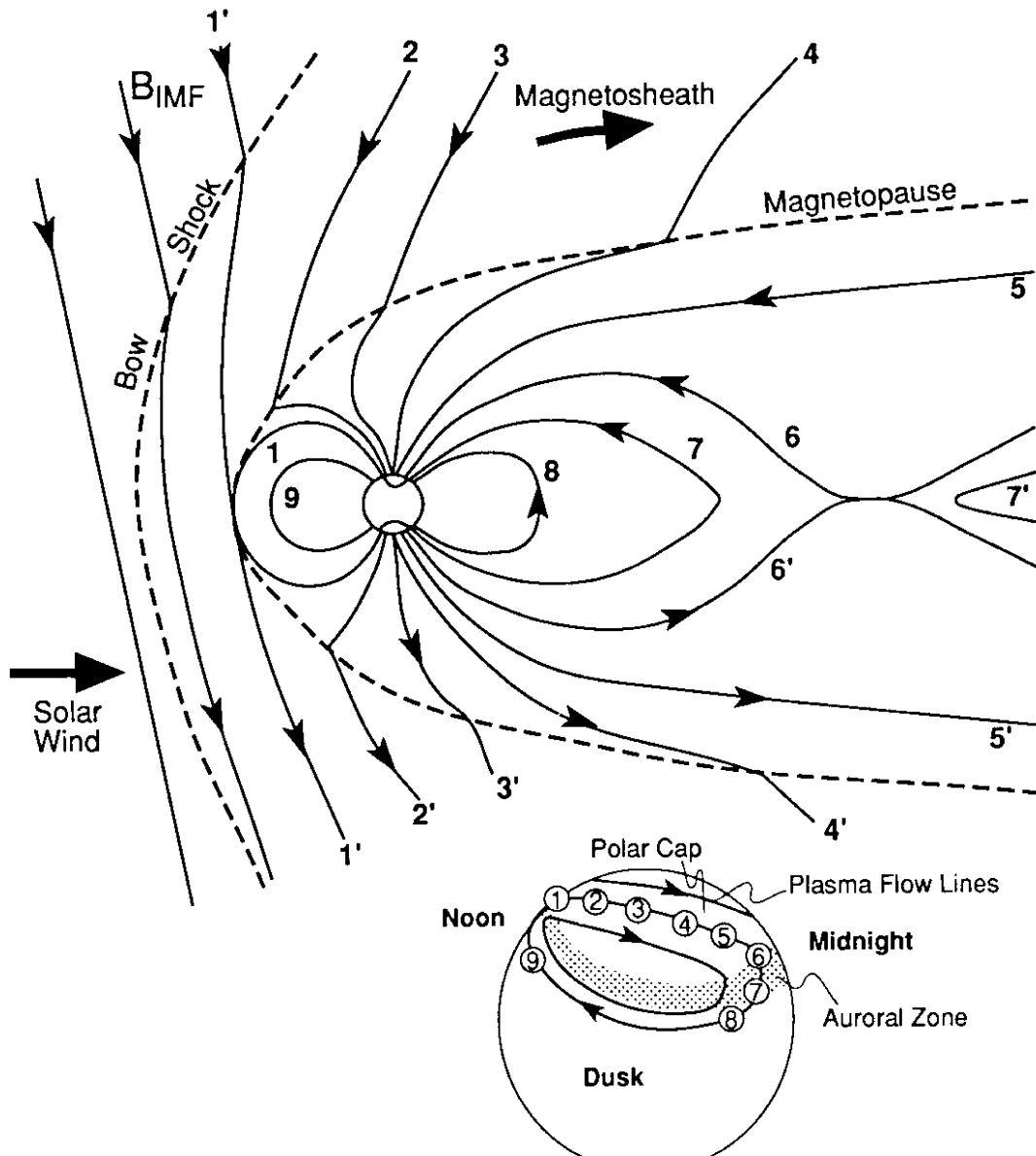


**Figure 2.2:** The numbered field lines indicate the different configurations a geomagnetic field line assumes after reconnection. The bottom right insert of this figure illustrates where each numbered field line maps to in the northern ionosphere (*Hughes, 1995*).

poles is due to convection with the magnetosheath flow. Figure 2.3 illustrates the configuration of newly opened fields on the dayside of the Earth. The open field lines will follow a path that trace out a sickle shape in the ionosphere as they move into and over the polar cap. For positive IMF  $B_y$  the flow near noon is downward in the northern hemisphere. The opposite tension is exerted on newly opened field lines in the southern hemisphere, so the flow in the south will have a strong duskward component when IMF  $B_y$  is positive. The magnetospheric convection cycle generates electric fields that map down to ionospheric heights. These electric fields produce the related ionospheric convection pattern. Figure 2.4 displays the effect that IMF  $B_y$  has on the northern ionospheric convection pattern. Local noon is toward the top of the figure, and the solid lines represent the convection streamlines at ionospheric altitudes. When IMF  $B_y$  is approximately zero (central panel) the symmetric two convection cell pattern is observed. This pattern is symmetric about the noon-midnight meridian. A negative IMF  $B_y$  component (left panel) results in a convection pattern where the flow into the polar cap, is tilted toward dusk. The opposite effect is expected for positive IMF  $B_y$  (right panel).

Reconnection on the dayside of the Earth happens most efficiently when IMF  $B_z$  is negative, but it can also occur when IMF  $B_z$  is positive. There are many possible ways that northward pointing IMF field lines may reconnect to the geomagnetic field on the dayside. Each results in a different form of convection in the magnetosphere (e.g., *Watanabe et al.*, 2007). A common attribute of convection driven by northward IMF is sunward plasma flows at high latitudes in the polar cap. It has been found that this reversed convection can occur for 2-3 hours in a steady state, as long as the IMF is stable (*Huang et al.*, 2000).

It has been shown that the average amount of geomagnetic activity is not constant over the course of the year; rather there is a semi-annual variation that peaks near equinox (*Russell and McPherron*, 1973). Methods to quantify geomagnetic activity commonly employ magnetic field instruments on the Earth's surface. These magnetometers respond to magnetospheric and ionospheric currents. For example, the  $aa$  and  $aa_m$  indices are commonly used to quantify geomagnetic activity (*Delouis*

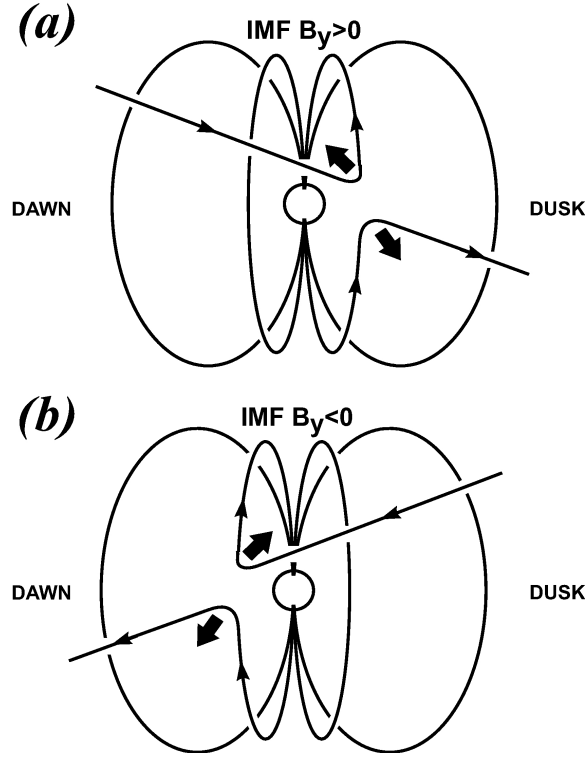


**Figure 2.3:** Magnetic reconnection for (a) positive and (b) negative IMF  $B_y$  orientations, as viewed from the Sun (*Golsing et al., 1990a*).

and *Mayaud, 1975*). Figure 2.5 displays the semi-annual trend in the  $aa$  and  $aa_m$  indices with peaks in geomagnetic activity near equinox (*Svalgaard et al., 2002*).

*Russell and McPherron (1973)* proposed that this semi-annual variation, seen in Figure 2.5, is the result of: (1) the Earth's magnetic field having a tilt with respect to the solar equatorial plane, and (2) the geometry of the IMF which results from the magnetic field of the Sun being twisted into spiral. Due to the dipole tilt of the Earth's magnetic field, there is a systematic variation in the orientation of planetary field with respect to the IMF spiral through out the year. This leads to a varying probability that the IMF and the geomagnetic field will be anti-parallel. *Russell and McPherron (1973)* found that, with respect to the Earth's dipole axis, the IMF  $B_z$  component is more likely to have a negative component near equinox. IMF  $B_z$  plays a large role in driving geomagnetic activity, so it is expected to be higher at equinox.

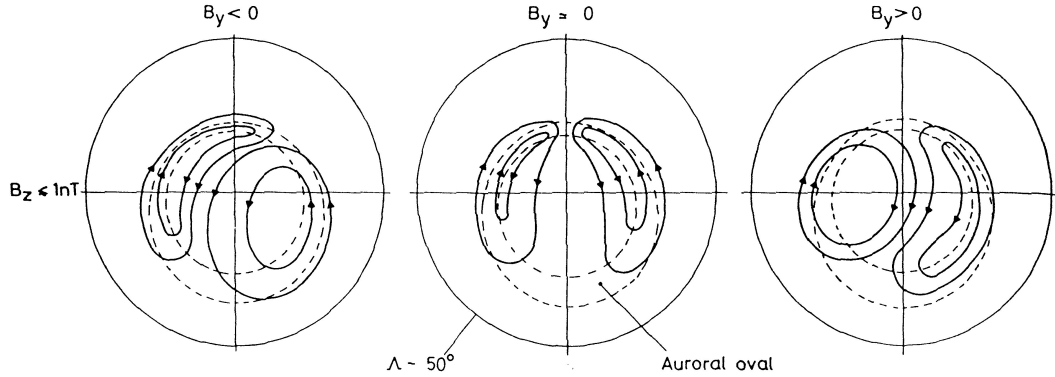


**Figure 2.4:** Idealised northern hemisphere ionospheric convection patterns for different IMF  $B_y$  orientations. The solid lines indicate convection contours. The auroral oval is illustrated by the dashed lines (after Cowley *et al.*, 1991).

## 2.2 Convection States of the Magnetosphere

The convection cycle leads to energy storage and release in the Earth’s magnetosphere. The unloading of energy in the magnetotail may occur in a relatively steady fashion, but more commonly it results in a catastrophic change to the state of the magnetotail. There are three primary ways that energy is released in the magnetotail: (1) substorms, (2) sawtooth events, and (3) steady magnetospheric convection (McPherron *et al.*, 2008).

### 2.2.1 Substorms

Substorms occur when there has been relatively gradual loading of energy in the magnetotail in the form of open flux. This gradual build-up is followed by an explosive release of energy into the magnetosphere. There are three main phases to a substorm: (1) the growth phase (McPherron, 1970), (2) the expansion phase, and (3) the recovery phase (Akasofu, 1964). The development of a substorm in the visible aurora is illustrated in Figure 2.6 (Akasofu, 1964).

Panels A and B of Figure 2.6 illustrate the quiet phase preceding the onset of the substorm. According to McPherron (1970) this quiet phase or growth phase lasts about one hour and begins when the IMF turns southward and magnetospheric

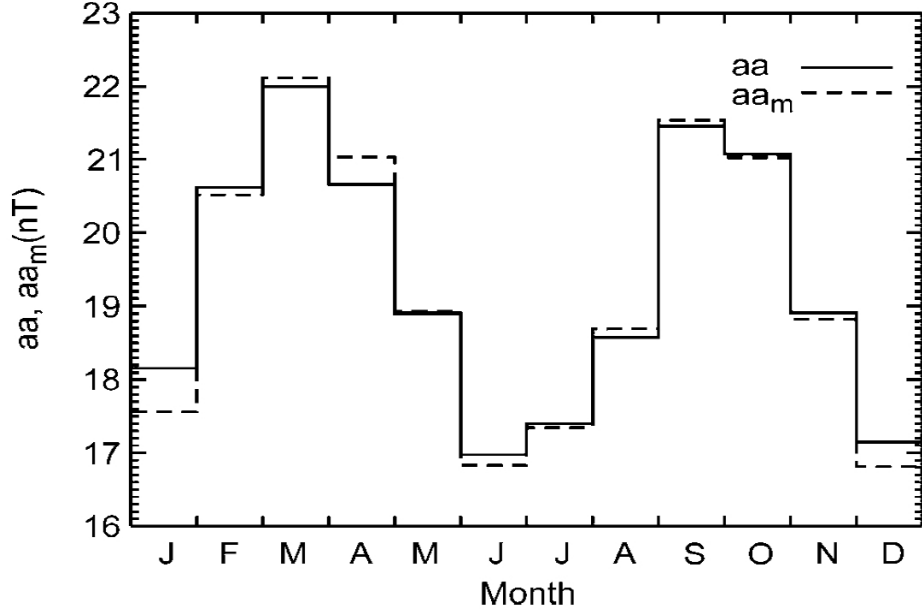


**Figure 2.5:** Seasonal variation of the geomagnetic  $aa$  and  $aa_m$  indices (from *Svalgaard et al.*, 2002).

convection becomes enhanced. Magnetic energy from the solar wind is transferred to the magnetosphere through magnetic merging on the dayside. The open flux that is created on the dayside convects into the tail lobes. The open flux builds up in the magnetotail and the ionospheric footprint of open flux (the polar cap) grows. In Figure 2.6 the polar cap resides within the auroral oval. Panels A and B show the polar cap near the end of the growth phase, when it is close to its maximum size. This increase of open magnetic flux leads to an increase of the strength of the magnetic field in the tail lobes. As the strength of the field in the tail grows, the plasma sheet thins. The cross-tail current becomes stronger during the growth phase (*McPherron*, 1972).

The second phase of a substorm, the expansion phase, corresponds to panels C and D in Figure 2.6 and is characterised by an increase in the intensity of the visible aurora. On average, the expansion phase lasts 5 - 30 minutes (*Akasofu*, 1964). The first brightening of the nightside aurora is referred to as the expansion phase onset and is often used to define the start of a substorm (*Elphinstone et al.*, 1996). Energy that was built up in the magnetotail during the growth phase is released

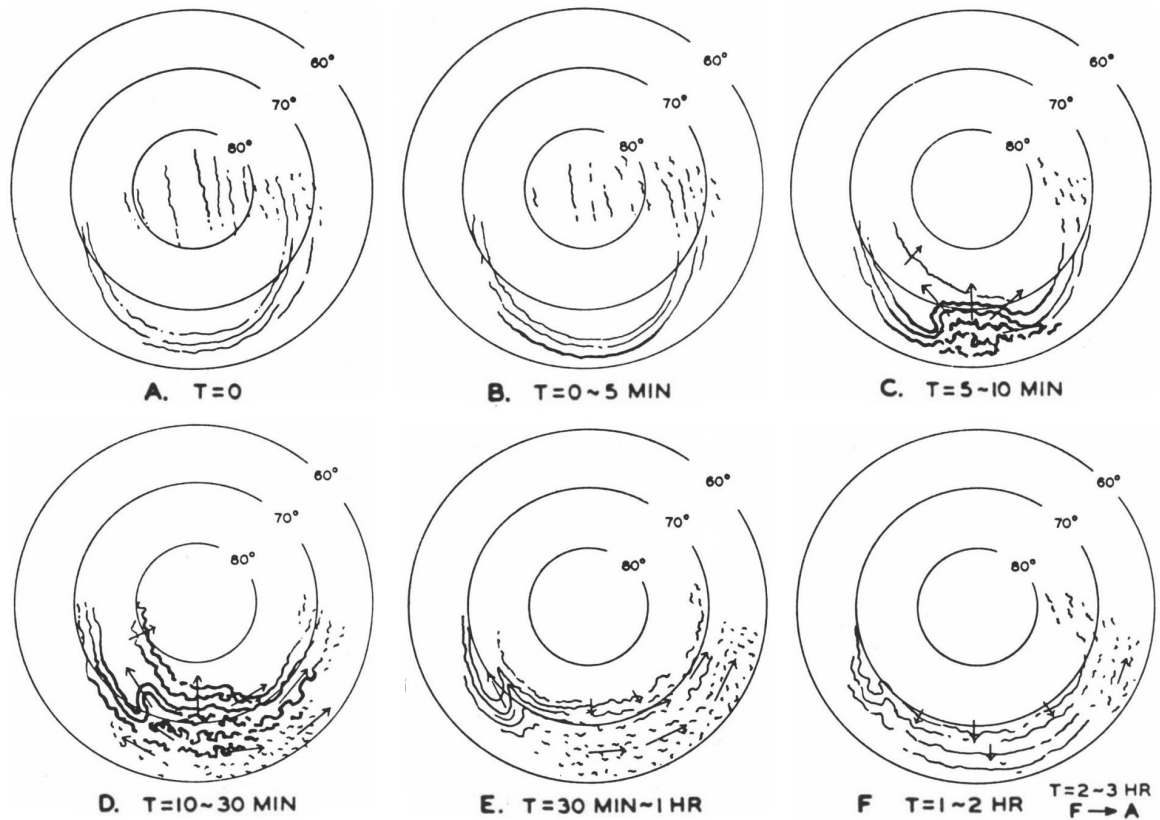


**Figure 2.6:** The different phases of a substorm as seen in the visible aurora. A-B: the quiet phase, C-D: the expansion phase, E-F: the recovery phase. (Adapted from *Akasofu*, 1964). Local midnight is towards the bottom of each panel.

rapidly. Newly closed magnetic field lines retreat back towards the Earth dragging magnetotail plasma with them. An auroral signature of this phase is that the visible aurora expands poleward throughout the duration of the expansion phase, such as in the transition in Figure 2.6 from C to D.

At onset and during the substorm expansion phase the cross-tail current becomes disrupted, and it is diverted into the ionosphere. This phenomena is called the substorm current wedge and it can be observed on Earth as an enhanced westward electrojet current. The strong westward electrojet current can be observed by ground-based magnetometer stations as a strong southward magnetic perturbation, which is often used to quantify substorm activity. This westward electrojet current is closed by a downward field aligned current on the eastern side and an upward field-aligned current on the western side. Pseudo-breakups, a phenomenon

similar to a substorm, may occur during the growth phase of a substorm (*Koskinen et al.*, 1993). They share most the same features that are present during full blown substorms, the difference being that pseudo-breakups are much more localised and have a much smaller poleward expansion of the aurora. During pseudo-breakup a full-fledged substorm current wedge does not develop (*Koskinen et al.*, 1993).

After the expansion phase the recovery phase begins. During this phase there is a reduction in the intensity of the aurora globally (*Akasofu*, 1964), as illustrated in panels E and F of Figure 2.6. The aurora tends retreat equatorward during the recovery phase (*Elphinstone et al.*, 1996).

### 2.2.2 Sawtooth Events

Sawtooth events are sequences of large amplitude oscillations of energetic particle fluxes in the near magnetotail that occur with a variable repetition rate of between 2 to 4 hours. Their phenomenology greatly resembles that of substorms (*Henderson et al.*, 2006). During sawtooth events the magnetosphere is moderately to strongly driven by a continuously southward IMF (IMF  $B_z \leq -10$  nT) (*Henderson et al.*, 2006). Sawtooth events get their name because plots of the proton flux measurements by satellites on the nightside have a shape similar to that of a saw blade (*Belian et al.*, 1995). The proton fluxes that are observed on the nightside are associated with strong stretching and dipolarization of the magnetotail. *Henderson et al.* (2006) proposed that the quasi-periodicity of sawtooth events is the time for the magnetosphere to be driven to a point of instability and therefore to substorm expansion phase onset.

*DeJong et al.* (2007) compared sawtooth events to isolated substorms using auroral measurements made by POLAR and IMAGE satellites. It was found that an individual sawtooth had more intense aurora, that the aurora extended further north in magnetic latitude, and that the amount of open magnetic flux in the polar cap was larger. It was found 150% more magnetic flux, on average, was contained in the polar cap during an individual sawtooth event as compared to an isolated substorm (*DeJong et al.*, 2007). Sawtooth events also release more open flux at expansion

phase onset than isolated substorms, but the percentage released was the same as isolated substorms. Both displayed a 30% decrease in polar cap magnetic flux during the expansion phase.

A statistical comparison between isolated substorms and sawtooth events was conducted by *Cai et al.* (2006). They investigated whether dipolarization during sawtooth events was a global phenomenon. This was done by examining the magnetic tilt angle measured by the geosynchronous GOES satellites. The tilt angle is the angle between the magnetic field vector and the equatorial plane of the planetary magnetic field. *Cai et al.* (2006) found that individual teeth follow a dipolarization pattern similar to isolated substorms, the difference being that the magnetotail is much more stretched prior to onset for a sawtooth than for isolated substorms. The dipolarisation observed is also much larger during individual teeth and is present over a wider magnetic local time sector.

Although sawtooth events represent an unstable configuration of the magnetosphere, it has been suggested that they are similar in nature to steady magnetospheric convection, the difference being that the magnetosphere is too strongly driven during sawtooth events to dissipate energy without the occurrence of substorms (*Henderson et al.*, 2006).

### 2.2.3 Steady Magnetospheric Convection

Steady magnetospheric convection (SMC) is the third type of magnetospheric convection. It is a case of steady, balanced dynamic equilibrium where reconnection rates on the dayside and on the magnetotail are balanced. Qualitatively, SMC events are defined as times when the energy input into the magnetosphere is enhanced and no substorm signatures are observed for extended time periods, i.e., for times longer than a typical substorm interval. This implies the large scale stability of the magnetotail is maintained.

Solar wind conditions during SMC are characterised by moderate solar wind speeds, typically below 450 km/s, as well as moderately southward IMF, with IMF  $B_z$  typically about -3 nT (*O'Brien et al.*, 2002).

Steady convection can occur without enhanced energy input to the magnetosphere, but it is preferential to study SMC events that have a similar level of convection as substorms. SMC events that have enhanced convection are interesting to study because moderate to strong energy input into the magnetosphere is expected to generate semi-periodic substorms or sawtooth events, rather than SMC (*Sergeev et al.*, 1995).

The duration of SMC events originally considered was between 4 and 6 hours. This duration is twice the average time between substorms and longer than a typical substorm (*Sergeev et al.*, 1995). This ensures that substorm growth and recovery phases are not misinterpreted as SMC. *O'Brien et al.* (2002) allowed for shorter durations and stated that there is no obvious minimum duration for an SMC event but that there should be a continuum from very short to very long durations. The requirement that SMC events must have a minimum time length is usually applied to ensure that the SMC events are not confused with part of a substorm cycle.

The most important criterion of SMC is the long term, large scale stability of the magnetotail. The key to defining stability lies in the content of magnetic flux in the lobes. During the expansion phase of substorms the magnetic flux in the magnetotail is reduced by about 20% to 30%. During SMC the variation in the lobe flux content is expected to be less than this (*Sergeev et al.*, 1995). If the flux content of the magnetotail is stable then the open flux in the polar cap should remain constant. A relatively stable polar cap area implies that the reconnection rate on the dayside magnetopause is balanced by the reconnection rate in the magnetotail.

A global simulation of SMC conducted by *Goodrich et al.* (2007) found that during SMC, quasi-steady reconnection occurs in the midtail 35-40  $R_E$  downstream from the Earth. This quasi-steady reconnection in the magnetotail drives steady earthward flows which are diverted to the dusk and dawn sectors due to a thick current sheet. This diversion of flow left the modelled inner magnetosphere undisturbed. *Goodrich et al.* (2007) also performed a simulation of a sawtooth event. They found that both the SMC and sawtooth events demonstrated a similar magnetospheric convection system, the difference being that reconnection in the magnetotail was

intermittent and patchy for the sawtooth event with flow bursts penetrating into the inner magnetosphere. These flow bursts are associated with observed plasma injections and field signatures observed at geosynchronous orbit.

During SMC there is evidence that the plasma sheet magnetic flux content may undergo a slow large scale reconfiguration similar to the substorm recovery phase, but proceeding at a slower pace (*Sergeev et al.*, 1995). If the plasma sheet magnetic flux content is relatively stable no poleward motion of the aurora oval and no substorm current wedge should be observed during SMC.

Pseudo-breakups are a prominent feature of SMC as well. It has been suggested that during SMC pseudo-breakups release energy on a small scale so that the convection can remain steady on a large scale (*DeJong and Clauer*, 2005). *DeJong et al.* (2007) found the difference between the isolated substorms and SMC lies in the amount of open flux. The open flux content in the polar cap decreases by 20% to 30% for isolated substorms, which is contrary to SMC. During SMC the flux content in the polar cap is expected to remain roughly constant.

Although difficult to quantify, SMC is a fundamental concept of the dynamics and stability of the earth's magnetosphere. Understanding SMC would greatly improve our understanding of magnetospheric physics and predictive capabilities of space science.

# CHAPTER 3

## THE IONOSPHERE

### 3.1 Introduction

The ionosphere is the region of the magnetosphere that is closest to the surface of the Earth, and is the most accessible for study. Because the electric field in the magnetosphere maps down to ionospheric heights, observations of convection in the ionosphere effectively mirror convection in the magnetosphere (e.g., *Ruohoniemi and Baker, 1998*).

For purely southward IMF, the classic two-cell ionospheric convection pattern, displayed in Figure 3.1, has anti-sunward flow over the pole and sunward flow at lower latitudes. The black solid and dashed lines in Figure 3.1 represent the convection streamlines in the ionosphere. These streamlines represent the direction plasma in the ionosphere will drift. In the F region SuperDARN makes measurements where relatively few collisions take place so the plasma experiences a bulk drift, which will be described in detail in section 3.4. In the F region the bulk plasma flow velocity is perpendicular to the ionospheric electric field, therefore plasma flow streamlines are equivalently equipotential contours. The dashed lines in Figure 3.1 represent contours that have a positive voltage, while the solid lines represent contours where the voltage is negative. The “ $\times$ ” and “ $+$ ” symbols represent the minimum and maximum voltages, respectively. The potential difference between the maximum and minimum voltage is the cross polar cap potential difference (PCPD) and often used as an indication of the magnitude of convection in the magnetosphere. Caution should be exercised when using the cross polar cap difference because the plasma drift velocity is not directly dependent on the voltage. It is the cross polar cap electric

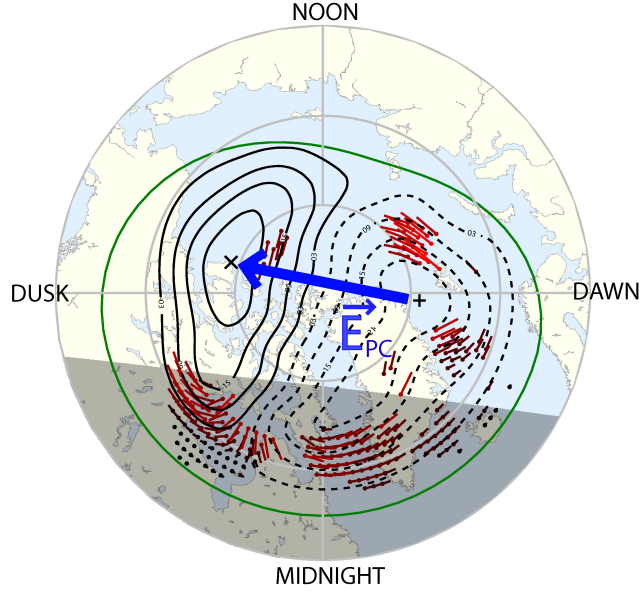


**Figure 3.1:** An example of an ionospheric equipotential contours in the northern hemisphere from SuperDARN. The Sun is towards the top of the the figure and local midnight is towards the bottom. The vector  $\vec{E}_{pc}$  represents the cross polar cap electric field.

field,  $\vec{E}_{pc}$ , that drives plasma flow across the polar cap and PCPD is dependent on the distance between voltage centres, as well as on the cross polar cap electric field.

## 3.2 The Neutral Atmosphere

To first order, the ions and electrons that exist in the ionosphere are the result of photo-ionisation of neutral atmospheric constituents. It is therefore appropriate to study the density of neutral atmospheric constituents as a function of height.

If one assumes that the neutral gas is stationary and horizontally stratified only, a simplistic model of the gravitational force balanced by thermal pressure gradient force can be applied. This is called hydrostatic balance and is expressed:

$$\frac{\partial(nkT)}{\partial z} = -nmg, \quad (3.1)$$

where the acceleration due to gravity is  $g$ , and  $m$  is the mass of a neutral constituent of the gas. The vertical pressure gradient on the left hand side of Equation 3.1 depends on the particle density,  $n$ , the gas temperature,  $T$ , and Boltzmann's constant,

$k$ . Equation 3.1 is based on the “flat Earth” approximation where  $z$  is the vertical distance above the Earth’s surface.

With several assumptions a simple, yet useful, result can be derived from Equation 3.1. By neglecting changes in the temperature of the gas species and changes in the gravitational constant  $g$  as a function of height, integrating from some reference altitude  $z_o$  to the altitude of interest  $z$ , the gas density  $n(z)$  is:

$$n(z) = n_o e^{-(z-z_o)/H} , \quad (3.2)$$

where,

$$H = \frac{kT}{mg} \text{ and} \quad (3.3)$$

the number density at some reference altitude is  $n_o$ . A new variable is defined in Equation 3.3 called the scale height,  $H$ . It is the vertical distance upwards over which the pressure of the atmosphere decreases by a factor of  $e$ . From Equation 3.2 several things can be learned: (1) the majority of the Earth’s atmosphere is located near the Earth’s surface, and (2) the number density of a gas near the Earth’s surface can be used to estimate it at any height.

### 3.3 The Ionosphere

There are two principle mechanisms for ionising atoms and molecules in the upper atmosphere. These are photo-ionisation by solar radiation and bombardment by energetic particles from the magnetosphere. Only the details of photo-ionisation are considered in this thesis since it is relevant for electrojet currents and therefore SMC studies. Particle precipitation is more important for disturbed times such as substorms and sawteeth events.

When solar radiation reaches the Earth, photons are absorbed by neutral atmospheric constituents. As the photons travel earthward, they encounter an exponentially increasing atmospheric density. At high altitudes photo-ionisation is limited by the low neutral gas concentration, while at low altitudes photo-ionisation is limited by the low levels of ionising radiation. In between these two limiting regions,

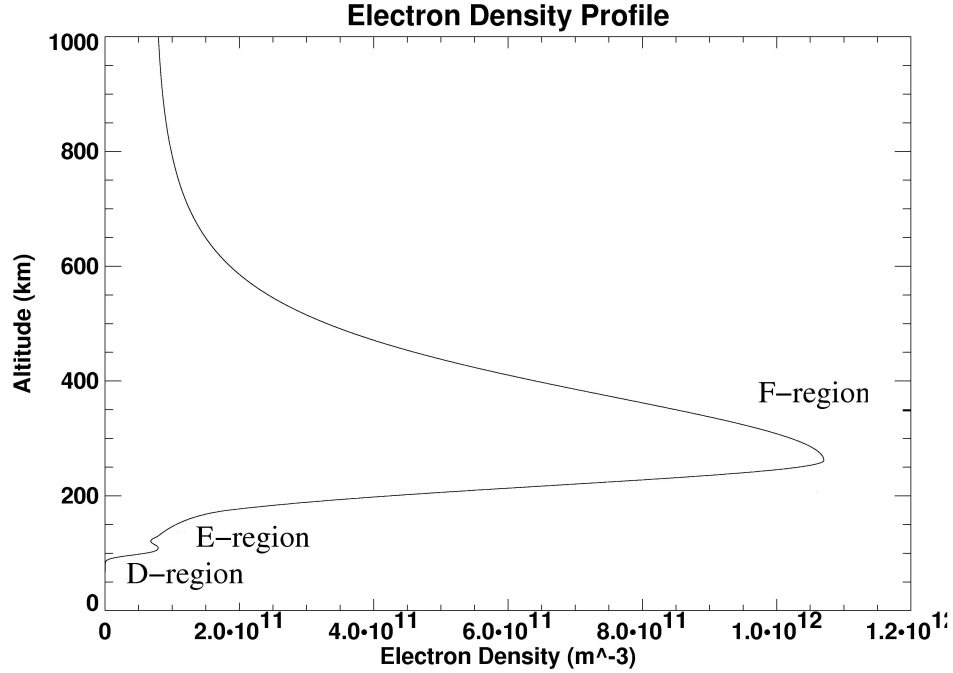


**Figure 3.2:** The modelled electron density in the atmosphere with regions of the ionosphere identified (adapted from *Bilitza, 2001*).

a layer of peak plasma production exists. Figure 3.2 is an example of the electron concentration in the Earth's atmosphere with height (*Bilitza, 2001*). The D, E, and F regions of the ionosphere are indicated in this figure.

To estimate the electron density in the ionosphere one must begin with the ion electron production. The following derivation is adapted from *Luhmann (1995)*. Light travelling an incremental differential distance,  $ds$ , through the neutral gas the intensity of light,  $I$ , is attenuated by an amount  $dI$ . The amount of attenuation depends on the density of the neutral gas,  $n$ , and the absorption cross section,  $\sigma$ , such that:

$$dI = -I\sigma nds . \tag{3.4}$$

Consider sunlight entering the atmosphere at an angle  $\chi$  from the vertical direction, as illustrated in Figure 3.3. The differential height above the surface  $dz$  is related to the path length  $ds$  since  $ds = -dz \sec(\chi)$ . Therefore Equation 3.4 becomes:

$$dI = In\sigma \sec(\chi)dz . \tag{3.5}$$

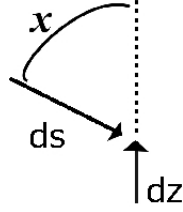


**Figure 3.3:** The differential path length  $ds$  in relation to  $\chi$ , the solar zenith angle, and the differential height  $dz$  in a horizontally stratified atmosphere.

Rearranging Equation 3.5 leads to an expression for the attenuation of the incident light:

$$\frac{dI}{I} = n\sigma \sec(\chi) dz . \quad (3.6)$$

To find the intensity of sunlight that penetrates through the atmosphere to a particular altitude, one must integrate down through the atmosphere from the Sun (effectively at infinity) to the altitude of interest:

$$\int_{I_\infty}^I \frac{dI}{I} = \int_\infty^z n(z)\sigma \sec(\chi) dz . \quad (3.7)$$

Substitution of Equation 3.2, the neutral density from simple hydrostatic balance, leads to:

$$\ln\left(\frac{I}{I_\infty}\right) = -n\sigma H \sec(\chi) , \quad (3.8)$$

where  $H$  is the scale height of the neutral gas (Equation 3.3). The quantity  $n\sigma H \sec(\chi)$  is known as the optical depth,  $\tau$ , so Equation 3.8 can be further simplified as follows:

$$I = I_\infty e^{-\tau} , \quad (3.9)$$

The production rate,  $Q$ , describes how incoming radiation ionises the neutral atmosphere,

$$Q = \xi \sigma n I . \quad (3.10)$$

where  $\xi$  is the ionising efficiency of the incoming radiation. The production rate maximises at the altitude where  $dQ/ds = 0$ , so at the height of maximum photoionisation:

$$-\frac{1}{n_{max}} \frac{dn}{ds} = \frac{1}{I_{max}} \frac{dI}{ds} , \quad (3.11)$$

where  $n_{max}$  and  $I_{max}$  are the density and intensity at the height of maximum production. The derivative of Equation 3.2 with respect to the path length can be calculated, as  $ds = -\sec(\chi)dz$ . This leads to the following expression for the left hand side of Equation 3.11:

$$\frac{1}{n_{max}} \frac{dn}{ds} = \frac{\cos(\chi)}{H} . \quad (3.12)$$

Substituting Equation 3.12 and Equation 3.4 into Equation 3.11 reveals that at the height of maximum production:

$$\sec(\chi)H\sigma n_{max} = 1 . \quad (3.13)$$

Recalling this is the definition of the optical depth,  $\tau$ , the maximum production rate occurs where the optical depth is unity. It should be noted that the optical depth is a function of the absorption cross section,  $\sigma$ , and is different for various wavelengths of light, so the peak production will occur at different altitudes for different wavelengths of light.

It can be advantageous to derive an expression for the production rate in terms of the maximum production rate. Because the optical depth is unity at the maximum production height, Equation 3.9 becomes  $I_{\infty}e^{-1}$ . Combining this with Equation 3.13, Equation 3.10 can be rewritten:

$$Q_{max} = \frac{\xi I_{\infty}}{eH \sec(\chi)} . \quad (3.14)$$

Now consider the neutral gas density at the height of maximum production, using the neutral gas profile,

$$n_{max} = n_o e^{-(z_{max}-z_o)/H} . \quad (3.15)$$

Substituted into Equation 3.13, the following result can be obtained,

$$n_o = \frac{e^{(z_{max}-z_o)/H}}{\sec(\chi)H\sigma} . \quad (3.16)$$

This now allows the reference density,  $n_o$ , to be explicitly included in the equation for the production function, by substituting Equation 3.16 into Equation 3.10. The production function becomes:

$$Q = \frac{\xi I_{\infty}}{H\sec(\chi)} e^{(z_{max}-z_o)/H} e^{-(z-z_o)/H} e^{-\tau} . \quad (3.17)$$

Expanding  $e^{-\tau}$  using the neutral gas profile yields:

$$e^{-\tau} = \exp\left(-e^{(z_{max}-z)/H}\right) . \quad (3.18)$$

Using this result and including the expression for  $Q_{max}$  (Equation 3.14) the production rate can be written as follows:

$$Q = Q_{max} \exp\left(1 + \frac{z_{max} - z}{H} - e^{z_{max}-z/H}\right) . \quad (3.19)$$

This equation describes the well known ‘‘Chapman production function’’ (e.g., *Luhmann, 1995*).

When the Sun is directly overhead the maximum overhead production rate from Equation 3.10 is given by:

$$Q_{mo} = \eta\sigma I_{mo} n_{mo} . \quad (3.20)$$

Recall that for maximum production the optical depth is unity. Therefore Equation 3.14 can be rewritten:

$$Q_{max} = Q_{mo} \cos(\chi) . \quad (3.21)$$

Therefore the production of plasma, relative to the maximum possible production, is modulated throughout the year by the tilt of the Earth’s rotational axis. The preceding discussion includes only the production of plasma, but loss processes must be included to determine the ambient plasma number density. In the ionosphere there are two principle loss processes for electrons: (1) recombination, where an electron and a ion combine, and (2) attachment, where an electron combines with a neutral atom or molecule to produce a negative ion.

In the region of the ionosphere where currents flow, recombination is the dominant loss mechanism (*Brekke and Hall, 1988*). The probability for one electron to combine with an ion is proportional to the ion density since recombination implies collisions. The number of electrons that can recombine must also be proportional to the electron density. Since the plasma in the ionosphere is quasi-neutral,  $n_e \simeq n_i$ , one can write:

$$L = \alpha n_e^2 , \quad (3.22)$$

where  $L$  is the loss rate, and the proportionality constant,  $\alpha$ , is called the recombination coefficient. If one assumes the charged particles are in equilibrium in the ionosphere then the production and loss rates are balance and  $L$  is equal to  $Q$ . This will be true for the maximum production rate as well. Thus the maximum electron concentration, based on Equation 3.22 and Equation 3.21, will be related to the solar zenith angle, as follows:

$$n_{max} \propto \sqrt{\cos(\chi)} . \quad (3.23)$$

### 3.4 Electrical Conductivity in the Ionosphere

Currents in the ionosphere flow because of the relative motion of ions and electrons. For the materials that compose the ionosphere, the current density is proportional to the force per unit charge. The constant of proportionality between the two is called the electrical conductivity of the medium. Ionospheric conductivity is dependent on the properties of the medium.

When charged particles move through the ionosphere they collide with neutral and charged particles. The collision frequency is defined for each pair of interactive species. For example,  $\nu_{in}$  is the collision rate between ions and any species of neutral particle and  $\nu_{ie}$  is the collision rate between ions and electrons. The collision rate between the electrons and the ions,  $\nu_{ie}$ , is much smaller than  $\nu_{in}$  or  $\nu_{en}$  and is often considered negligible (*Walker and Russell, 1995*).

Consider charged particle motion in the presence of only an electric field and collisions. The momentum equation is given as follows:

$$m_\alpha \frac{D\vec{v}_\alpha}{Dt} = q_\alpha \vec{E} - m_\alpha \nu_{\alpha n} (\vec{v}_\alpha - \vec{U}_n) , \quad (3.24)$$

where  $\alpha$  is the particle species (ion or electron). The variable  $\vec{U}_n$  represents the ambient velocity of the neutrals and is zero in the rest frame of the neutrals. The mass of the particle is given by  $m_\alpha$ ,  $\nu_{\alpha n}$  is the collision rate with the neutrals,  $\vec{v}_\alpha$  is the drift velocity of the particle, and  $q_\alpha$  is the charge of the particle. Consider the equilibrium, or steady-state, condition of force balance in the rest frame of the

neutrals where:

$$q_\alpha \vec{E} = m_\alpha \nu_{\alpha n} \vec{v}_\alpha . \quad (3.25)$$

In a situation with only electric fields and collisions, both electrons and ions drift parallel to the electric field so vector notation is no longer required. If  $i$  and  $e$  represent ions and electrons, respectively, and the generic charge of  $q_\alpha$  is replaced by the quantised electron charge,  $e$ , ( $q_i = +e$ ;  $q_e = -e$ ) the particle velocities are given by:

$$v_i = \frac{qE}{\nu_{in}m_i} ; \quad (3.26)$$

$$v_e = \frac{qE}{\nu_{en}m_e} . \quad (3.27)$$

Therefore, the drift velocity for any kind of charged particle in the ionosphere is known when only an electric field is the driver. This is advantageous because the electric current density is defined as the amount of charge passing through a cross sectional area per unit time. In the case of the ionosphere, both ions and electrons have a charge magnitude of  $e$ . Their velocity,  $\vec{v}_\alpha$ , and their density,  $n_\alpha$ , are known. With these three parameters one can obtain the electric current density, since the current density is defined as:

$$\vec{J} = n_e e (\vec{v}_i - \vec{v}_e) . \quad (3.28)$$

Again, vector notation is not required as the electric current density will be parallel to the drift velocity. Substituting Equations 3.26 and 3.27 into Equation 3.28 leads to the following:

$$J = e^2 n_e \left( \frac{1}{\nu_e m_e} + \frac{1}{\nu_i m_i} \right) E . \quad (3.29)$$

With only an electric field present, the current density can also be defined as follows:

$$\vec{J} = \sigma \vec{E} . \quad (3.30)$$

Based on the results of Equation 3.29 and Equation 3.30, the conductivity in the presence of an electric field only can be written:

$$\sigma = e^2 n_o \left( \frac{1}{\nu_e m_e} + \frac{1}{\nu_i m_i} \right) . \quad (3.31)$$

This result is useful, but it is incomplete, as there is also a magnetic field present in the ionosphere. The Earth's magnetic field plays an important role in the motion of charged particles in the ionosphere. Consider the high northern latitude case where the magnetic field is pointing nearly radially inward toward the Earth.

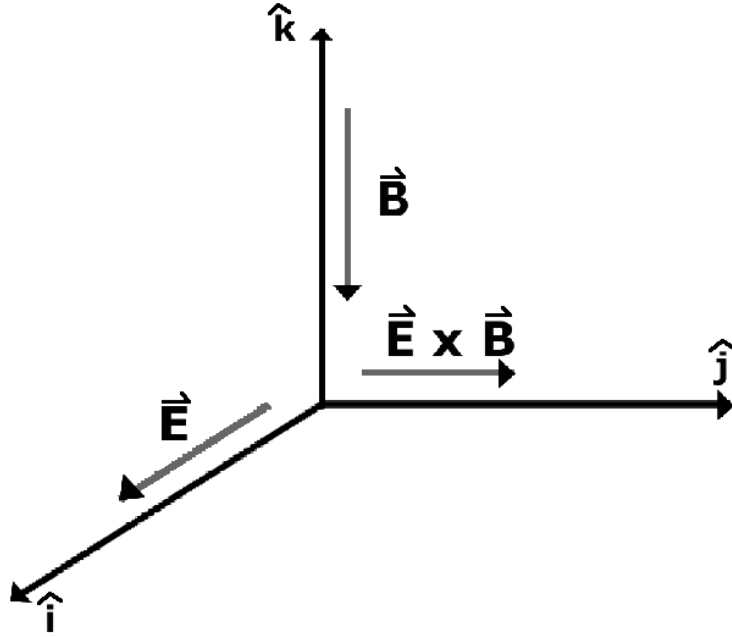


**Figure 3.4:** The coordinate system for the magnetic and electric fields in the ionosphere for the high latitude case.

This changes the situation but does not nullify the result of Equation 3.31. The above result is still useful because when a charged particle moves parallel to the magnetic field it experiences no Lorentz force. That is why the conductivity in Equation 3.31 is often referred to as  $\sigma_{\parallel}$ , the conductivity in a direction parallel to the magnetic field. Figure 3.4 shows the electric and magnetic field direction in the high latitude ionospheric coordinate system. The electric field has two components, one perpendicular to the magnetic field ( $\vec{E}_{\perp}$ ) and one parallel to the magnetic field ( $\vec{E}_{\parallel}$ ). The full electric field vector can be written as follows:

$$\vec{E} = \vec{E}_{\parallel} + \vec{E}_{\perp} = E_z \hat{k} + E_x \hat{i} . \quad (3.32)$$

The charged particles moving perpendicular to the magnetic field feel two contributions to their acceleration, namely that of the electric field,  $\vec{E}$ , and of the magnetic

field,  $\vec{B}$ . Similar to the case where there was no magnetic field, it is assumed that collisional effects are balanced by the electromagnetic forces:

$$q_\alpha(\vec{E} + \vec{v}_\alpha \times \vec{B}) = m_\alpha \nu_{\alpha n} \vec{v}_\alpha . \quad (3.33)$$

Consider the drift velocity in the direction perpendicular to the magnetic field. This drift velocity is effectively horizontal in the northern polar regions. The vector components can be separated according to the geometry of Figure 3.4:  $\vec{v}_\alpha = v_{\alpha x} \hat{i} + v_{\alpha y} \hat{j}$ ,  $\vec{E} = E_x \hat{i}$ , and  $\vec{B} = -B_z \hat{k}$ . Because of the addition of the magnetic field the velocities perpendicular to the magnetic field will have components in both the  $\hat{i}$  and the  $\hat{j}$  directions. Substituting these components into the equilibrium equation (Equation 3.33) results in the following equations:

$$\frac{q_\alpha E_x}{m_\alpha} - \frac{q_\alpha v_{\alpha y} B_z}{m_\alpha} = \nu_{\alpha n} v_{\alpha x} , \quad (3.34)$$

$$\frac{q_\alpha v_{\alpha x} B_z}{m_\alpha} = \nu_{\alpha n} v_{\alpha y} . \quad (3.35)$$

It is useful to the derivation to introduce the motion due to gyration at this point, since the gyrofrequency has the same units as the collision frequency. The gyrofrequency is the rate at which a charged particle oscillates around a given magnetic field line. It depends on the mass and charge of the particle as well as the strength of the magnetic field. It is given the symbol  $\Omega$  and is defined as:

$$\Omega_\alpha = \frac{q_\alpha B}{m_\alpha} . \quad (3.36)$$

Equations 3.34 and 3.35 can be rewritten:

$$0 = \frac{q_\alpha E_x}{m_\alpha} - \Omega_\alpha v_{\alpha y} - \nu_{\alpha n} v_{\alpha x} , \quad (3.37)$$

$$0 = \Omega_\alpha v_{\alpha x} - \nu_{\alpha n} v_{\alpha y} . \quad (3.38)$$

The drift velocities of charged particles in the  $\hat{i}$  and  $\hat{j}$  directions are therefore given by:

$$v_{\alpha x} = \frac{q_\alpha \nu_{\alpha n}}{m_\alpha (\Omega_\alpha^2 + \nu_{\alpha n}^2)} E_x , \quad (3.39)$$

$$v_{\alpha y} = \frac{q_{\alpha} \Omega_{\alpha}}{m_{\alpha}(\Omega_{\alpha}^2 + \nu_{\alpha n}^2)} E_x . \quad (3.40)$$

More specifically the motion of the ions and electrons can be considered separately if the species place holder  $\alpha$  in Equations 3.39 and 3.40 is replaced with an  $i$  and  $e$  for the ions and electrons, and the generic charge  $q$  is replaced by  $+e$  for ions and  $-e$  for electrons. The equations of velocity therefore become:

$$v_{ex} = \frac{-e\nu_{en}}{m_e(\Omega_e^2 + \nu_{en}^2)} E_x , \quad v_{ey} = \frac{e\Omega_e}{m_e(\Omega_e^2 + \nu_{en}^2)} E_x \quad (3.41)$$

$$v_{ix} = \frac{e\nu_{in}}{m_i(\Omega_i^2 + \nu_{in}^2)} E_x , \quad v_{iy} = \frac{e\Omega_i}{m_i(\Omega_i^2 + \nu_{in}^2)} E_x \quad (3.42)$$

It is the relative flow of the ions and electrons that gives rise to currents and the components of the current density (Equation 3.30) are:

$$J_x = e^2 n_e \left( \frac{\nu_{in}}{m_i(\Omega_i^2 + \nu_{in}^2)} + \frac{\nu_{en}}{m_e(\Omega_e^2 + \nu_{en}^2)} \right) E_x , \quad (3.43)$$

$$J_y = e^2 n_e \left( \frac{\Omega_e}{m_e(\Omega_e^2 + \nu_{en}^2)} - \frac{\Omega_i}{m_i(\Omega_i^2 + \nu_{in}^2)} \right) E_x . \quad (3.44)$$

There are two conductivities: one parallel to the electric field and one perpendicular to it. The conductivity parallel to the electric field is called the Pedersen conductivity,  $\sigma_P$ :

$$\sigma_P = e^2 n_e \left( \frac{\nu_{in}}{m_i(\Omega_i^2 + \nu_{in}^2)} + \frac{\nu_{en}}{m_e(\Omega_e^2 + \nu_{en}^2)} \right) . \quad (3.45)$$

The conductivity perpendicular to the electric field in the plane of the horizontal atmosphere is called the Hall conductivity,  $\sigma_H$ :

$$\sigma_H = e^2 n_e \left( \frac{\Omega_e}{m_e(\Omega_e^2 + \nu_{en}^2)} - \frac{\Omega_i}{m_i(\Omega_i^2 + \nu_{in}^2)} \right) . \quad (3.46)$$

The presence of  $\vec{B}$  and  $\vec{E}$  fields in ionospheric plasma creates a medium with conductivities in three dimensions. In the polar regions, where the magnetic field is nearly vertical, the full current density vector can be written in terms of a conductivity tensor:

$$\vec{J} = \begin{pmatrix} \sigma_P & \sigma_H & 0 \\ -\sigma_H & \sigma_P & 0 \\ 0 & 0 & \sigma_{\parallel} \end{pmatrix} \vec{E} . \quad (3.47)$$

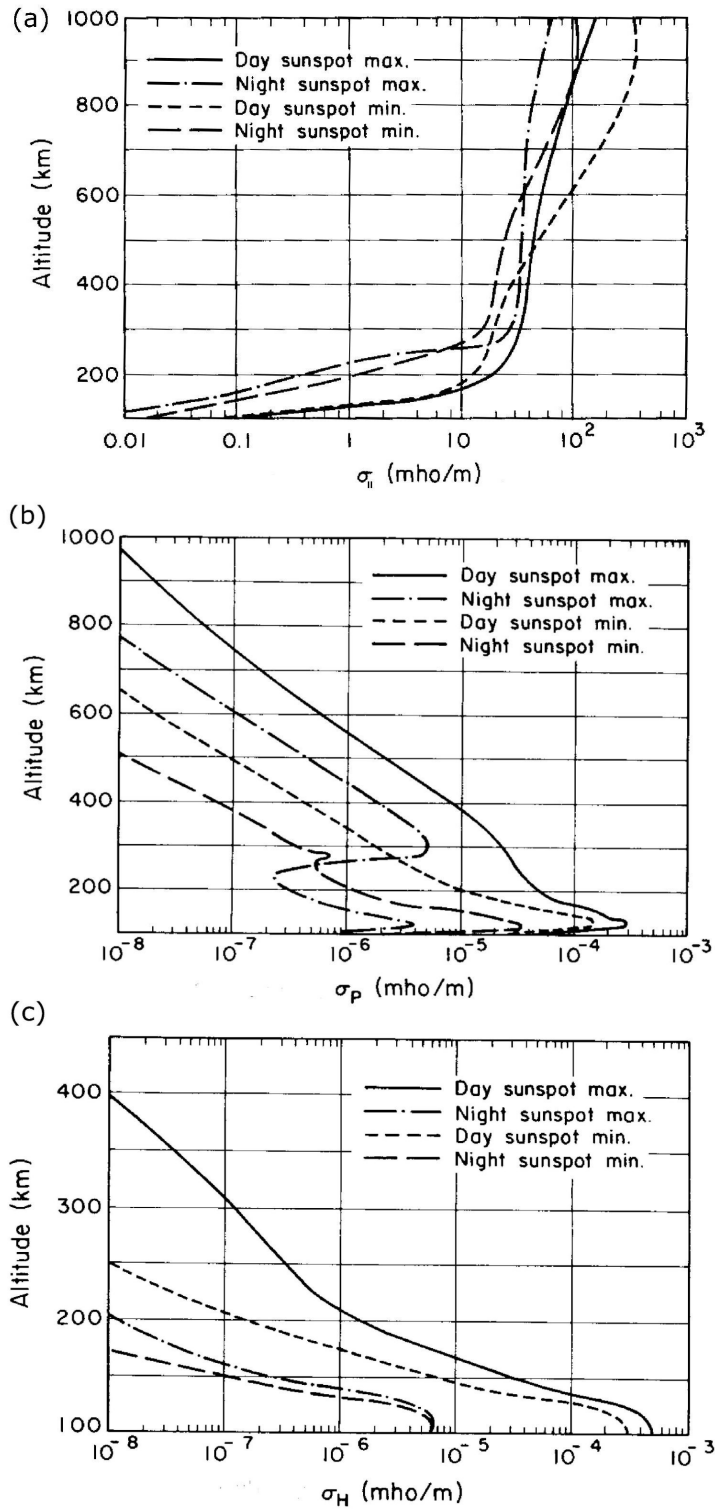


**Figure 3.5:** (a) Parallel conductivity versus altitude, (b) Pedersen conductivity versus altitude, and (c) Hall conductivity versus altitude for the day and night during solar maximum and minimum as indicated (*Johnson, 1961*).

The  $\sigma_{\parallel}$  is related to field-aligned currents (FAC) and is defined by Equation 3.31. The Hall and Pedersen conductivities are related to currents flowing perpendicular to the magnetic field. Figure 3.5 displays typical values for the parallel, Pedersen, and Hall conductivities for day and night at solar minimum and solar maximum.

### 3.5 Regions of the Ionosphere

Each neutral constituent in the atmosphere has a different natural response to light and a different scale height. Because of this, the maximum production rates for different ion species occur at different heights.

In the Earth's ionosphere above 100 km altitude, plasma is mainly produced by photo-ionisation of atomic oxygen  $O$ , molecular nitrogen  $N_2$  and molecular oxygen  $O_2$ , according to the three following reactions:



After the initial photochemical reaction, the  $N_2^+$  ions go through the intermediate reaction to form  $NO^+$ :  $O^+ + N_2 \rightarrow NO^+ + N$ . Likewise,  $O^+$  can interact with  $N_2$  to produce  $NO^+$ :  $N_2^+ + O \rightarrow NO^+ + N$ . At the highest altitudes in the ionosphere  $O^+$  is the dominant ion, as there is little  $N_2$  to produce  $NO^+$ . Lower down increased nitrogen density leads to  $NO^+$  being dominant (*Hunsucker and Hargreaves, 2003*).

Based on electron number density three regions of the ionosphere can be defined: (1) the F region, (2) the E region, and (3) the D region. The ionospheric region at the highest altitude is the F region, and it extends upward from about 150 km. The maximum electron number density in the F region occurs at an altitude of about 250 km and is called the F peak. The F peak is the result of oxygen ion ( $O^+$ ) production and typically has electron concentrations of the order of  $10^6 \text{ cm}^{-3}$  (*Luhmann, 1995*).

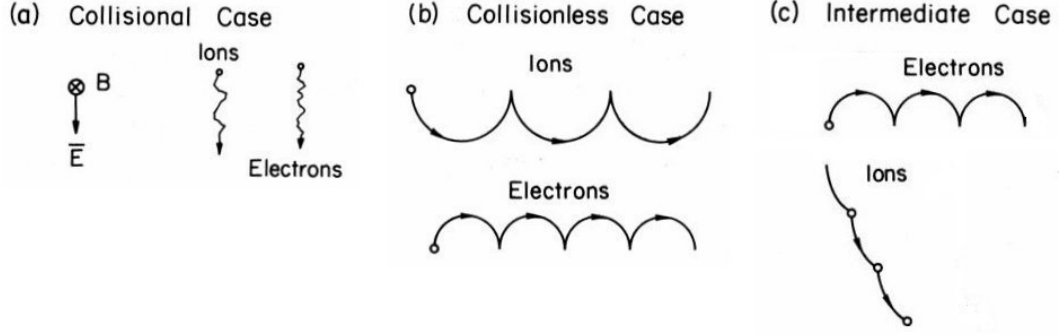


**Figure 3.6:** Three cases of charged particle motion in the ionosphere in the presence of electromagnetic fields and collisions. (Adapted from *Kelley, 1989*).

In the F region the neutral density is low enough that charged particles in this region incur very few collisions. The ion-neutral collision frequency is of the order of  $10 \text{ s}^{-1}$ , and the electron-neutral collision frequency is of the order of  $100 \text{ s}^{-1}$  (*Kelley, 1989*). These collision frequencies are small compared to their respective gyrofrequencies ( $\Omega_i \simeq 150 \text{ s}^{-1}$  and  $\Omega_e \simeq 10^7 \text{ s}^{-1}$ ). Neglecting collisions reveals that in the F region the electron and ion drift velocity is controlled by the electric and magnetic field, as follows:

$$\text{Electrons: } v_{ex} = 0, v_{ey} = \frac{E_x}{B} \quad (3.51)$$

$$\text{Ions: } v_{ix} = 0, v_{iy} = \frac{E_x}{B} \quad (3.52)$$

Figure 3.4 displays typical particle motion in the presence of collisions. The electric and magnetic field direction in the high latitude ionospheric coordinate system displayed in this figure applies to all panels. Both the electrons and the ions are magnetically controlled in the F region, and therefore no horizontal currents will flow in this region, as electrons and ions drift with the same velocity. The drift direction is perpendicular to both the electric and magnetic field as observed in Figure 3.4. Panel (b) of Figure 3.6 displays the typical electron and ion drift motion in the near collisionless F region.

The E region exists between 90 km and 150 km. The E region has a peak in electron number density near 110 km. During times of active aurora the E-region

peak is due to both the production of nitric oxide ions ( $NO^+$ ) and molecular oxygen ions ( $O_2^+$ ) with a typical electron concentrations of  $10^5 \text{ cm}^{-3}$ . In the E region, the neutral density has increased to a value where ions no longer convect in the  $\vec{E} \times \vec{B}$  direction. In this region the ion-neutral collision frequency has increased to about  $10^3 \text{ s}^{-1}$ , which is an order of magnitude greater than the ion gyro frequency (*Kelley, 1989*), and therefore the ions are collision-controlled. The electron-neutral collision frequency is of the order of  $10^4 \text{ s}^{-1}$  for electrons in the E region. Electrons have a much larger gyrofrequency and remain magnetically controlled. Therefore, electrons continue to have a drift motion similar to that displayed in panel (b) of Figure 3.6. The ions, due to the increase in collisions, drift as pictured in panel (c) of Figure 3.6. After a collision with a slower neutral particle the electric field accelerates the ion in the direction of the electric field. As the ion gains speed, the Lorentz force begins to act on it. However, before the ion can make a full rotation, another collision occurs and the cycle repeats. The result is a drift velocity component in the direction of the electric field, which in turn results in relative motion of ions and electrons. This relative motion between charged particles is what produces E-region currents. These E-region currents create magnetic perturbations that can be observed near the surface of the Earth by magnetometers. The E region peak disappears at night, but the F peak does not. This is because  $O^+$  cannot recombine directly; first it must become  $NO^+$ . In the F region, it is difficult for  $O^+$  to become  $NO^+$  because the density of  $N_2$  is lower.

Below the E region lies the D region which has electron concentration up to  $10^4 \text{ cm}^{-3}$ . It is the deepest layer of the ionosphere and exists between 50 km and 90 km altitude (*Luhmann, 1995; Russell, 1995*). In this region the neutral density has increased to the point where ions and electrons are both strongly collisionally controlled. The D-region motion of charged particles is displayed in panel (a) of Figure 3.6. Thus no currents flow in the D-region.

# CHAPTER 4

## IONOSPHERIC AND MAGNETOSPHERIC CONVECTION

### 4.1 Observational Techniques

The Earth's magnetosphere is vast, encompassing a volume of the order of  $10^{26}$  m<sup>3</sup> (*Elphinstone et al.*, 1996), so direct observation is very difficult. There are many satellites in a variety of orbits around the Earth that do make direct observations, but these only make point measurements. Because the ionospheric electric field maps to the magnetosphere, it is possible to quantify many magnetospheric phenomena with Earth-based instruments. Instruments, such as ground-based networks of magnetometers and radars, have been developed to exploit ionosphere - magnetosphere coupling. This coupling makes it possible to study magnetospheric convection from the ground with good spatial and temporal resolution, as well as extensive coverage, while using instruments that are a small fraction of the cost of a satellite.

#### 4.1.1 Auroral Electrojet Indices

The name Auroral Electrojet Indices, or AE Indices, is applied to a group of four variables: (1) the Auroral Upper (AU) Index, (2) the Auroral Lower (AL) Index, (3) the Auroral Electrojet (AE) Index, and (4) the AO index. These were developed as a means to characterise the strength of the global electrojet currents (*Davis and Sugiura*, 1966). A simplified morphology of the electrojet currents is illustrated in Figure 4.1, where noon is towards the top of the page. The currents flow primarily in the anti-sunward direction at low latitudes, in the magnetic latitude

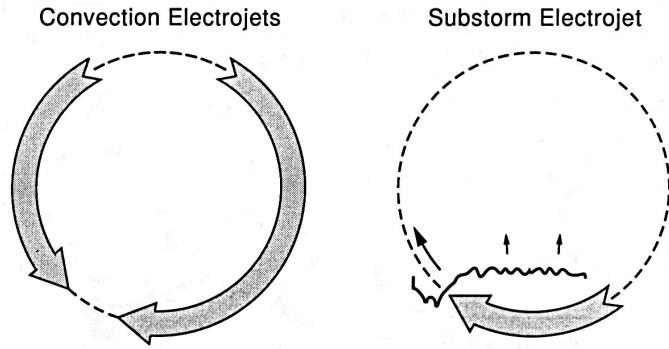


**Figure 4.1:** The auroral electrojet currents (from *Baumjohann and Treumann, 1996*). Noon is toward the top of the figure, midnight is towards the bottom, dusk is towards the left and dawn is towards the right.

range of  $65^\circ - 75^\circ$  (*Davis and Sugiura, 1966*). The convection electrojets develop in response to the large-scale circulation of magnetospheric plasma, while the substorm electrojet becomes important when the magnetosphere is disturbed, such as during a substorm.

To characterise the electrojets, an array of ground-based magnetometers at latitudes near  $70^\circ$  are used (*Kamide and Kokubun, 1996*). Magnetometer networks offer several advantages: (1) they are very responsive to currents that flow in the ionosphere due to the convection cycle and (2) they operate continuously, independent of interruptions such as cloudy skies.

The AE indices are derived from the horizontal variations of the Earth's magnetic field observed at the Earth's surface by 10 to 15 magnetometers in the auroral zone. The north-south magnetic variations are the result of the mainly east-west electrojet currents that flow overhead. Figure 4.2 presents the locations of AE magnetometer stations, which are all in the northern hemisphere. Ideally there would be a similar network in the southern hemisphere, but there is insufficient land in the southern auroral zone to deploy an evenly spaced array of magnetometers. The AE indices are therefore only a northern hemispheric measurement.

The AU index responds to the eastward electrojet current that flows in the dusk side of the ionosphere. The AL index responds to the westward electrojet current or the substorm electrojet in the dawn-midnight sector, as illustrated in Figure 4.1.

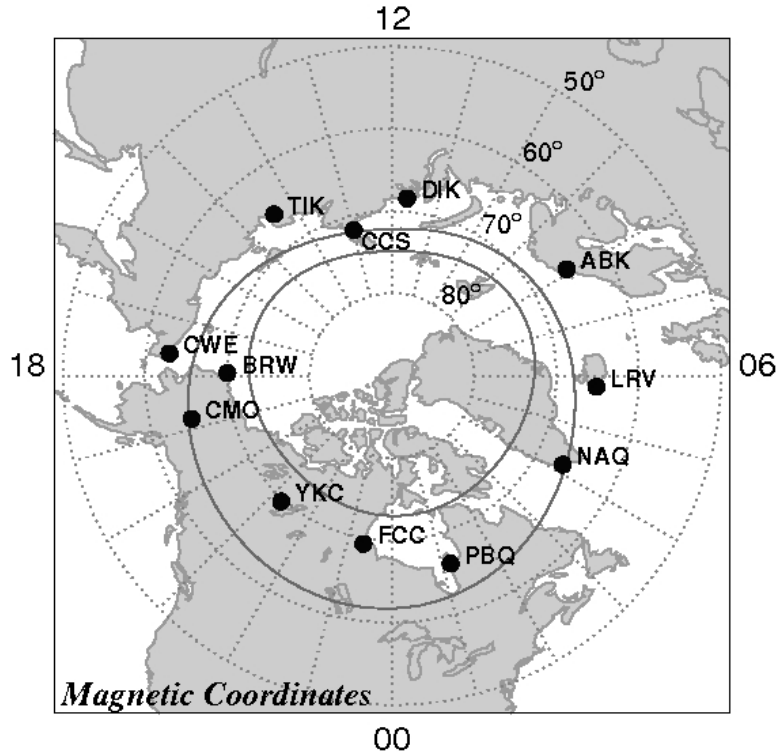


**Figure 4.2:** The location of the magnetometers used to derive the AE indices. The two grey lines enclose the statistical auroral oval for  $K_p=4$  (moderately disturbed) (Feldstein and Starkov, 1967).

The auroral electrojets flow in the regions of sunward return flow in the low latitude part of the global convection pattern (seen in Figure 3.1).

Before calculating the AE indices, the data must be adjusted to a baseline value. The north-south magnetic field value ( $H$  component) is usually recorded with 1-min resolution. The  $H$  component data are then normalised to a base  $H$  value for each station. The base value is calculated each month for each station. It is an average of all of the data for the 5 geomagnetically quietest days of that month. This base value is then subtracted from all  $H$ -component data measured at that particular station during the month.

For each minute, the greatest positive value of the  $H$ -component magnetic field perturbation from all available stations is chosen, and this is the AU index. The greatest positive perturbation is determined by the magnetometer station that is closest to the maximum eastward current intensity. The most negative  $H$  perturbation for all stations at the same instant becomes the AL index, and it quantifies

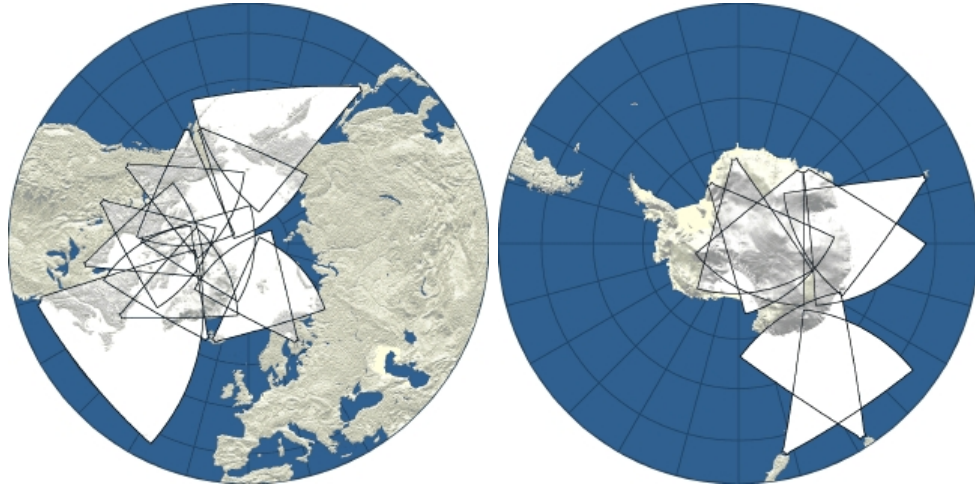


**Figure 4.3:** The shaded areas indicate the viewing area that the SuperDARN radar network covers in the North and South hemisphere, respectively. (Figure courtesy R. Barnes).

the strongest westward electrojet. The AL index responds to either the westward convection electrojet in the dawn sector or to the substorm electrojet in the midnight section, whichever is stronger. The AE index is obtained by subtracting AL from AU and quantifies the total maximum amplitude of the east and west electrojets. Since AU is mainly positive and AL is mainly negative the AE index is mainly a positive value. The AO index is obtained by averaging AU and AL and is a measure of the displacement of the midpoint of AU and AL from the reference level at any time (*Davis and Sugiura, 1966*).

### 4.1.2 SuperDARN

The Super Dual Auroral Radar Network (SuperDARN) (*Greenwald et al., 1995*) is an international network of high frequency (HF) radars. The coverage of the SuperDARN radar network for both hemispheres is displayed in Figure 4.3. SuperDARN measures the convection velocity of plasma in the ionosphere. In the northern hemisphere there are currently twelve radars in operation, while in the southern hemisphere there are seven. Each SuperDARN radar is capable of observing over 4 million square kilometers in the ionosphere.

Each radar in the “common mode” of operation makes a complete scan in

1 or 2 minutes. A single radar beam is swept sequentially through 16 positions separated by  $3.24^\circ$  in azimuth, therefore in one scan a beam sweeps through  $52^\circ$ . Along each beam there are 75 “range gates” of 45 km in length with the first range gate starting at a horizontal distance of 180 km from the radar. Offset along the array boresight, either in front of or behind the main antenna array there is a four-antenna interferometer array that is used to identify the elevation angle of arrival of the returning electromagnetic waves.

SuperDARN measures the convection velocity of the ionospheric plasma using the Doppler shift of returning radar echoes. Each radar can only measure the plasma drift speed in the direction parallel to the radar beam. The ionospheric convection pattern is two dimensional, which is why the radars in the network are designed to operate in pairs. With the two fields of view overlapping, as seen in Figure 4.3, two dimensional velocity vectors can be resolved. To reconstruct the two dimensional flow vectors data from all available radars must be combined. This is done with the “merge” technique, which combines pairs of overlapping components to reconstruct the full velocity vector.

Not all of the SuperDARN range gates contain ionospheric velocity data in every scan. Ionospheric data can be contaminated by echoes from the ground, and poor scattering conditions can lead to no data. In addition to this SuperDARN cannot make velocity measurements over the entire northern region since there are gaps in radar coverage. To obtain a global convection pattern, the velocities in the regions where there are no measured data must be interpolated. Before doing any interpolation measured velocity components are placed in an equal area grid of magnetic latitude and magnetic longitude. The area of each cell in the grid is defined by the spatial scale of  $1^\circ$  in latitude, which is roughly 111 km projected on to the surface of the Earth. For each interval of  $1^\circ$  of latitude the number of grid cells distributed in longitude is set by the requirement that the step in longitude be as close to 111 km as possible. Panel (a) of Figure 4.4 illustrates an example of the gridded line of sight velocity measurements made by SuperDARN. A convection mapping technique developed by *Ruohoniemi and Baker (1998)* is used to produce

two dimensional convection maps from the combined gridded data. At the heart of this technique is an iterative process to find a convection map produced from spherical harmonic functions that best fit the velocity components. The iterative algorithms change the spherical harmonic coefficients until the velocity components from the convection map are as similar as possible to the measured SuperDARN velocity components. It is possible that the electrostatic potential obtained from the convection mapping procedure is unphysical. This is undesirable and this is why, in order to obtain a global convection map that is the most consistent with all available data, the iterative process is initiated with an *a priori* statistical convection model. The statistical model tells one, based on the IMF conditions, what convection pattern is most likely to occur. The statistical model constrains the regions of the convection pattern where no SuperDARN velocity data have been obtained. When there are no velocity components the convection pattern obtained from the iterative convection mapping process is strongly influenced by the model, which may or may not represent what actually occurred.

To ensure that the convection map is a true representation of the actual ionospheric convection pattern, it is important that there be sufficient measurements to dominate the fit (*Ruohoniemi and Baker, 1998*). This is particularly important for SuperDARN studies of SMC because a convection model largely influenced by a statistical constraint is inherently steady.

A typical convection pattern is presented in Figure 4.4 (b). The equipotential lines are represented by the solid and dashed black lines, with dashed lines representing positive voltages and solid lines representing negative voltages. The best-fit algorithm imposes a low magnetic latitude (usually  $\leq 50^\circ$ ) zero-flow and zero-voltage boundary, which is illustrated by the green line in panel (b) of Figure 4.4. The reconstructed flow vectors are overlaid on the best-fit electrostatic potential contours. The IMF conditions for the *a priori* statistical convection pattern are displayed in the top right hand corner of the convection map. The dial plot indicates the direction and magnitude of the IMF vector in the Bz-By GSM plane, and the magnitude of the IMF is printed to the left of the dial plot. The difference between the maximum

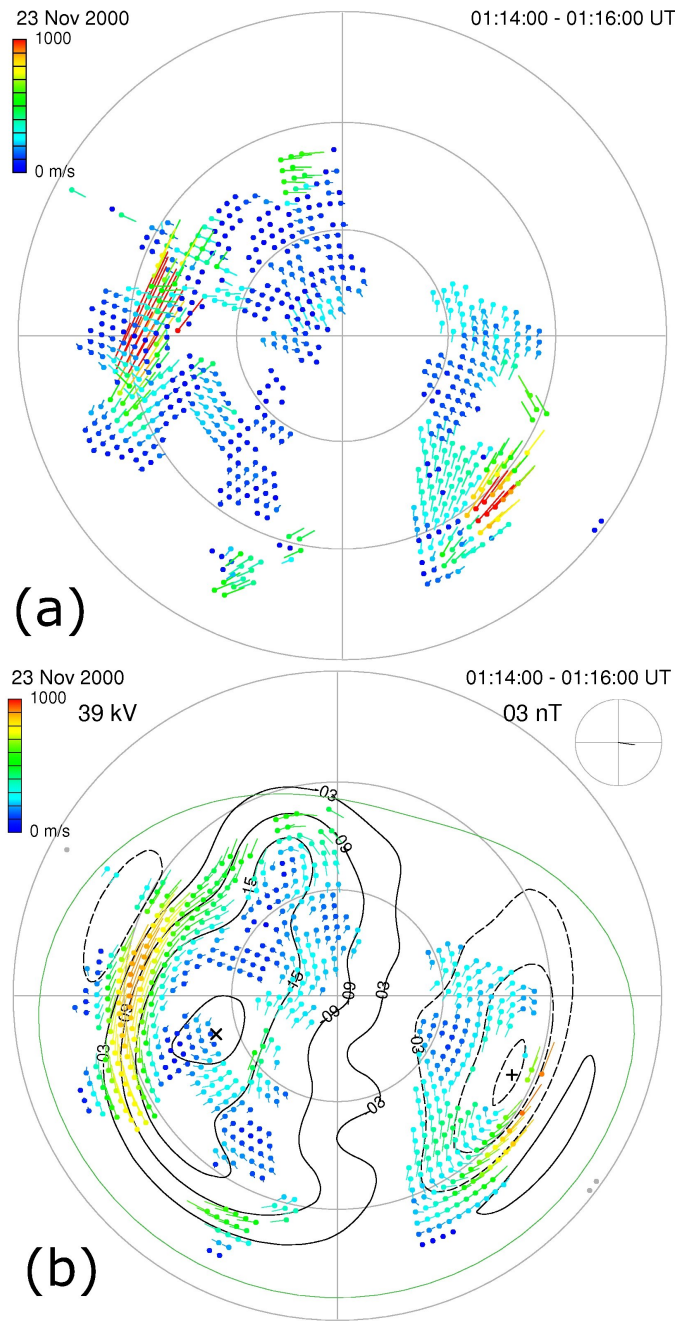


**Figure 4.4:** (a) The gridded line of sight velocity measurements made by SuperDARN. (b) The SuperDARN convection map constructed from the line of sight data. In panel (b) the equipotential contours resulting from the spherical harmonic potential expansion are represented by the black lines. The clock plot in the top right hand corner of panel (b) displays the IMF  $B_z$  and IMF  $B_y$  components used for the statistical model. The maximum and minimum potential are represented by an + and  $\times$  respectively. The potential difference between the maximum and minimum voltage is displayed in the top left corner (figure courtesy R. Barnes).

voltage (+) and the minimum voltage ( $\times$ ) is the cross polar cap potential difference (PCPD).

## 4.2 Previous SMC Results

SMC detection methods have been based on quantitative definitions of phenomena related to SMC, such as magnetometer responses to ionospheric currents. While the qualitative description of SMC is generally accepted, developing a robust quantitative definition has proven to be very difficult. There have been three primary qualitative definitions that have been developed to classify SMC.

*Sergeev et al.* (1995) developed a SMC definition consisting of four criteria that must be satisfied for 4-6 hours: (1) the IMF must be stable and continuously southward; (2) the AE index must be greater than 200 nT to ensure enhanced convection; (3) no substorm signatures should be observed by ground based instruments; and (4) there should be no current sheet disruptions or plasmoid releases in the near Earth magnetotail to ensure that no large scale reconfiguration of the tail occurred. The fourth condition requires in situ magnetotail measurements. If no magnetotail measurements are available, a lack of substorm signatures in ground based data is accepted as confirmation that the tail was not reconfigured.

During SMC, the large scale stability of the magnetotail is maintained, but *Sergeev et al.* (1995) found that auroral zone magnetometers recorded considerable amounts of short term activity. They called these signatures magnetic transient activations. These activations resemble those found during substorms, and without multi-instrument information it would be difficult to differentiate a substorm feature from a transient activation. The duration of these events is typically less than 10 minutes with a periodicity between 10 and 40 minutes. On average the periodicity was 30 minutes. The magnetic field fluctuations during these events can be equal to substorm onset or expansion phase activity levels. The differentiating factor, *Sergeev et al.* (1995) states, is the large scale stability of the magnetotail.

*Sergeev et al.* (1995) found the active auroral regions during SMC resemble

the auroral distribution during the expansion phase of substorms. These aurora are characterised by active, discrete aurora, which form a bulge-like pattern. This bulge is the primary location of the magnetic transient activations, and can persist for several hours during SMC events.

Observations made by satellites during SMC in the magnetotail have found that there are small scale activations in the plasma sheet magnetic field and earthward plasma flow bursts. *Sergeev et al.* (1995) states that these transient activations in the plasma sheet do not change the large-scale state of the magnetotail but can enhance the earthward transport of plasma and magnetic flux.

*Sergeev et al.* (1995) also found that all the SMC events studied began and ended with substorms. They concluded that SMC represents a period of extended activity between two substorms and that it may be that the magnetic configuration required to sustain steady convection can only develop following substorm development. *Sergeev et al.* (1995) found that the substorms that occurred at the end of SMC event could either be triggered due to IMF variations or could occur spontaneously.

The work conducted by *Sergeev et al.* (1995) was an important step in understanding SMC but some have questioned the quantitative definition used. *O'Brien et al.* (2002) stated that the first condition of the *Sergeev et al.* (1995) definition presumed the IMF conditions that should lead to SMC. They also claimed that the third and fourth criteria do not actually quantify steady convection. *O'Brien et al.* (2002) developed a quantitative substorm indicator based on the AL index and also considered shorter lengths of time for the SMC conditions to be maintained. An event was deemed to be SMC if AE was greater than or equal to 200 nT and AL decreased at less than 25 nT per minute for a period of at least 90 minutes. The period of 90 minutes was used instead of 4 hours, because it allowed for the investigation of the behaviour of shorter steady intervals as well. The disadvantage of using this shorter time constraint was that the recovery phase of substorms may be identified as SMC.

The first criterion that  $AE \geq 200$  nT is accepted as an indication that convection is enhanced. The second criterion,  $dAL/dt \geq -25$  nT/min requires a brief

explanation. According to *McPherron et al. (2005)* a moderate substorm expansion phase can last 20 minutes, and the AL index can drop to -500 nT. Therefore AL would have dropped by 25 nT per minute, on average, during the course of the expansion phase. During a larger substorm, AL is expected to drop more quickly than 25 nT per minute. If AL decreases because the convection electrojets have become enhanced due to SMC, it is expected to decrease more slowly than 25 nT per minute. The AL criterion is contentious as it is an empirical rule of thumb.

Applying their criteria to the AE data from 1978 to 1988, *O'Brien et al. (2002)* found 2000 SMC's of duration greater than 90 minutes. Several of these SMC candidate events occurred when IMF Bz varied substantially, thereby contradicting the notion that steady convection must be driven exclusively by a steady negative IMF Bz component. *O'Brien et al. (2002)* found statistically that values of IMF Bz near -3 nT and solar wind velocities below 450 km/s promote but do not always lead to SMC.

*DeJong and Clauer (2005)* developed another technique to classify SMC. The method was based on the principle that when convection in the magnetosphere is steady, the creation and destruction of open flux should be balanced. The amount of open flux in the magnetosphere should therefore remain relatively constant during SMC. When the amount of open flux is constant, the area of the polar cap should not change. *DeJong and Clauer (2005)* used the poleward boundary of the auroral oval as an approximate indicator of the perimeter of the polar cap from which to calculate its area. The poleward edge of the auroral oval was estimated using the auroral emissions recorded by the Ultraviolet Imager (UVI) on the POLAR spacecraft (*Torr et al., 1995*). The poleward auroral boundary was defined as the latitude poleward of which the image intensity fell below 4.3 photons/cm<sup>3</sup>/s. At times during its orbit the Polar spacecraft did not have a full view of the northern auroral oval. When this occurred the missing part of the polar cap boundary was extrapolated by fitting a curve to the visible part of the boundary.

During a substorm, the polar cap area can decrease by as much as 20% to 30% within an hour (*DeJong and Clauer, 2005*). Thus *DeJong and Clauer (2005)*

adopted the criterion that when the polar cap area changed by less than 10% in one hour convection was steady. To ensure convection was enhanced, the AE index was required to remain above 200 nT for the duration of the SMC interval. They required that these conditions must persist for at least 3 hours. *DeJong and Clauer (2005)* used a time constraint of 3 hours, as compared to the 90 minutes used by *O'Brien et al. (2002)*. This was to reduce the likelihood that the recovery phase of substorms was included in the SMC data set. In the event that Polar UVI could no longer see the auroral oval during the course of a SMC event, its end was determined by looking for substorm signatures in the AL index.

For the years 1997 to 2001 *DeJong and Clauer (2005)* identified 22 SMC events. The average IMF Bz was found to be -4 nT. This is in agreement with past studies, such as *O'Brien et al. (2002)*, which found Bz to be moderately negative during SMC events. *DeJong and Clauer (2005)* also identified two SMC events where the polar cap area increased steadily over 3 hours eventually ending in a substorm. These two events were more consistent with being substorms with very long growth phases.

The use of POLAR UVI to indirectly measure the amount of open flux in the polar cap is an intriguing way to study SMC, but there are drawbacks. Foremost of these drawbacks is that the poleward edge of the auroral oval is only a proxy for the polar cap boundary, but the method does not require absolute areas; rather it relies on the relative changes in area. Polar UVI does not always have a full view of the auroral oval due to its orbit and viewing angle. In addition, during the northern summer months a large portion of the polar cap is immersed in sunlight, which prevents the calculation of the entire perimeter of the auroral oval.

All three quantitative SMC definitions described above were designed to detect SMC but none directly measured convection. Instead, indirect observations were used to quantify convection based on either ground-based magnetometer measurements or auroral luminosity measured by a satellite. Some direct convection measurements have been used to study SMC. *Hughes and Bristow (2003)* used SuperDARN to study two SMC events. *Hughes and Bristow (2003)* focused on the electrically defined Harang discontinuity portion of the convection pattern in the

midnight sector. Their study indicated, for the first time, that Harang discontinuity was present during the SMC. This study was an important first step in incorporating direct convection measurements into the study of SMC but was limited as only two events were examined. Future work using SuperDARN should include larger event sets so a more complete picture of convection during SMC can be developed.

# CHAPTER 5

## EVALUATION OF SMC SELECTION METHODS

SuperDARN directly measures ionosphere convection patterns on a global scale. For this reason the SuperDARN convection maps are an ideal tool with which to study SMC. One must, however, understand the advantages and limitations of SuperDARN before making use of its data.

Because SuperDARN can not measure the entire ionospheric convection pattern, the gaps in the observations are interpolated using spherical harmonic expansion algorithms to deduce the convection pattern that best fits the data obtained by SuperDARN. The interpolation process used to obtain the best fit convection map is constrained by statistical convection maps, and these are parameterised by the IMF conditions at that particular time. When very few data points are obtained, the resultant convection map is usually very similar to the statistical model, which is inherently steady. It would be prudent to use previously developed and accepted methods of SMC selection to determine the properties of SuperDARN data during SMC. A quantitative SuperDARN definition of SMC may be developed out of this process. The global convection maps may also illuminate problems with existing SMC selection methods, which are not based on direct observations of convection.

The SMC intervals in this study were identified using the enhanced convection criterion ( $AE \geq 200$  nT) and the stable magnetotail criterion ( $dAL/dt \geq -25$  nT/min) of *O'Brien et al.* (2002). In contrast, to reduce the likelihood of selecting the recovery phases of substorms, the enhanced convection and stable magnetotail criteria were required to persist for at least 3 hours. This was a compromise between the 1.5 hour minimum SMC time of *O'Brien et al.* (2002) and the 4 - 6 hour duration used by *Sergeev et al.* (1995). It should also be noted that de-spiked AE and AL data

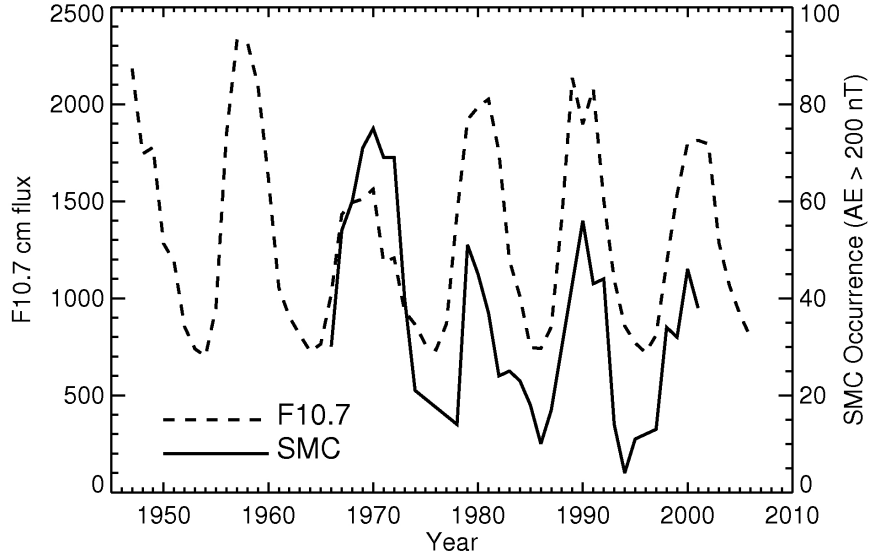


**Figure 5.1:** The solid line is the yearly number of SMC events selected as a function of year. The dotted line is the yearly number of sunspots observed. Sunspot data provided by National Geophysical Data Centre.

were used in this study. The processed data were obtained from R. L. McPherron, who performed a visual inspection to remove data spikes, which were likely due to magnetometer instrument effects (R. L. McPherron, personal communication).

AE and AL data were available for the years 1966-2001, inclusive, with the exception of 1975-1977, 1988, 1989, and 1996. The selection criteria resulted in a total of 1126 SMC intervals. This amounts to one SMC event occurring every 10 days, on average, but the SMC intervals did not occur at regular intervals. SMC occurrence has a strong seasonal dependence, as well as a strong dependence on the solar cycle.

## 5.1 AE Solar Cycle Dependence

The monthly counts of SMC intervals for all available years from 1966 to 2001 is presented in Figure 5.3. More SMC events were detected during the years near solar maximum (1968, 1979, 1990, 2001). The SMC occurrence and solar cycle relationship is more clearly evident in Figure 5.1, in which the sunspot number (dashed line) and SMC occurrence (solid line) vary in phase. The lack of one-to-one correspondence

is of interest and should be investigated further, but is out of the scope of the present study. The increased SMC occurrence at solar max does suggest that the SMC occurrence rate is related to geomagnetic activity. Solar cycle modulation of geomagnetic activity is a well known phenomenon (e.g, *Gonzalez et al.*, 1993). Increased geomagnetic activity is expected during solar maximum.

## 5.2 AE Dependence on Season

The SMC occurrence rate, presented in Figure 5.2, exhibits a seasonal variation, with more SMC events selected in the northern summer months. This seasonal variation occurred during all phases of the solar cycle, and the trend was present each year. There is no corresponding trend in the southern summer months because the AE indices are only a northern hemisphere measurement. The SMC distributions for all available years were combined to form a total annual SMC events distribution, which is presented in Figure 5.3. The strong seasonal dependence is more clearly evident, and the total events distribution is much more smoothly varying than the yearly distributions in Figure 5.2.

The large variation in the number of SMC events as a function season is more likely due to some process other than convection. Studies, such as that by *Ahn et al.* (2000), have reported that ionospheric conductivity causes a seasonal variation in the AE indices, with stronger currents observed in the northern summer. The AU index is most affected by variations in photoconductivity, while the AL index, which is closely related to substorm activity and therefore geomagnetic activity, displays a peak in activity near equinox. This variation in ionospheric conductivity is unfortunate for SMC studies as it makes a constant AE cutoff unsuitable for selecting events with a minimum convection threshold. Appropriate methods must therefore be developed to minimise the effects that conductivity has on SMC event selection using the AE index.

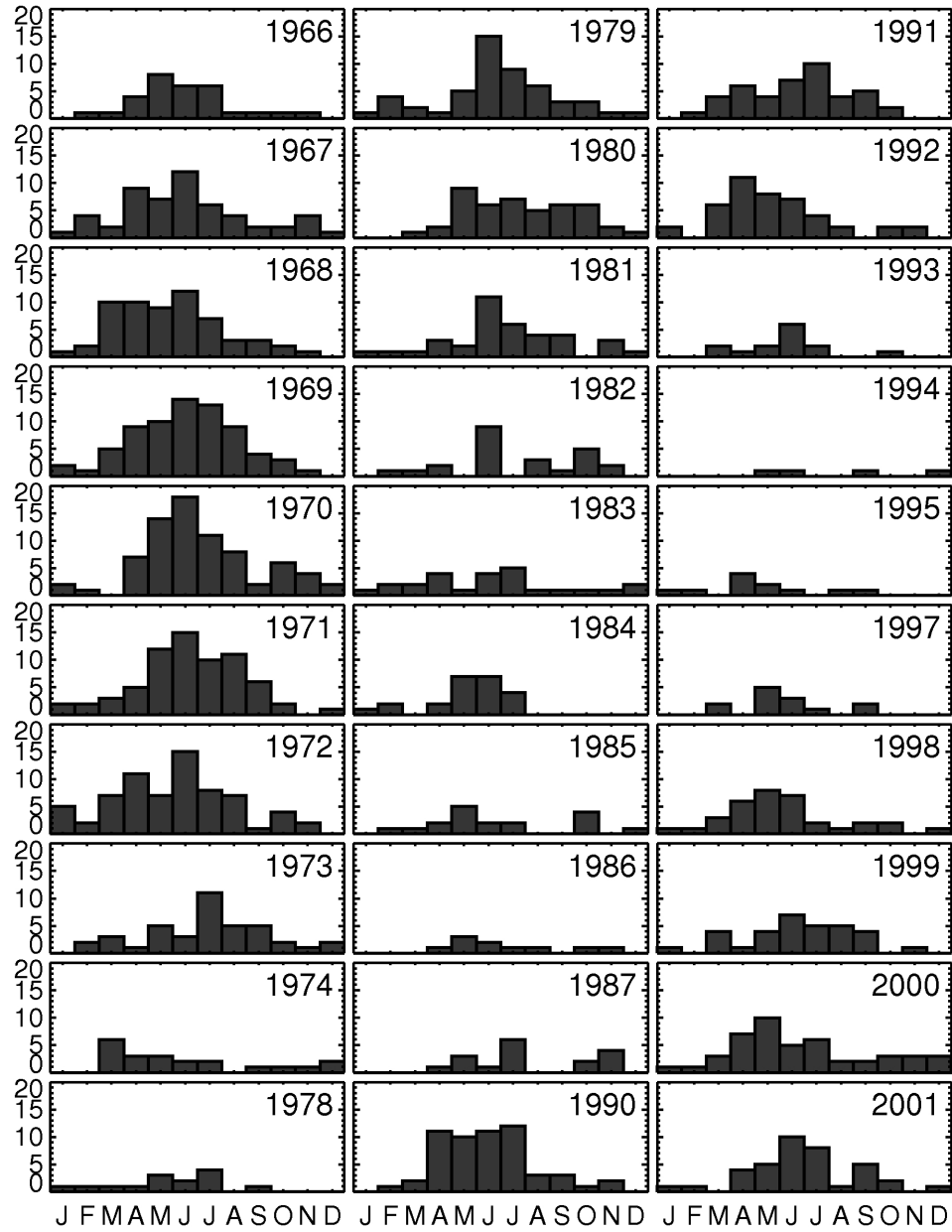


**Figure 5.2:** Occurrence of SMC events for each month for available years from 1966 to 2001 selected with  $AE \geq 200$  nT.

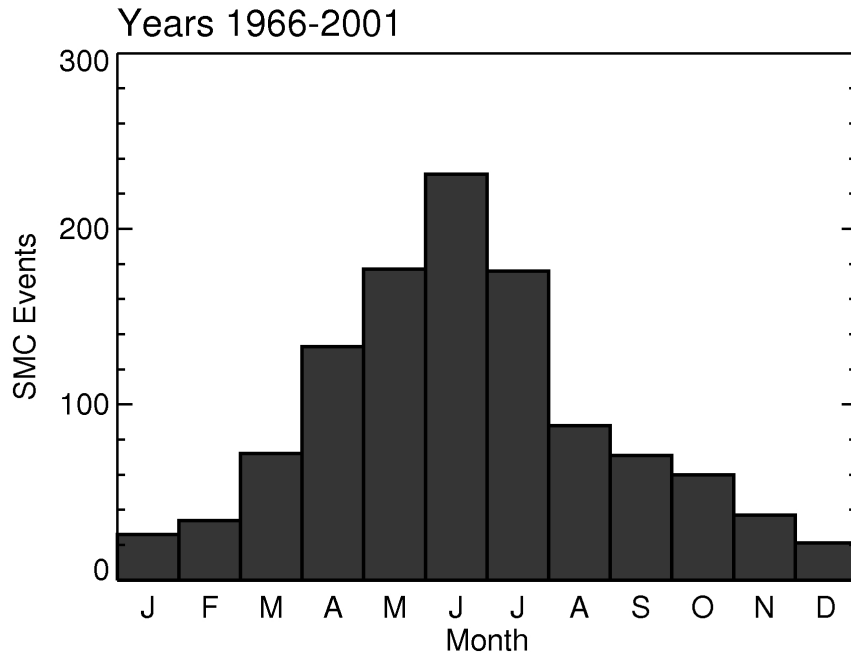


**Figure 5.3:** The total distribution of SMC events selected using the constant AE cutoff of 200 nT.

### 5.3 Improving SMC Selection Criteria

A particular value of AE is dependent on the convection in the magnetosphere and the conductivity of the ionosphere, and the ionospheric conductivity is dependent on season. While the modified method of *O'Brien et al. (2002)* is designed to find intervals of enhanced convection, the annual variation in ionospheric conductivity may be introducing a non-constant minimum convection threshold throughout the year. As a first attempt at minimising the effects of conductivity, a variable AE cutoff function should be developed.

During the winter months the conductivity in the polar ionosphere is at its lowest because the solar zenith angle is large, resulting in a lower rate of photo-ionisation in the upper atmosphere. The strength of magnetospheric convection in the winter must therefore be greater to generate electrojet currents equivalent to those observed in the summer months. In an attempt to quantify convection enhanced above a consistent minimum value throughout the year, the minimum AE value of the modified *O'Brien et al. (2002)* method was varied as a function of year,

with the AE cutoff being lowest in the winter. Many different functional forms for a variable AE cutoff were tried, including a Gaussian and several cosine polynomial functions. All functions that were tested maximised at 200 nT at the northern summer solstice. For each function tested a working total SMC events distribution was produced. To gauge which function produced the “flattest” distribution two tests were devised. The first was the minimum difference test. For all AE cutoff functions tested, the difference between the maximum and the minimum number of events per month was determined for the working total events distribution. The “best” function would have the smallest difference between maximum and minimum. The second test was based on the variance of each function’s total events distribution. The function with the smallest variance of monthly values was deemed the most appropriate. The variable AE cutoff function is a single cosine function raised to a power  $n$ , as follows:

$$AE \geq A \cos^n \left( \frac{(t - 173)\pi}{365} \right) + (200 - A) . \quad (5.1)$$

In the generalised equation  $t$  is the day of the year,  $A$  is the amplitude of the cosine function in units of nT, and the integer exponent  $n$  controls the width of the function. For all integer values of  $n$  between 1 and 10, SMC occurrence distributions were determined for integer values of  $A$  between 0 and 200 nT.

When  $A$  is equal to 0 nT the resulting AE cutoff function will have a constant value of 200 nT, which is the traditional SMC selection criterion. When  $A$  is equal to 200 nT the AE cutoff function peaks at 200 nT at the summer solstice and minimises at 0 nT at the winter solstice. Each AE cutoff function was used to select working SMC events, and a total monthly events distribution was determined for all combinations of  $A$  and  $n$  using all available AE data from 1966 to 2001.

The minimum difference test and minimum variance test were applied to determine which pair of  $A$  and  $n$  values produced the flattest total events distribution for Equation 5.1. Figure 5.4 displays in panel (a) the minimum difference test as a function of  $A$  and  $n$ , and in panel (b) the variance as a function of  $A$  and  $n$ . The minimum value in each plot is indicated by a plus sign. The minimum difference test found the flattest events distribution occurred for  $A$  equal to 107 nT and  $n$  equal to

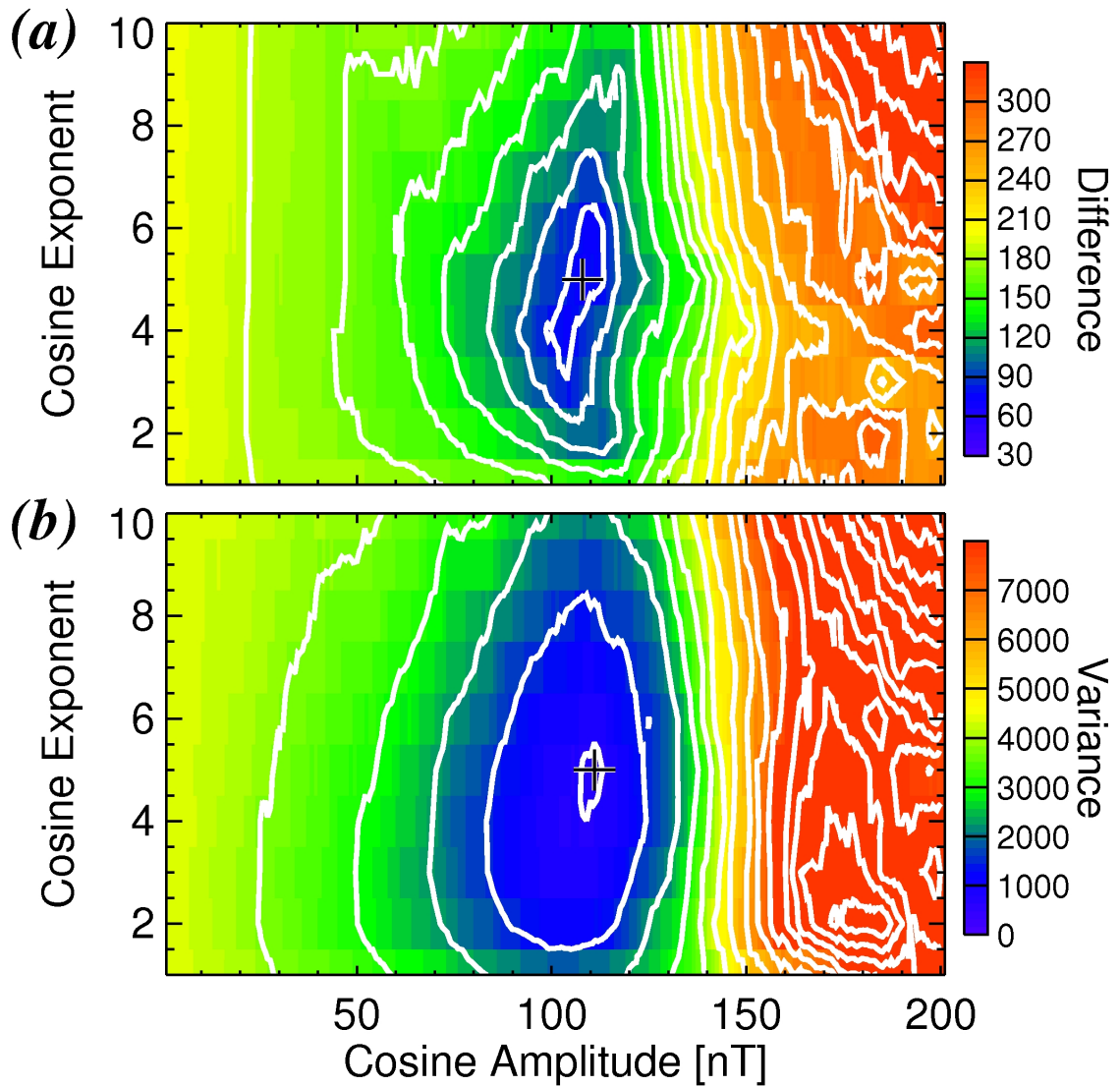


**Figure 5.4:** (a) The difference and (b) the variance of the working “SMC” events distributions resulting from applying the variable AE cutoff function (Equation 5.1) for integer values of cosine exponent  $n$  from 1 - 10 and integer values of cosine amplitude  $A$  from 0 - 200 nT. The plus sign indicates the minimum in both plots.

5. The minimum variance test had the lowest value when  $A$  was equal to 110 and  $n$  was equal to 5. Therefore both tests minimised at nearly identical values of  $A$  and  $n$  and there were not multiple minima for physically realistic values of  $A$  and  $n$ . With the most appropriate values of  $A$  and  $n$  the following variable-AE cutoff function was adopted:

$$AE \geq 110 \cos^5 \left( \frac{(t - 173)\pi}{365} \right) + (90) . \quad (5.2)$$

A word of caution should be noted here. In the winter months the new enhanced convection criterion (Equation 5.2) is as low as 90 nT. Recall that the AE index is obtained by subtracting the quiet-time baseline  $H$  component from the raw magnetometer data, as described in Chapter 3. If this baseline correction is not sufficient, the AE index can appear weakly enhanced for long periods of time. Questionable baselining is more common during times when there are technical difficulties and fewer magnetometers are operating. Most of the AE index data have been thoroughly checked to ensure that baseline problems are removed. However, only provisional data are available for the years 1997 - 2001, so there may be problems during these years. For large AE index values, such as 200 nT, baseline errors are not usually significant, but they can become a problem at lower values of AE. Since the modified AE cutoff of Equation 5.2 has such a low enhanced convection requirement in the winter months, it was necessary to institute a baseline check to ensure that the apparent enhancement present during selected events was the result of convection rather than of a baseline error.

Qualitatively, intervals with baseline errors look different from SMC in that the AU index is much larger than the AL index. Often with baseline errors the AU index never drops to zero but instead remains elevated above a constant value. Figure 5.5 displays the quicklook plot of the AU, AL, AE and AO indices for two different days, October 30, 2001, and December 22, 2000. The data from October 30, 2001, displayed in panel (A) contained two intervals that were deemed SMC by Equation 5.2, one from 4:33 UT until 7:47 UT and a second from 8:23 UT to 11:43 UT. Baseline subtraction was not an issue for these events as AU and AL were roughly the same magnitude and both dropped to zero at 15:30 UT. This indicates

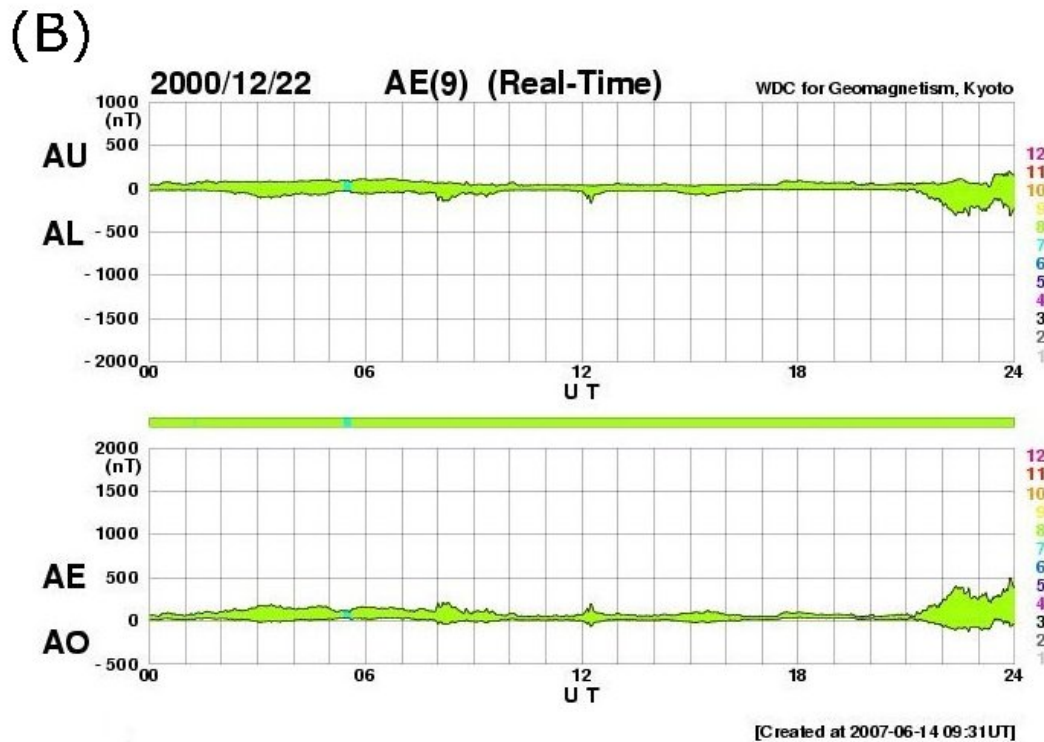
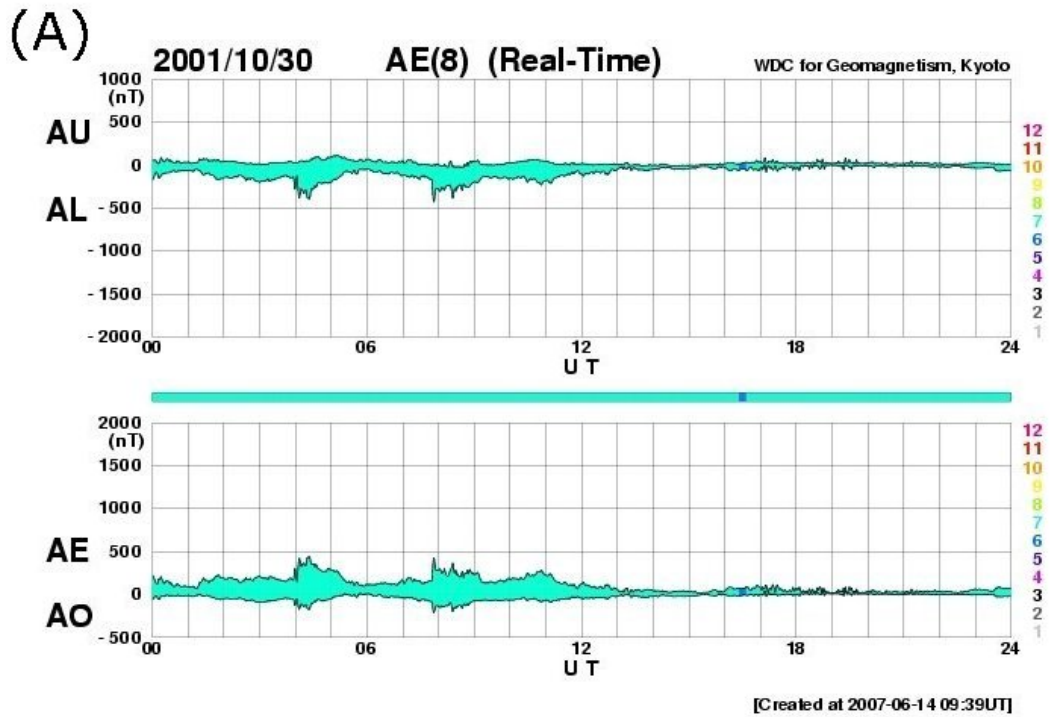


Figure 5.5: (A) An example of AE data with reasonable baseline adjustment, and (B) an example of baseline errors in the AE indices. (AE quicklook plots provided by the World Data Center, Kyoto.)

proper baseline procedure had occurred. In contrast the SMC interval starting at 1:53 UT on December 22, 2000 and ending at 7:55 UT was plagued by baseline problems. This event is pictured in panel (B) of Figure 5.5. Notice, especially between 10 and 21 UT, that the AU index remains enhanced and unusually stable for most of the day, while at the same time the AL index was nearly zero. To ensure a high quality data set visual inspection of the quicklook AE plots was performed for every variable AE SMC event selected in the years 1998 - 2001. In these years of provisional AE data there were 55 rejected events out of a total of 421.

The white histograms in Figure 5.6 are the monthly counts of SMC intervals for all available years from 1966 to 2001 as selected by Equation 5.2. The white histogram in Figure 5.7 is the verified total events distribution when the variable AE cutoff defined by Equation 5.2 was used. Both figures show the seasonal dependence has been greatly reduced. The original distributions have been reproduced in Figure 5.6 and 5.6 for reference. While the total event distribution that resulted from the variable AE cutoff function is relatively flat, a semi-annual variation still remains. This semi-annual variation peaks in the spring and the fall in agreement with the Russell McPherron effect (*Russell and McPherron, 1973*). This trend was noted by *Ahn et al. (2000)* in the AL index. The white histogram in Figure 5.7 also displays strong qualitative agreement with the geomagnetic activity *aa* index in Figure 2.5, which describes average geomagnetic activity.

## 5.4 SuperDARN and Seasonal Effects On SMC

The main purpose behind developing a variable AE cutoff function was to identify SMC consistently, based on a fixed minimum convection threshold. SuperDARN data will now be included to determine how the variable AE cutoff function performs. As a first step, the cross polar cap potential difference (PCPD) was used to quantify convection. SuperDARN convection maps were produced every 2 minutes for the duration of each SMC. A delay of 60 minutes was applied to the IMF data from the ACE Magnetic Field Instrument. The ACE spacecraft is located at

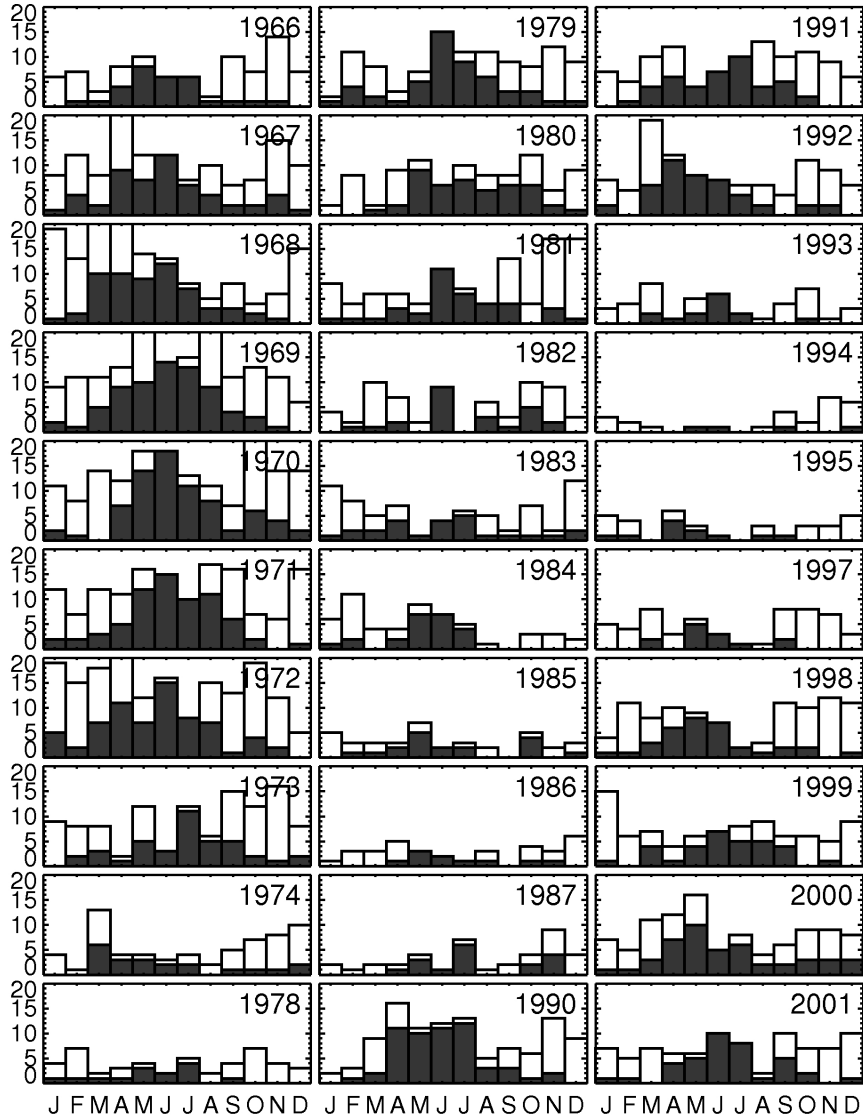


**Figure 5.6:** The black histograms are the occurrence of SMC events per month for available years from 1966 to 2001 selected with  $AE \geq 200$  nT. The white histograms are the occurrence of SMC events per month for available years from 1966 to 2001 selected using the variable-AE cutoff function in Equation 5.2.

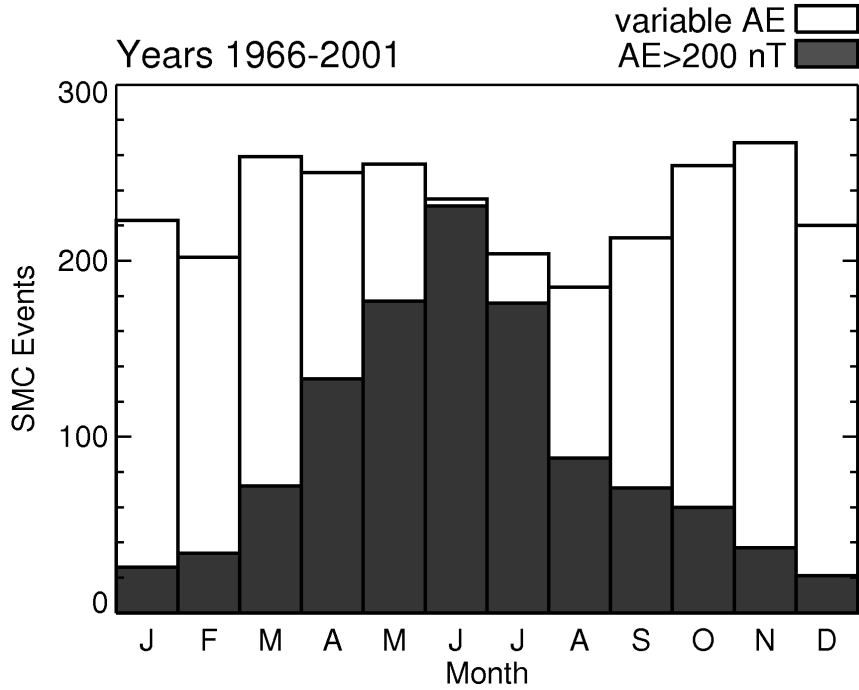


**Figure 5.7:** The dark histogram is the total distribution of SMC events selected using a constant AE cutoff of 200 nT. The white histogram is the total distribution of SMC events selected using the variable AE cutoff function from Equation 5.2, with  $A = 110$  and  $n = 5$ .

the L1 lagrangian point, which is approximately 1.5 million kilometers upstream of the Earth along the Earth-Sun line. The polar cap voltages from the individual convection maps were combined to determine the average value of PCPD for each SMC interval. The average PCPD value for an event is represented by a black dot in Figure 5.8. The black line in each panel represents a sliding mean of the PCPD calculated on the first day of each month and includes two months of PCPD data. The dashed line in each plot represents 45 kV.

The mean interval voltages for SMC events selected using  $AE \geq 200$  nT are presented in panel (a) of Figure 5.8, and panel (b) of Figure 5.8 displays the voltages of the SMC events selected using the variable AE cutoff function of Equation 5.2. To provide context, it is useful to know what SuperDARN typically observes. To this end, a list of randomly selected events was created by changing the date of properly identified SMC events using a random number generator. The SMC list was used as a starting point, in order to maintain some statistical properties of the interval

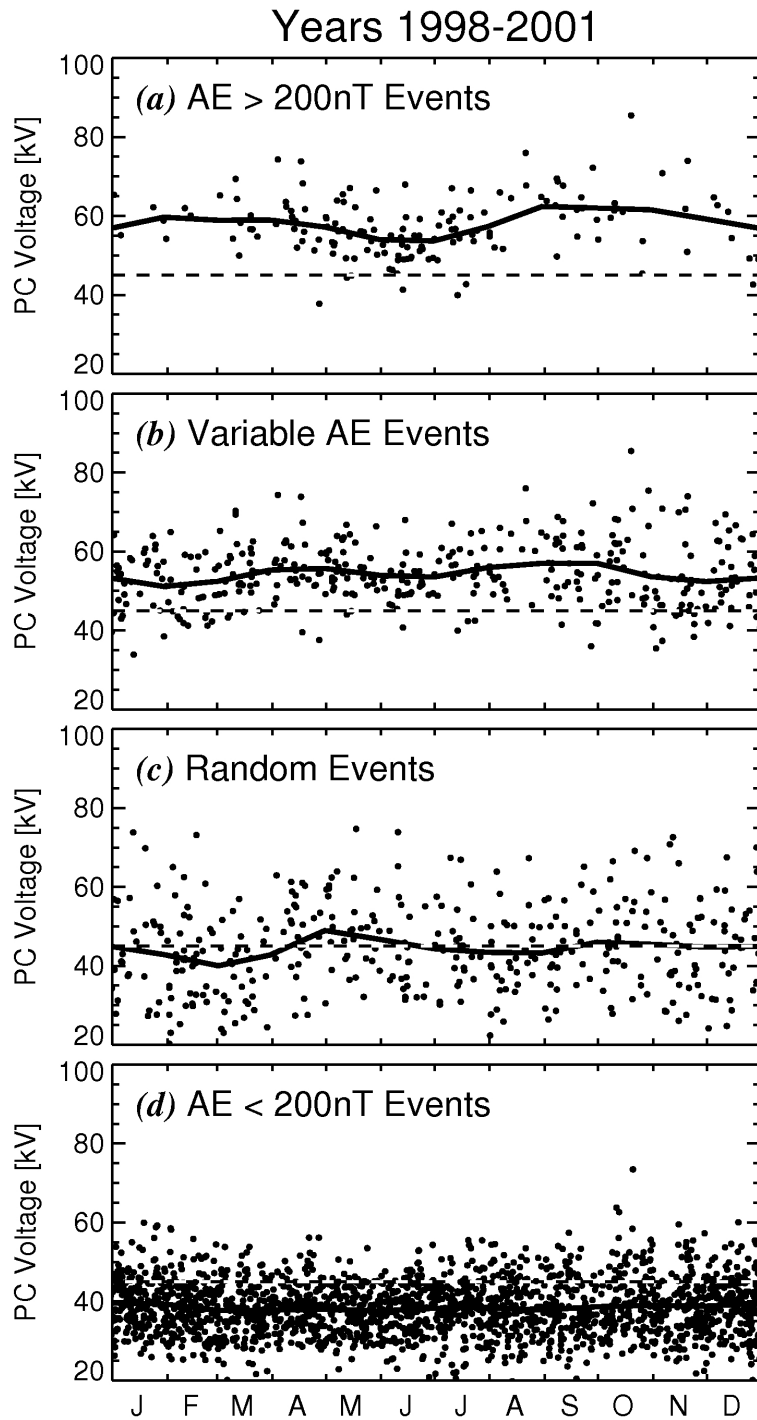


**Figure 5.8:** Average interval values of SuperDARN PCPD for: (a) SMC events selected using  $AE \geq 200$  nT, (b) SMC events selected using Equation 5.2, (c) randomly selected events, and (d) events selected using  $AE \leq 200$  nT. The dashed line represents 45 kV, the solid line is a sliding 2-month average of PCPD.

set, such as event duration. The randomly selected events were distributed evenly throughout the year, and they are presented in panel (c) of Figure 5.8.

The mean voltages during the random intervals are predominantly between 20 and 60 kV, and the average of the 2-min map voltages is 45 kV. In contrast, of the events selected using a constant AE cutoff, only 7 were below 45 kV. Furthermore, 90% of the 18379 individual 2-min map voltages for the SMC intervals in panel (a) exceeded 45 kV. The SuperDARN PCPD data therefore confirms that the SMC events selected using a constant AE cutoff 200 nT are intervals of enhanced convection.

The sliding mean voltage line in panel (a) suggests that the summer SMC events have lower voltages, which indicates weaker summer convection. The randomly selected events of panel (c) did not seem to display this seasonal variation. This could be construed as evidence that conductivity is affecting SMC events selection in panel (a). This evidence is not conclusive, since there is an unquantified uncertainty in the voltages derived from SuperDARN measurements. Further work will need to be needed to address the significance of the trend in panel (a).

The variable AE cutoff events also displayed enhanced convection, compared to the randomly selected events, with 86% of the 439 variable-AE SMC events having a mean event voltage above 45 kV. Of the 55105 2-min map voltages used to calculate the average PCPD, 80% were above 45 kV. The variable AE cutoff function therefore preserves enhanced convection throughout the year, while increasing the number of events in the winter months. The events selected in the winter months had similar voltages to those selected in the summer, providing some evidence that the variable AE cutoff selects events with a constant minimum convection threshold.

As a further check of the strength of convection quantified by the AE indices, an investigation of “non-enhanced” intervals was performed. Events in panel (d) of Figure 5.8 were selected for which  $AE < 200$  nT and  $dAL/dt \geq -25$  nT/min were satisfied for at least 3 hours. These events were selected to contrast the SMC events in panels (a) and (b). In panel (d) 84% of the 1967 events had an average voltage below 45 kV. Panel (d) events are therefore a subset of SuperDARN data that are

not enhanced.

SuperDARN has provided evidence that convection is enhanced during SMC and suggests that the variable AE cutoff function selects events with enhanced convection and a fixed minimum convection threshold. Unfortunately, this evidence is not conclusive since the uncertainties in SuperDARN measurements are not quantified. It is therefore appropriate to find additional evidence to support the hypothesis that the seasonal dependence in the  $AE \geq 200$  nT events is the result of ionospheric conductivity. Based on the physical process of photo-ionisation that was described in Chapter 3, one may develop a model to describe the effects conductivity have on SMC selection.

## 5.5 Conceptual Model of Conductivity Effects on SMC Selection

The plasma production function in Equation 3.21 will be the basis of a conceptual model of ionospheric conductivity effects, from which to derive an analytical SMC events distribution based solely on the annual variations of conductivity. If the suppression of events in the winter months using a constant AE cutoff is caused by the conductivity variation, then the modelled distribution should have strong qualitative agreement with Figure 5.3. The conceptual model is based on probabilities, in particular the effect that the ionospheric conductivity has on the probability of observing an AE index value above 200 nT. In this model photo-ionisation processes are considered. Contributions from energetic particle precipitation, such as during a substorm, are neglected.

Several simplifying assumptions were used in this conceptual model. The first was to assume that convection is constant in the magnetosphere. This assumption is intended to decouple the solar wind driver and the ionospheric conductivity effects. With this assumption, the “steadiness” requirement of SMC (i.e.,  $dAL/dt \geq -25$  nT) becomes irrelevant. When convection is constant  $dAL/dt$  is zero at all times. The next assumption is that all SMCs have the same duration. The length of each SMC

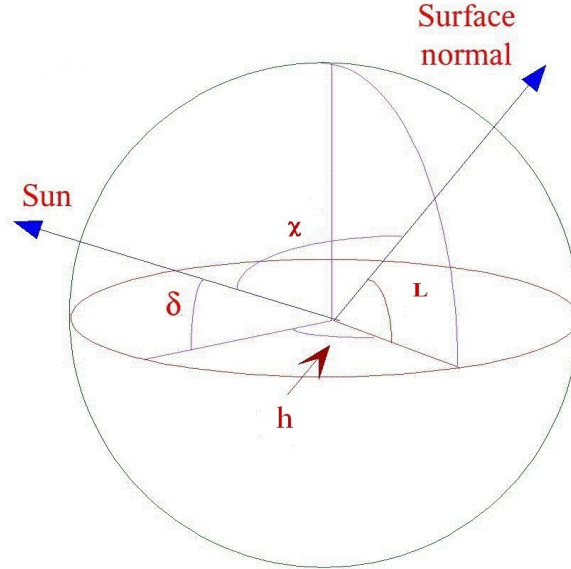


**Figure 5.9:** The geometry of the Sun-Earth system in spherical coordinates, where  $\delta$  is the declination angle,  $h$  is the hour angle,  $L$  is the latitude, and  $\chi$  is the solar zenith angle.

interval was fixed at 3 hours. The distribution of magnetometers was also idealised in this model despite that, in reality, the magnetometers used to derived the AE indices are not evenly spaced, as can be observed in Figure 4.2. The twelve idealised magnetometers are evenly spaced in longitude and situated at the same geographic latitude. The time dependence of the solar zenith angle was also simplified in this model, but before proceeding to the modelled SMC events distribution, the solar zenith angle should be examined in more detail.

The solar zenith angle,  $\chi$ , is defined as the angle at the centre of the Earth subtended by the vector pointing towards the Sun and the surface normal vector passing through the point on the surface where  $\chi$  is to be determined (see Figure 5.9). This differs from the approach used in Chapter 3, where  $\chi$  was determined at ionospheric altitudes using the flat Earth approximation. Due to the astronomical distance involved, the Sun's light rays are effectively parallel at Earth so both angles converge to the same value.

The latitude angle of the point on the Earth's surface where the solar zenith angle is to be determined is denoted by  $L$ . The hour-of-day angle is given by  $h$ , and  $\delta$  is the declination angle. These angles are illustrated in Figure 5.9. The solar

zenith angle is related to the other angles as follows:

$$\cos(\chi) = \cos(L) \cos(\delta) \cos(h) + \sin(L) \sin(\delta) . \quad (5.3)$$

The declination angle  $\delta$  depends on the day of year and varies between  $\pm\delta_{max}$ , which is the maximum declination angle and is equal to  $23.5^\circ$ . The hour angle  $h$  depends on the hour of the day  $t$  (from 0 to 24). The hour of the day is set to zero at midnight. The expanded equation for the solar zenith angle becomes:

$$\begin{aligned} \cos(\chi) = \cos(L) \cos \left( \delta_{max} \cos \left( \frac{2\pi(x+10)}{365} \right) \right) \cos \left( \frac{\pi t}{12} \right) \\ + \sin(L) \sin \left( \delta_{max} \cos \left( \frac{2\pi(x+10)}{365} \right) \right) , \end{aligned} \quad (5.4)$$

where  $x$  is the day of year, and the offset of 10 days ensures that the function maximises at the summer solstice. Notice that  $\cos(\chi)$  in Equation 5.4 varies on two primary time scales: (1) with time of day by the hour angle  $h$ , and (2) with day of year by the declination angle  $\delta$ . For the purposes of this conceptual model, Equation 5.4 can be simplified by assuming the hourly variations of the solar zenith angle are less significant than the seasonal variation. Furthermore, neglecting changes in the solar zenith angle on small time scales should also be valid in this model because convection has been constrained to be constant. If the convection pattern is constant then the distribution of electrojet currents will not change during a day, implying that the location of the maximum current densities in the electrojets will not change on a scale of an hour. In other words, if the greatest magnitude in the eastward electrojet is located at 18 UT, it will remain located at 18 UT. The AE indices are a measure of the maximum currents in the convection electrojets, and the magnetometers closest to the current maxima will contribute to the AE indices. Therefore if the maximum currents are always located at the same location in MLT, the hour angle in Equation 5.3 will be constant. Due to the simplifying assumptions, Equation 5.4 reduces to:

$$\cos(\chi) = C_0 \cos \left( L + \delta_{max} \cos \left( \frac{2\pi(N+10)}{365} \right) \right) , \quad (5.5)$$

where  $C_0$  is a constant. Assuming a constant convection pattern, the AE current

intensity scales up or down according to the conductivity in the ionosphere, and the conductivity is proportional to the electron density (Equation 3.47). In Section 3.3 it was shown that the maximum electron concentration at any point in the ionosphere is related to the solar zenith angle as follows:

$$n_{max} \propto \sqrt{\cos(\chi)} . \quad (5.6)$$

Equation 5.5 therefore describes how conductivity will affect current strength as a function of season. Electrojet currents, through the AE indices, are used to quantify the level of convection in the magnetosphere. For a SMC event to be selected the traditional methods require the AE index to be above a set minimum value. For the AE index to be large, the AU index must be above a minimum threshold and the AL index must be below a maximum negative threshold. The chance of this occurring will depend both on convection and on ionospheric conductivity, as the AU and AL indices are functions of these two parameters. In a statistical sense, the probability that AU is above a minimum threshold depends on the overhead ionospheric conductivity which is proportional to Equation 5.5, and on the amount of convection in the magnetosphere. Similarly, the probability that AL has a large magnitude is dependent on the ionospheric conductivity overhead, as well as on the amount of convection. For the AE index to be above a minimum threshold of 200 nT both AU and AL must have appropriately large magnitudes. The probability that AE is above a minimum threshold is the combined probability that both AU and AL exceed their thresholds:

$$P(AE \geq 200 \text{ nT}) = P(AU \geq AU_{min}) \cap P(AL \leq AL_{max}) . \quad (5.7)$$

If  $P(AU \geq AU_{min})$  and  $P(AL \leq AL_{max})$  were independent,  $P(AE \geq 200 \text{ nT})$  would simply be the product of these two probabilities. Unfortunately these probabilities are not independent, as they share a common driver, the IMF. Without independence a simple equation describing  $P(AE \geq 200 \text{ nT})$  cannot be written. Fortunately, in this model convection has been constrained to be constant, which means that AU and AL no longer share a common cause. This constraint implies that the IMF,

which drives the invariable convection pattern, is itself unvarying. In other words, AU and AL are independent, as long as convection is constant.

To illustrate this concept further, consider the following analogy. Imagine two rose bushes in neighbouring gardens. The probability that the first rose bush flowers (Event 1) is dependent on the amount of rainfall (Event 0), while the probability that the second rose bush flowers (Event 2) also depends on the amount of rainfall. Both events have a common cause: Event 0. Therefore Event 1 and Event 2 are not independent. If, however, rainfall is constrained to be constant, Event 1 will only depend on the conditions in the first garden, such as soil nutrient content or care given by the owner. The same will be true for the second garden. Thus, Event 1 and Event 2 are conditionally independent, given Event 0 is constant. This rainfall analogy illustrates how the independence of AU and AL can be considered to be conditionally independent given a constant convection pattern. Because of this independence, the combined probability can be written as the product of the individual probabilities. Therefore the probability of AE being greater than 200 nT can be written as follows:

$$P(AE \geq 200 \text{ nT}) = P(AU \geq AU_{min})P(AL \leq AL_{max}) . \quad (5.8)$$

This conceptual model has reduced the variability in the AE currents to variability in ionospheric conductivity. Since the intensity of the AE currents varies with ionospheric conductivity directly, the probability of observing a certain AE value will also vary in this manner. The AU and AL probabilities will vary as  $\sqrt{\cos(\chi)}$ , so the combined probability for AE becomes:

$$P(AE \geq 200 \text{ nT}) \propto \cos(\chi) . \quad (5.9)$$

Thus the probability that  $AE \geq 200 \text{ nT}$  is known as a function of season, assuming that convection is constant. Without this assumption it would not have been possible to develop this conceptual model. It is therefore important to provide some evidence to suggest that this is a valid assumption for SMC. Based on the probability treatment above, AU and AL should be uncoupled during times of constant

convection, but during times of unstable convection the AU and AL indices should show a level of dependence.

In order to investigate this dependence quantitatively, the correlation coefficient of AU and AL was calculated for SMC and non-SMC times. The correlation between AU and AL for  $AE \geq 200$  nT SMC events for the years from 1966 to 2001 was found to be, on average, 0.162. For the SMC events selected using the variable AE cutoff function the average correlation was 0.288. In contrast, the correlation coefficient for all times from 1966 to 2001 was found to be 0.589. The lower correlation between AU and AL during SMC times supports the assumption of constant convection in the conceptual model.

The above work has provided the foundation with which to derive a theoretical SMC distribution based solely on the probability of observing a particular value of AE. According to Equation 5.9, the chance that any AE measurement is greater than 200 nT is proportional to  $\cos(\chi)$ . In addition to this, according to the model for an event to be deemed SMC the AE index must be greater than 200 nT for three hours. The next stage of the model is to consider the probability that  $AE \geq 200$  nT for 180 measurements in a row, as AE is determined every minute.

For the answer to this question, one should consider the statistics of discrete random variables. In this model there are two discrete random variables. The first will be called X, and it is equal to 1 if  $AE \geq 200$  nT and 0 if  $AE \leq 200$  nT. The probability that X is equal to 1 is proportional to  $\cos(\chi)$ , while the probability that X is equal to 0 is proportional to  $1 - \cos(\chi)$ . The second discrete random variable defined is Y, which corresponds to the time when a pair of magnetometers contributes to AE. For each measurement, Y, there are two possible values for X. One could measure  $AE \geq 200$  nT ( $X=1$ ) or  $AE \leq 200$  nT ( $X=0$ ). If one wanted to find the chance that  $X=1$  for 180 measurements in a row, one must sum the all the probabilities from  $Y=0$  to  $Y=180$  for  $X=1$ , with each probability being proportional to  $\cos(\chi)$ . Since the day time variations have not been included, the  $\cos(\chi)$  term can be factored out of the sum and the resultant probability is simply  $\cos(\chi)$  multiplied by a constant. Therefore the probability that any series of AE measurements made

by a pair of magnetometers are greater than 200 nT is proportional to  $\cos(\chi)$ . This seems to indicate that the probability that any 3 hour interval is SMC is proportional to  $\cos(\chi)$ , but this is not necessarily the case, since the pair of magnetometers that contribute to AE can change during the 3 hour interval.

Because of the constant convection assumption in the conceptual model, the electrojet current system is fixed with respect to the Earth-Sun line. The Earth, on the other hand, rotates with respect to the Sun, so the magnetometers closest to the maximum AE currents, and therefore the magnetometers contributing to AE, change over time. Consider two different pairs of magnetometers contributing to the AE index over a 3 hour time interval. For this time period to be deemed SMC both pairs must contribute  $AE \geq 200$  nT. Or in other words pair 1 *and* pair 2 must both contribute an AE index greater than the cutoff of 200 nT. The probability that pair 1 contributes AE values greater than 200 nT is independent of what pair 2 contributes. Because of this, the probability that a 3 hour interval will be SMC is the product of the probabilities that each individual pair contributes  $AE \geq 200$  nT at some time during those three hours. Therefore, when two pairs of magnetometers contribute to the AE index over a three hour interval the probability of the AE index being greater than  $AE \geq 200$  nT for the length of that interval is proportional to  $\cos^2(\chi)$ .

Because the length of the idealised SMC was set to be 3 hours, a maximum of 8 SMC events can occur in one day. It is assumed that the same number of pairs of magnetometers contribute to AE during each event. Because hourly variations in  $\chi$  have been neglected (by neglecting the hour angle  $h$ ), each three hour interval will have the same probability of success. This kind of experiment is called a Bernoulli trial. Bernoulli trials are any experiments in which  $n$  trials are made with the probability  $p$  of success in any given trial. The probability distribution of a Bernoulli trial is described by a binomial distribution. Therefore in the case of this model each day of the year is a Bernoulli trial and there will be a binomial distribution that describes the chances of between 0 and 8 SMC events occurring each day. The binominal distribution will have a probability that is proportional to  $\cos^n(\chi)$ , where  $n$  represents the number of magnetometer pairs involved in the SMC measurement.

Since  $\cos^n(\chi)$  is dependent on season, the expected number of SMC events per day will change. In the summer months the expected number of SMC events per day will be higher. The tools are now in place to construct a modelled total SMC events distribution.

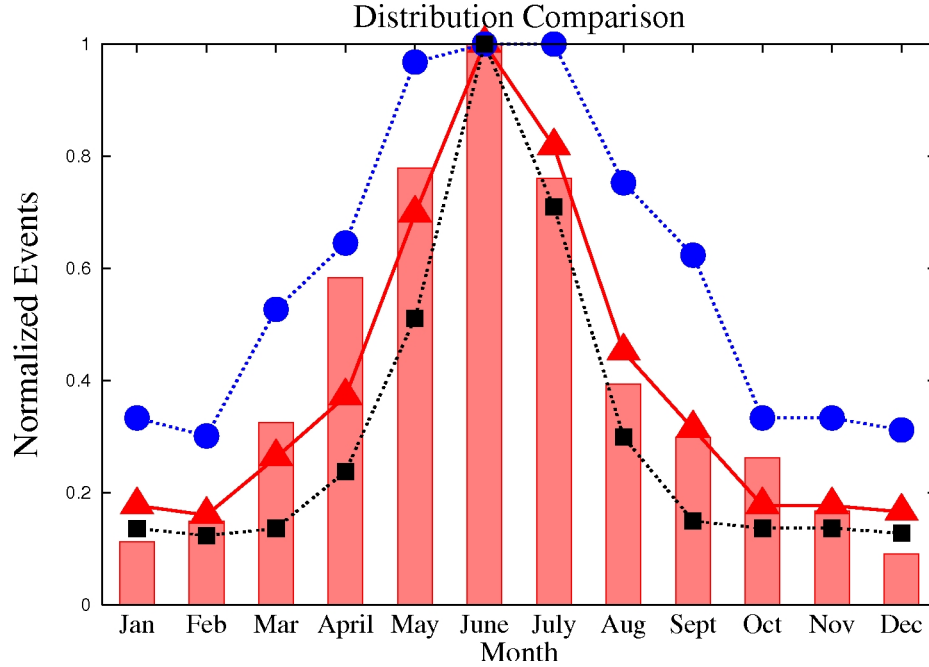


**Figure 5.10:** The red histogram represents the total events distribution selected using a constant minimum cutoff of 200 nT. Each line represents a theoretically derived distribution with monthly values represented by each lines respective symbol. The blue distribution was obtained with probabilities proportional to  $\cos^2(\chi)$ . The red distribution was obtained with probabilities proportional to  $\cos^5(\chi)$ . The black distribution was obtained with probabilities proportional to  $\cos^{10}(\chi)$ .

The modelled distribution was built by first calculating the expected number of SMC events for each day of the year. Then a total events distribution was formed simply by adding up the expected number of SMC events from each day of a given month to find the expected number of SMC events per month. The distributions that were obtained for various values of  $n$ , and these agreed very well with the experimental distribution. The comparison is pictured in Figure 5.10. The experimental total events distribution is represented by the red histogram. The theoretical total events distribution found using a probability proportional to  $\cos^2(\chi)$  is represented

by the blue line, with monthly number of events being represented by blue dots. The distribution obtained from the  $n = 2$  model was too wide and too large in the winter months. Recall, that the power of the cosine term is controlled by the number of pairs of stations that contribute to AE over a 3 hour interval. Because a power of two is too low, it seems likely the  $n = 2$  model underestimates the number of magnetometers that contribute to AE over a three hour interval. A distribution was constructed with probabilities proportional to  $\cos^{10}(\chi)$ , and it is represented by the black line, with monthly values represented by black squares. In contrast to the  $n = 2$  distribution, the  $n = 10$  distribution was too narrow and was too low in the winter months. This is not unexpected, however, since the Earth will not rotate over 10 pairs of equally spaced magnetometers in 3 hours. Hence the number of pairs of magnetometers that contribute to AE over a 3 hour interval is expected to lie somewhere between 2 and 10.

The cosine power was varied from 2 to 10 until a distribution that best agreed with the experimental distribution was found. The  $\cos^5(\chi)$  model provided an events distribution that most resembled the actual events distribution obtained from the measured AE index data. The  $\cos^5(\chi)$  modelled distribution is displayed in Figure 5.10 as the solid red line with red triangles. The model therefore implies that 5 pairs of magnetometers contribute to the AE index over the course of a three hour interval. This is not entirely unexpected since  $\cos^5(\chi)$  was the best empirical choice for a variable AE cutoff function. Figure 5.11 displays the idealised magnetometer array in panel (a) at time  $t=0$ . For illustrative purposes only, physically realistic locations were chosen for the maximum AU and AL electrojet currents, and these are indicated in panel (a) of Figure 5.11. The magnetometers closest to these locations will constitute the pair contributing to the AE measurements. Panel (b) of Figure 5.11 displays which magnetometers contribute to AE over a three hour interval starting at time  $t=0$ . Notice that 5 pairs can contribute to the AE index over the three hour interval.

The analytical distribution constructed with  $\cos^5(\chi)$  agreed well with the experimental distribution for most of the year. The weakest agreement was in months

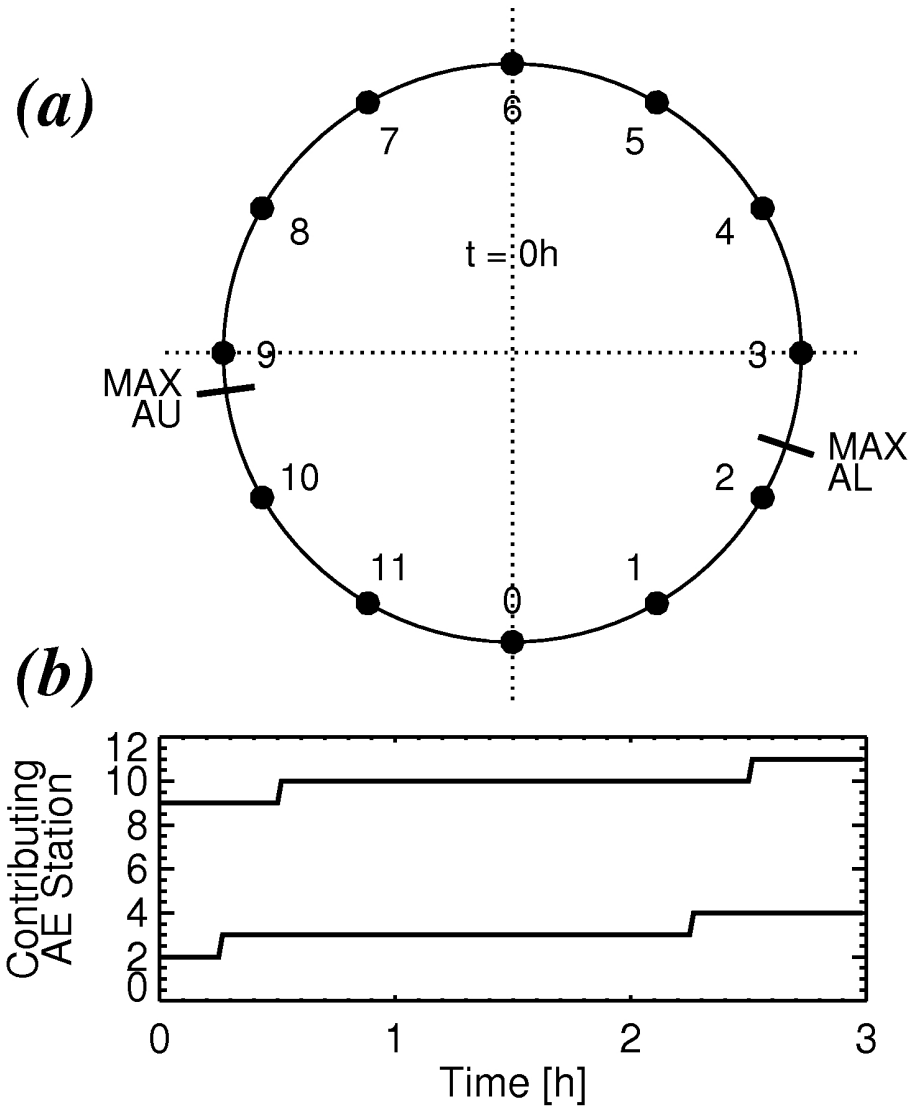


**Figure 5.11:** (a) The idealised magnetometer array at time  $t=0$  with the locations of the maximum AU and AL electrojet current densities. (b) The number of pairs of magnetometers that will contribute to AE over a three hour interval beginning at time  $t=0$ .

near equinox, particularly in April and October. This could be due to the Russell-McPherron affect (*Russell and McPherron, 1973*), which can not be included in this model as long as convection is restricted to be constant. Overall, however, the two distributions displayed agree very well, thus providing supporting evidence that the trend displayed in the number of SMC events per month selected by the  $AE \geq 200$  nT threshold is the result of variable conductivity in the ionosphere.

# CHAPTER 6

## STATISTICAL STUDIES OF SMC

Based on the evidence provided by SuperDARN, as well as by the conceptual model, the variable AE cutoff of Equation 5.2 identifies SMC events based on a consistent minimum convection threshold. Properties of the sets of events presented in Chapter 5 will be examined statistically in Chapter 6. This approach will provide an overview of activity in the magnetosphere during SMC. The conditions during the variable-AE SMC events selected using Equation 5.2 will be compared to the  $AE \geq 200$  nT events selected using the modified method of *O'Brien et al.* (2002). The two test populations will also be examined to discover if the conditions in the magnetosphere during SMC events are unique to SMC. These test populations were identified in Chapter 5. The first test population is made of randomly selected intervals, and the second is the non-enhanced steady events selected with  $AE \leq 200$  nT.

### 6.1 Superposed Epoch Study

The first statistical approach allows the evolution of conditions during SMC to be examined in detail. This method presented is a superposed epoch analysis in which all events are combined relative to the event onset time - the zero epoch time. All events in a particular set will be represented as a cumulative distribution. All cumulative distributions presented in this section will include six lines (95%, 80%, 65%, 50%, 35%, 20%, and 5%). Each line represents the value below which that particular percentage of the total number of events occur. For example the 50% line indicates that half of all the events lie below this line for any given epoch time.

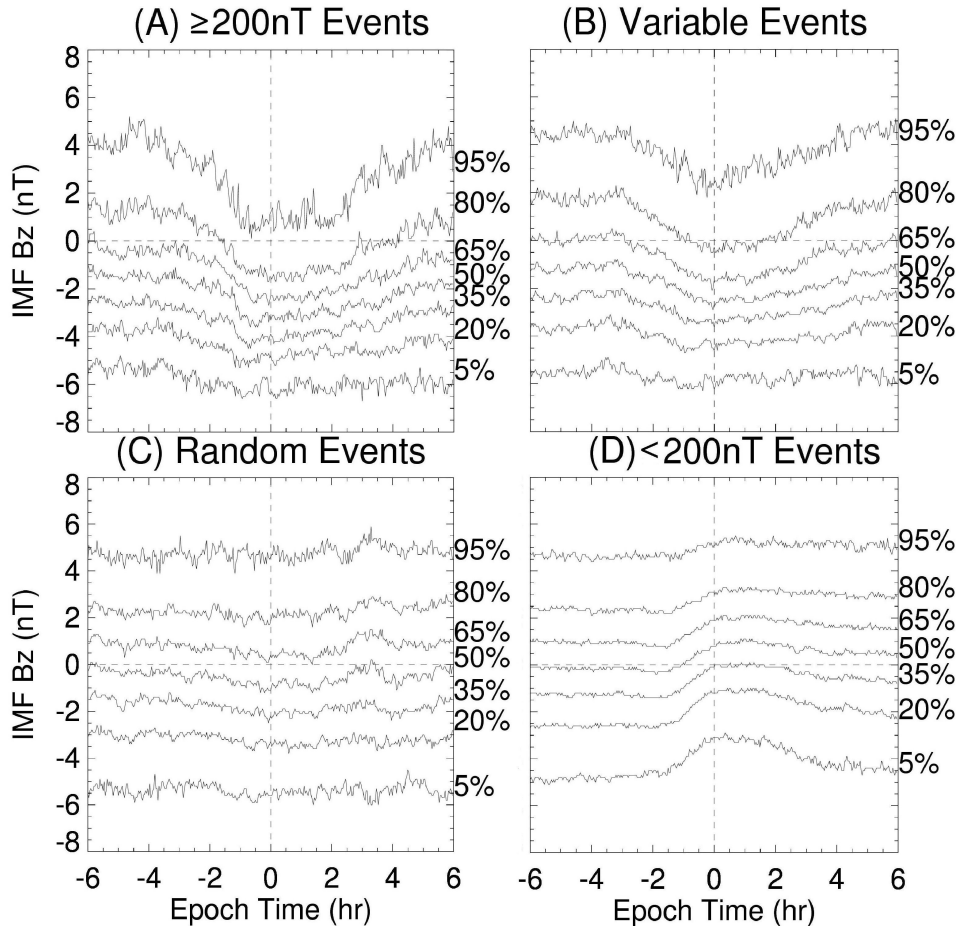


**Figure 6.1:** Cumulative distributions of IMF Bz as a function of superposed epoch time for (a)  $AE \geq 200$  nT SMC events, (b) Variable-AE SMC events, (c) randomly selected events, (d) non-enhanced events with  $AE < 200$  nT.

### 6.1.1 Interplanetary Magnetic Field Conditions

Consider the behaviour of the IMF Bz component as a function of epoch time, since IMF Bz is an important driver of convection in the Earth's magnetosphere. The IMF Bz data that were analysed were obtained by the ACE satellite. For this statistical study, the IMF data were shifted by 60 minutes to account for the travel time of the solar wind conditions from the ACE satellite to the Earth's magnetopause. The value of 60 minutes is based on the simple ballistic delay for particles that typically have a radial velocity from the Sun of 400 km/s. Changes in the solar

wind speed are expected to lead to variation in the delay times of the events, and it is expected that errors of up to 15 minutes could occur in a few cases. The cumulative distributions of IMF Bz are presented in Figure 6.1. In panel (A) are the SMC events selected using  $AE \geq 200$  nT. In panel (B) are the SMC events selected using the variable AE cutoff function of Equation 5.2. Roughly two hours before the onset of the SMC events, the IMF Bz component decreased for both SMC events in panel (A) and (B). The IMF Bz component in panel (A) dropped by roughly 2 nT for the percent lines 80%, 65%, 50%, 35% and 20%. The 95% line dropped by almost 4 nT, while the 5% dropped by 1 nT. After onset IMF Bz gradually increases until at 6 hours after onset it is roughly equivalent to the initial IMF Bz value observed at 6 hours before onset. For events selected using Equation 5.2, IMF Bz followed the same general trend as those events selected using a constant AE cutoff function, the difference being that the trend was more gradual for the variable AE cutoff SMCs. In panel (B) the 95%, 80% and 65% lines dropped by 2 nT. The 50%, 35%, and 20% lines dropped by roughly 1.5 nT. The 5% line dropped 1 nT. One interesting thing is that not all the events in panels (A) and (B) had a negative IMF Bz component. The 95% line and 80% line did not dip below zero for the variable selection method, while the 95% line did not drop below zero for the cumulative distribution in panel (A). Therefore 20% of the SMC events selected by Equation 5.2 and 5% of events selected by the modified method of *O'Brien et al.* (2002) did not have a negative IMF Bz component at onset. This could be due to a strong IMF By component playing a role in driving convection in the magnetosphere. On average, SMC events from both selection methods appear to be driven by a moderately negative IMF Bz component, with the  $AE \geq 200$  nT events occurring under more strongly negative IMF Bz conditions. This is in agreement with previous SMC studies such as those by *DeJong and Clauer* (2005), *O'Brien et al.* (2002) and *Sergeev et al.* (1995). All of these papers concluded that SMC occurred when IMF Bz was moderately negative. This trend of IMF Bz decreasing before onset appears to be specific to the SMC events, because the randomly selected events in the panel (C) of Figure 6.1 show no discernable decrease before or after onset. In contrast,

the “non-enhanced”  $AE \leq 200$  nT events in panel (D) displayed the opposite trend. The cumulative distribution lines in panel (D) increased significantly by about 1 nT leading up to the zero epoch time. This contrast adds further support to the notion that negative IMF Bz drives convection. One might even say that a northward turning of the IMF during steady conditions effectively suppresses convection in the magnetosphere, but this requires much more investigation in future studies. It should be noted that the lower variability of the lines in panel (D) is due to better statistics, as many more “non-enhanced” events selected.

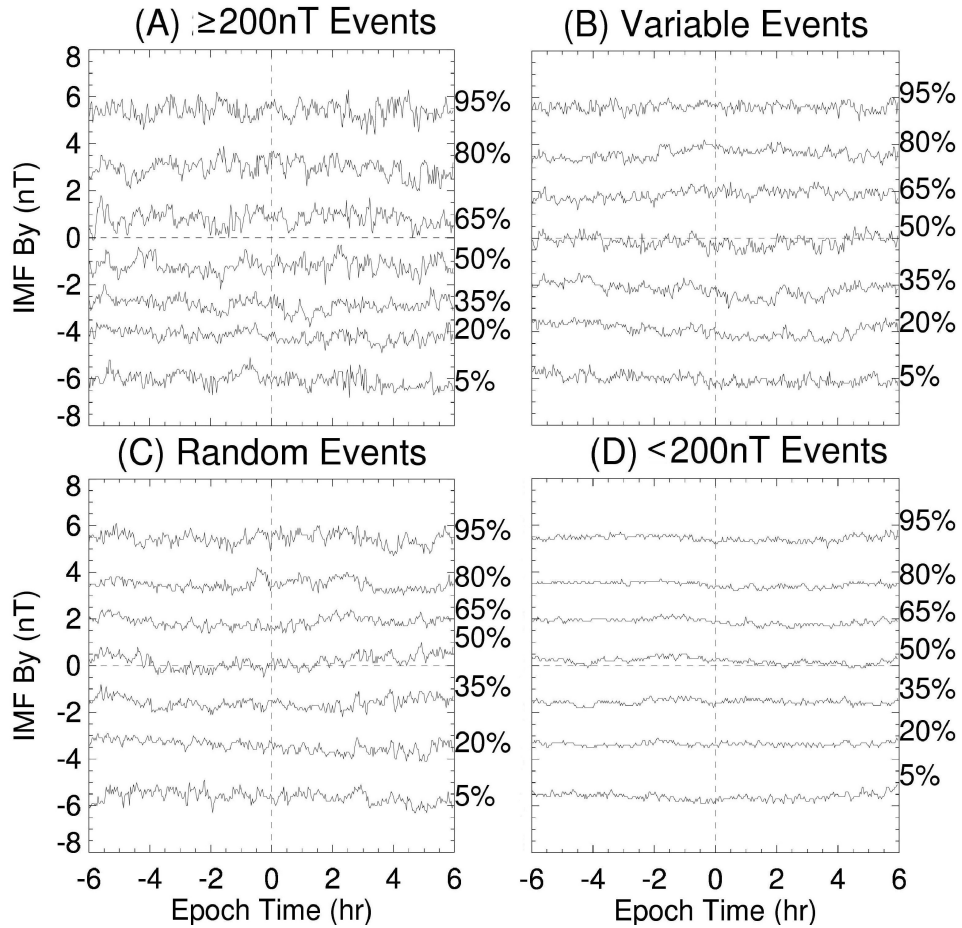


**Figure 6.2:** Cumulative distributions of IMF By as a function of superposed epoch time for (a)  $AE \geq 200$  nT SMC events, (b) Variable-AE SMC events, (c) randomly selected events, (d) non-enhanced events with  $AE < 200$  nT.

The cumulative distributions in Figure 6.1 reveal that a moderately negative IMF Bz component plays a significant role in driving SMC in the magnetosphere.

Since strong IMF  $B_y$  can also drive convection when IMF  $B_z$  is weak, it would be wise to examine IMF  $B_y$  to determine if there is a preferred azimuthal component. In Figure 6.2 the cumulative distribution of the IMF  $B_y$  component is presented as a function of the epoch time. All four panels show roughly the same trend, the 50% line lies approximately at 0 nT, so the events are equally distributed between positive and negative IMF  $B_y$ . There is also no noticeable change in IMF  $B_y$  near the onset.

### 6.1.2 Convection Electric Field and Transpolar Voltage

Enhanced convection is one of the main requirements of SMC. The electric field in the magnetosphere, which is induced by the flow of the solar wind in the magnetosheath, maps down to the ionosphere where it can be measured by SuperDARN. When convection is enhanced the electric field induced in the ionosphere will be larger, and vice versa. It can be difficult however to use the electric field, as it is a vector quantity, which is why the SuperDARN PCPD is very often used as a proxy for the convection electric field.

The cumulative distributions of PCPD in Figure 6.3 are of the same form as those presented in Figure 6.1, including the events sets (A)  $AE \geq 200$  nT SMCs, (B) the variable-AE SMCs, (C) the randomly selected intervals, and (D) “non-enhanced”  $AE \leq 200$  nT events. Roughly two hours before the SMC onset epoch time panels (A) and (B) of Figure 6.3 show a marked increase in the PCPD. This two hour “growth phase” occurred at roughly the same epoch time as IMF  $B_z$  was dropping in Figure 6.1.

In panels (A) and (B) the 5% line displayed the largest increase in PCPD, and as one progresses to higher percentages of events in the cumulative distributions the voltage increase becomes less prominent. The one exception in both panels was the 95% line. It displayed a greater increase than the 80% line. This could be because the 95% line represents the upper fringe of the data set, where the most erratic events exist. The general trend in the other percentage lines is clear: when the voltage is initially large it stays large after onset, and when it is low beforehand it becomes

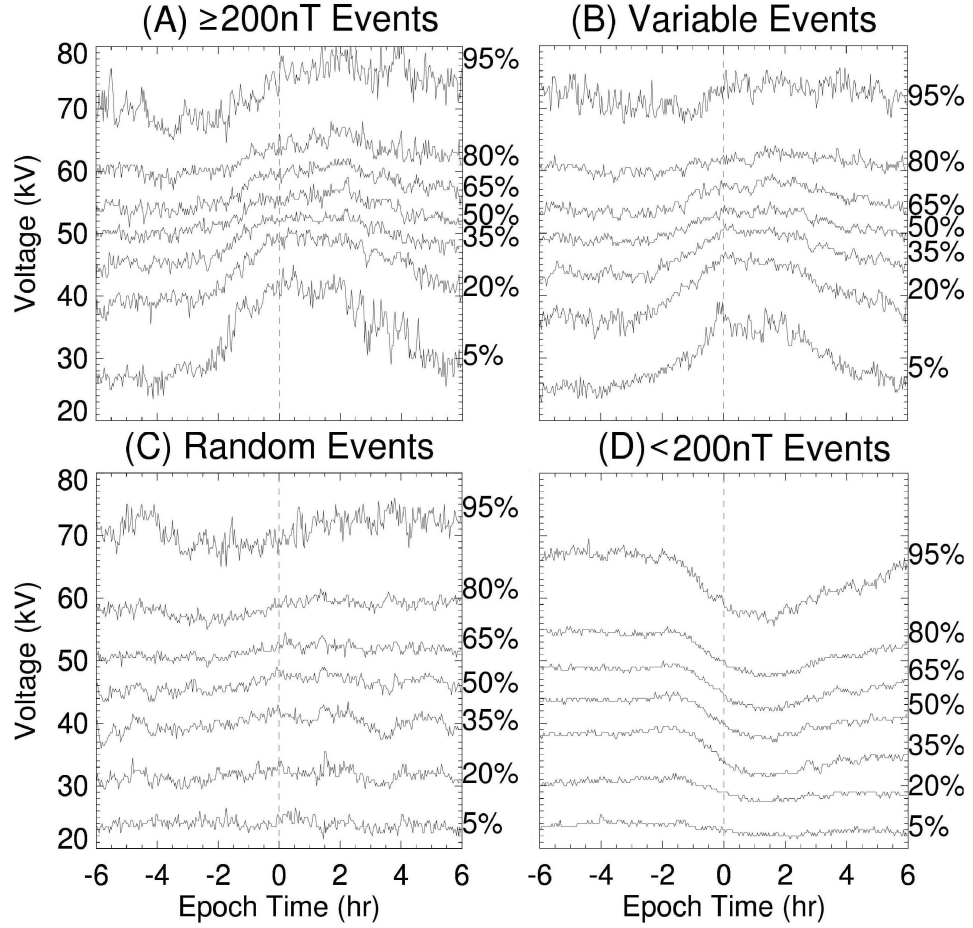


**Figure 6.3:** Cumulative distributions of PCPD as a function of superposed epoch time for (a)  $AE \geq 200$  nT SMC events, (b) Variable-AE SMC events, (c) randomly selected events, (d) non-enhanced events with  $AE < 200$  nT.

large after onset. The two hour ramp-up before onset of SMCs is interesting. *Sergeev et al.* (1995) stated that all SMC events they observed were preceded by a substorm. The 2 hours before onset could be the time frame for the substorm. It may take two hours for the magnetosphere to reconfigure itself before entering a phase of enhanced and steady convection.

The randomly selected events in panel (C) did not display any clear change near onset. The voltage was roughly constant before and after onset. The non-enhanced  $AE \leq 200$  nT events, once again, displayed the opposite trend as panels (A) and (B). Based on the superposed epoch analysis of SuperDARN PCPD, the SMC events selected using both methods exhibit enhanced PCPD. The events in panel (D) serve

to illustrate the suppression of PCPD for non-enhanced intervals.

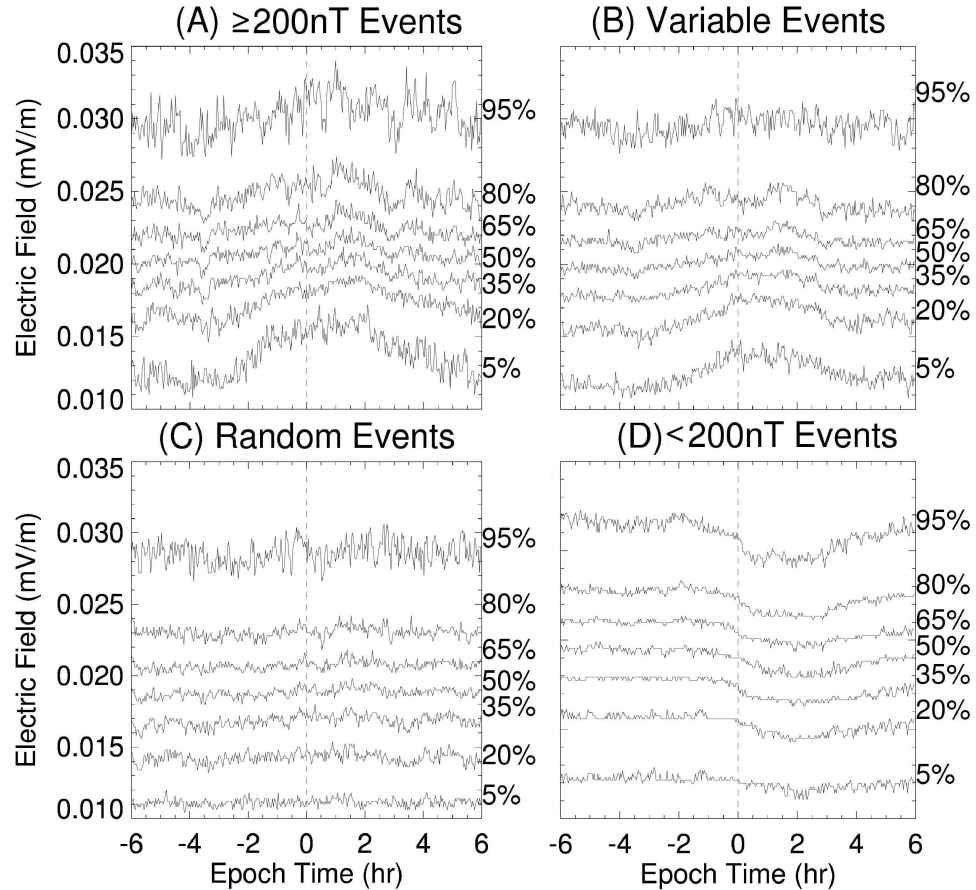


**Figure 6.4:** Cumulative distributions of the convection electric field as a function of superposed epoch time for (a)  $AE \geq 200$  nT SMC events, (b) Variable-AE SMC events, (c) randomly selected events, (d) non-enhanced events with  $AE < 200$  nT.

The cross polar cap potential difference depends on the electric field present and the size of the convection pattern. In other words, integrating a strong convection electric field along a short path between the voltage extrema can yield the same PCPD as a weak convection electric field integrated across a much larger convection pattern. To determine if the distance between voltage extrema affects the PCPD results, the average cross polar cap electric field was estimated. The cumulative distribution of the calculated cross polar cap electric field is presented as a function of epoch time in Figure 6.4.

The software tools that are used to analyse data from SuperDARN produce

voltage values in every grid cell of the convection pattern. The locations of the maximum and minimum voltage values can be determined. The arc length between these two points can then be calculated. The arc length between the two voltage extrema is calculated by first determining the angle at the Earth's centre between the two vectors that point toward the voltage extrema. This angle was found by computing the dot product between these two vectors. The spherical arc length subtended by the vectors is calculated at an altitude of 250 km, which corresponds to the F-region peak. This arc length is the geodesic distance between the two voltage extrema on a spherical surface at ionospheric heights. By dividing the PCPD by this arc length, one obtains a rough estimate of the average cross polar cap electric field for that particular SuperDARN convection map. There are some words of caution that are necessary before using these calculated electric field values.

The SuperDARN convection mapping software finds the position of the maximum and minimum voltage. These are not necessarily the centres of a well behaved two cell convection pattern. At times the convection patterns can become highly convoluted and complex. In the event that this occurs the average cross polar cap electric field may not be a true representation of the convection electric field in the ionosphere. To find the actual electric field a line integral calculation is required between voltage maxima perpendicular to the convection streamlines. However as a first step, this simple estimate can reveal if the convection electric field as well as the PCPD are enhanced during SMC, or if the polar cap is getting larger during SMC.

The  $AE \geq 200$  nT SMC events in Figure 6.4 (A) display an increase in the polar cap electric field, indicating convection becomes enhanced before SMC onset. At the 3 hour epoch time the average electric field values began to decrease back to pre-SMC levels. The variable AE cumulative distribution in panel (B) of Figure 6.4 displayed a similar but much weaker trend. When the electric field value was low before onset it became large afterwards; when it was large before onset it stayed large. The trend, which is similar to that of PCPD, was less pronounced for panel (B). This was expected because using a constant AE cutoff function will only identify the events with the strongest convection in the winter months. The relative increase leading up

to onset was less pronounced for the electric field, compared with the PCPD. This suggests that the distance between voltage centres maybe increasing before SMC.

The random events of panel (C) show no increase in electric field before or at onset, and the  $AE \leq 200$  nT events display a decrease in polar cap electric field at onset, in contrast to panels (A) and (B). Based on the average electric field superposed epoch analysis, SMC intervals selected by both methods have enhanced convection, but it is apparent that the distance between voltage extrema is having an effect on the PCPD.

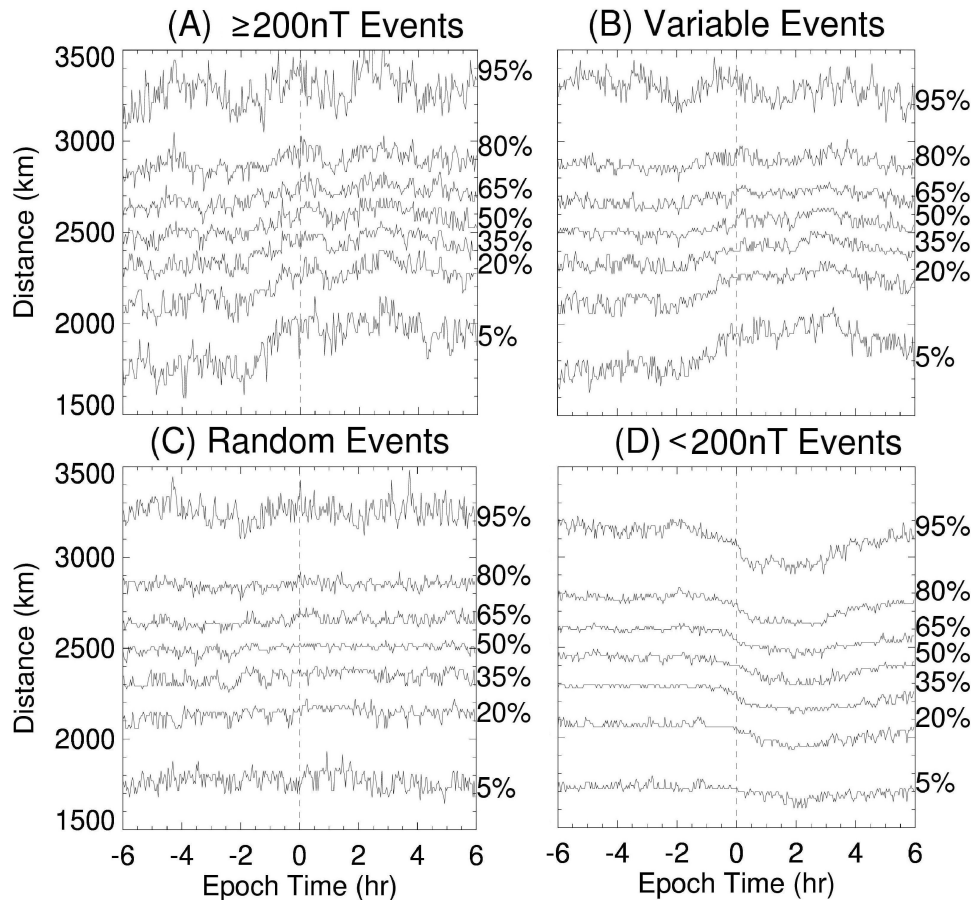


**Figure 6.5:** Cumulative distributions of the distance between voltage extrema as a function of superposed epoch time for (a)  $AE \geq 200$  nT SMC events, (b) Variable-AE SMC events, (c) randomly selected events, (d) non-enhanced events with  $AE < 200$  nT.

The cumulative distributions of the distance between voltage extrema is presented in Figure 6.5. In panels (A) and (B) SMC events selected using a constant

AE cutoff function and using Equation 5.2 are shown, respectively. In both panels (A) and (B) all percentage lines show a small increase in distance roughly 2 hours before onset but after onset the distance stays relatively constant. The increase in distance became less prominent with increasing percentage with one exception, the 95 % line showed large fluctuation. As before, this is likely due to statistical outliers. The encouraging aspect of panels (A) and (B) is that the distance remains stable after onset. During the course of SMC events the PCPD is, therefore, on average, an appropriate proxy for convection. The increase in distance prior to onset corresponds well with IMF Bz turning southward, and it could be an indication that it takes time for the magnetosphere to adjust to a stable convection state. The polar cap may need to increase in size until equilibrium between the reconnection rates on the day and night side are reached. Based on Figure 6.5, Figure 6.3, and Figure 6.4 it can also be concluded that the PCPD does contain information regarding convection and is a useful proxy for convection during SMC.

### 6.1.3 SuperDARN Data Coverage

During very active times in the magnetosphere, such as substorms, the energetic auroral particle precipitation can greatly increase the electron density in the ionosphere. In regions of bright aurora the amount of data SuperDARN obtains is often greatly diminished (*Gauld et al.*, 2002). During these scientifically interesting dynamic times in the magnetosphere SuperDARN often loses its view of convection. Whether this happens during active but steady times such as SMC has not yet been investigated. In Figure 6.6 the cumulative distributions of the number of SuperDARN data points are presented in the same format as the previous cumulative distributions.

In panels (A) and (B) the number of data points gradually increases before onset for all percentage lines. As before, panels (A) and (B) were made using SMC events selected using the constant AE cutoff function and the variable AE cutoff function, respectively. In panels (A) and (B) the number of SuperDARN convection points begin to increase roughly 4 hours before onset. By 6 hours after onset

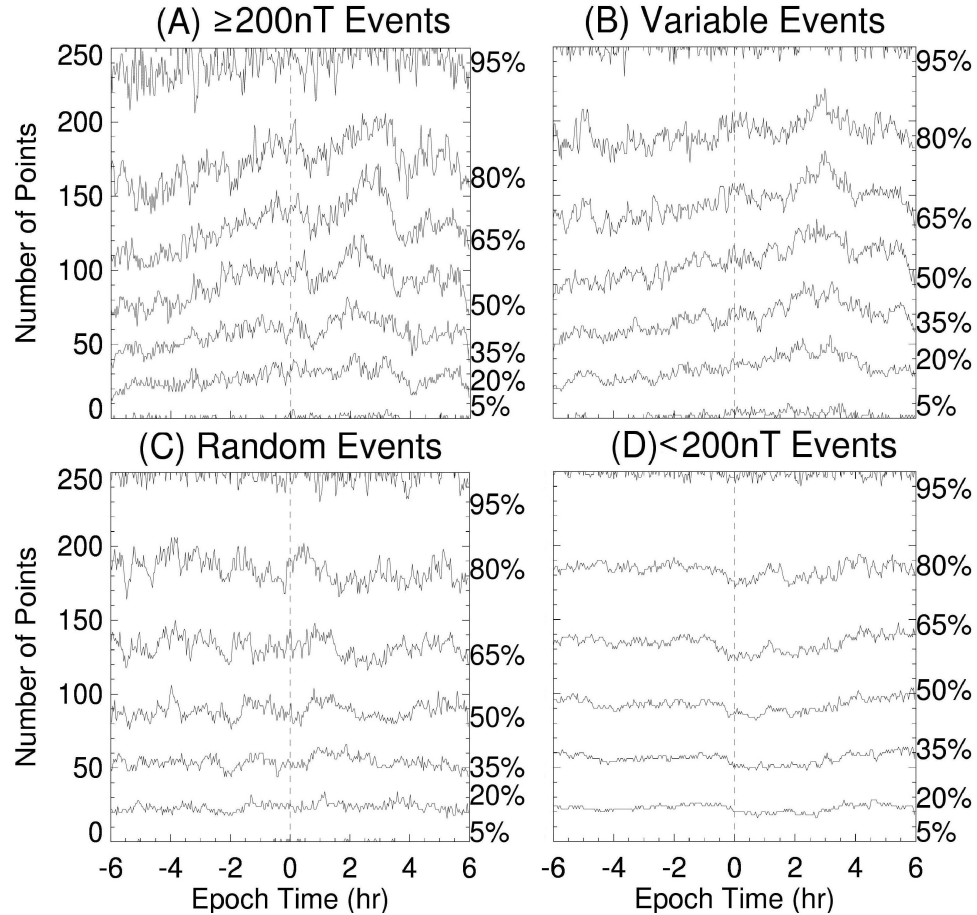


**Figure 6.6:** Cumulative distributions of the SuperDARN data points as a function of superposed epoch time for (a)  $AE \geq 200$  nT SMC events, (b) Variable-AE SMC events, (c) randomly selected events, (d) non-enhanced events with  $AE < 200$  nT.

the number of data points had decreased back to pre-SMC levels. The number of data points was roughly constant for the randomly selected events in panel (C). The number of data points decreased slightly for the non-enhanced events in panel (D). Figure 6.6 indicates studying convection during SMC with SuperDARN is appropriate as, statistically, there is no reduction in data volume associated with SMC.

## 6.2 Scatter Plot Study of Association Between SMC Parameters

The superposed epoch analysis of the previous section revealed characteristics of the time evolution of SMC in a statistical manner over a 12 hour interval centred on SMC onset. This analysis, however, did not include any information regarding the average conditions during the various types of events that were compared. It would be useful to study conditions, in particular the SuperDARN convection data, during the SMC events and compare these with the other measured parameters, as well as previous SMC studies of average conditions during SMC. To that end, statistical scatter plots were produced. Scatter plots allow one to determine if two different parameters are related, but it is important to remember that the causal links can not be verified with this type of analysis.

### 6.2.1 IMF Conditions

This discussion will begin with the upstream IMF conditions that drive convection in the magnetosphere. An average IMF Bz and an average IMF By value was calculated for each interval in the events sets measured during the years 1998 - 2001. The IMF Bz value was then plotted as a function of IMF By to produce the scatter plots in Figure 6.7.

Panel (A) of Figure 6.7 corresponds to the events that were selected with a constant minimum AE value of 200 nT. The median IMF Bz value for these events is moderately negative at -2.7 nT. This is an expected result and is in agreement with past SMC studies such as *O'Brien et al. (2002)* and *DeJong and Clauer (2005)*. Panel (B) was created using the variable-AE SMC events selected using Equation 5.2. The median IMF Bz value was roughly -1.8 nT, which was less than for the events selected using a constant AE cutoff function of 200 nT, but was also moderately negative. One would expect that the average IMF Bz would be slightly less negative during the variable AE SMC events because, as previously discussed, a constant AE

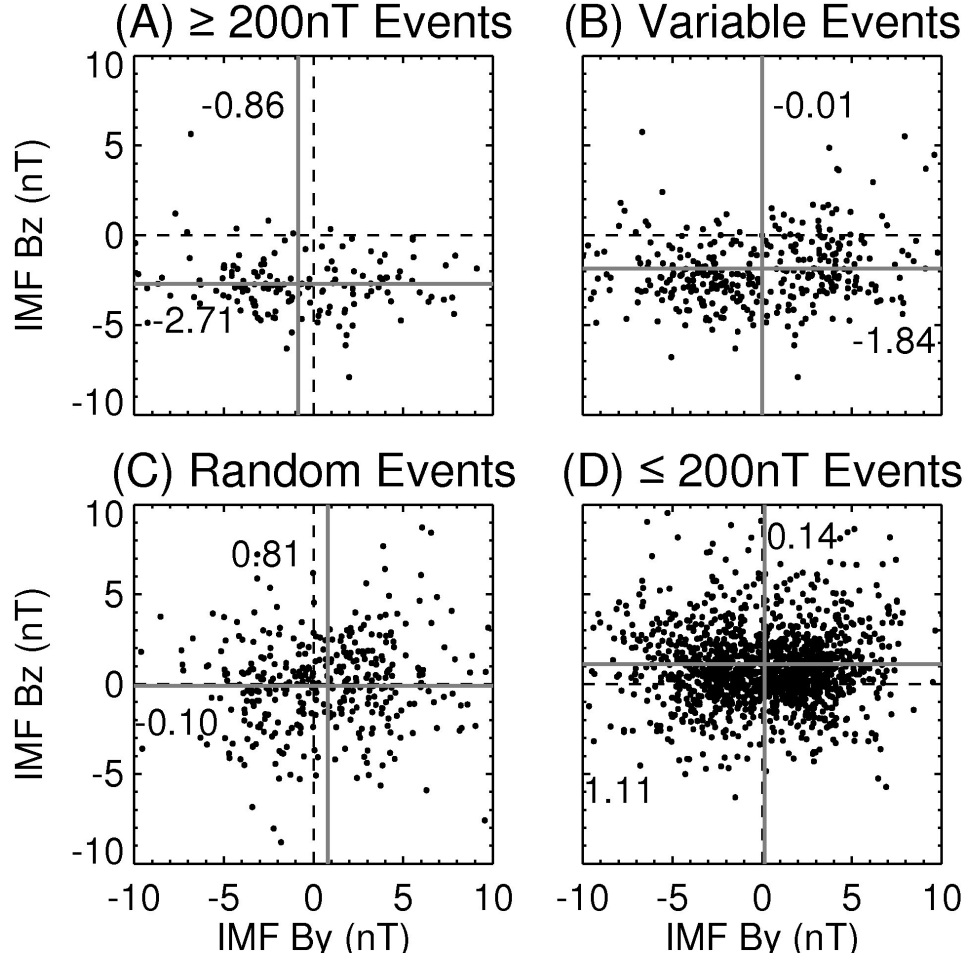


**Figure 6.7:** Scatter plots of IMF  $B_y$  versus IMF  $B_z$  for: (a) AE  $\geq 200$  nT SMC events, (b) Variable-AE SMC events, (c) randomly selected events, and (d) non-enhanced events with AE  $\leq 200$  nT. The grey lines in each panel indicate the median values.

cutoff function will favour only the strongest events in the winter months. On the other hand, the variable AE events will include those that have weaker convection and therefore, presumably, a weaker driver, which is supported by the slightly smaller driven IMF  $B_z$  median values. The IMF  $B_y$  values for both SMC event sets were more evenly distributed around 0 nT. The variable AE SMC events of panel (B) had many more events with large IMF  $B_y$  magnitudes. This indicates that the weaker winter SMC events that are added when the AE threshold is lowered occur when the upstream IMF is strongly tilted from the southward. The dominant IMF  $B_y$  component may therefore have had an important role in driving convection in the

magnetosphere during these weaker SMC events.

In the scatter plot for the randomly selected events, which is panel (C) of Figure 6.7, the IMF Bz values were centred around 0 nT, while IMF By values were centred near 1 nT. The scatter of the data points suggests that there is no preferred IMF orientation during the randomly selected intervals. The non-enhanced events of panel (D) had a positive IMF Bz median value of 1.1 nT and an IMF By component median value near 0 nT. The scatter plots therefore confirm the superposed epoch analysis results, as well as previous work, that SMC are a phenomenon that occur under moderately negative IMF conditions and with a significant IMF By component.

### 6.2.2 Polar Cap Voltage and Electric Field Values

In this convection driven system it is of interest to determine how the SuperDARN PCPD relates to the IMF Bz component. Figure 6.8 displays the scatter plot of IMF Bz verses SuperDARN PCPD. In general, when IMF Bz is strongly negative a large convection electric field is expected and since PCPD has been shown to be a good proxy for convection during SMC, large values of PCPD are also expected. This trend will manifest itself in a scatter plot of IMF Bz verses PCPD with data points clustered around a line of negative slope. This is true for all four scatter plots in Figure 6.8. Panel (A), which consist of events selected using the constant AE cutoff function, have the largest median voltage at 57 kV and the most negative median IMF Bz component at -2.7 nT. Panel (B), which consists of events selected using the variable AE cutoff function in Equation 5.1, have a median PCPD of 54 kV and a median IMF Bz of -1.8 nT. The randomly selected events in panel (C) have a median voltage of roughly 45 kV and a median IMF Bz component of 0 nT. The non-enhanced events of panel (D) had a small median PCPD of 45kV and occurred under predominantly positive IMF Bz conditions. SMC is therefore a phenomenon that is driven by a moderately negative IMF Bz and has higher PCPD values than typical and non-enhanced intervals.

Since the PCPD is dependent on both the convection electric field and the path between voltage centres, it would be useful to investigate the relationship between

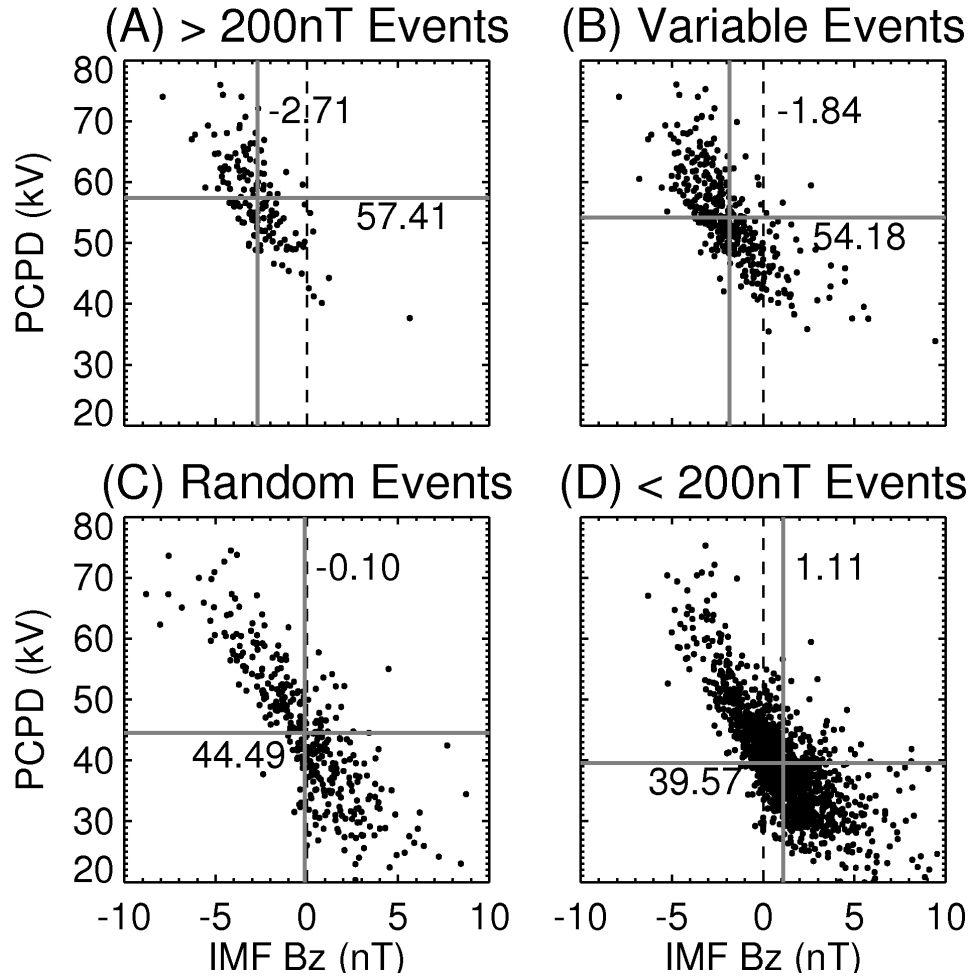


**Figure 6.8:** Scatter plots of PCPD versus IMF Bz for: (a) AE  $\geq 200$  nT SMC events, (b) Variable-AE SMC events, (c) randomly selected events, and (d) non-enhanced events with AE  $\leq 200$  nT. The grey lines in each panel indicate the median values.

these two properties. In Figure 6.9 the PCPD is plotted as a function of the distance between voltage centres. The median distance between voltage centres was larger for the SMC events in panel (A) and (B), compared to the randomly selected events in panel (C) and the non-enhanced events in panel (D). The median voltage was also larger for SMC events. The larger median values for both properties during SMC is not unexpected however, since the superposed epoch analysis has shown that both increased roughly 2 hours before onset. It is interesting to note that, while the SMC events may be a higher PCPD subset of the “typical” events in panel (C), the SMC events do not display a clear dependence on the distance between voltage extrema.

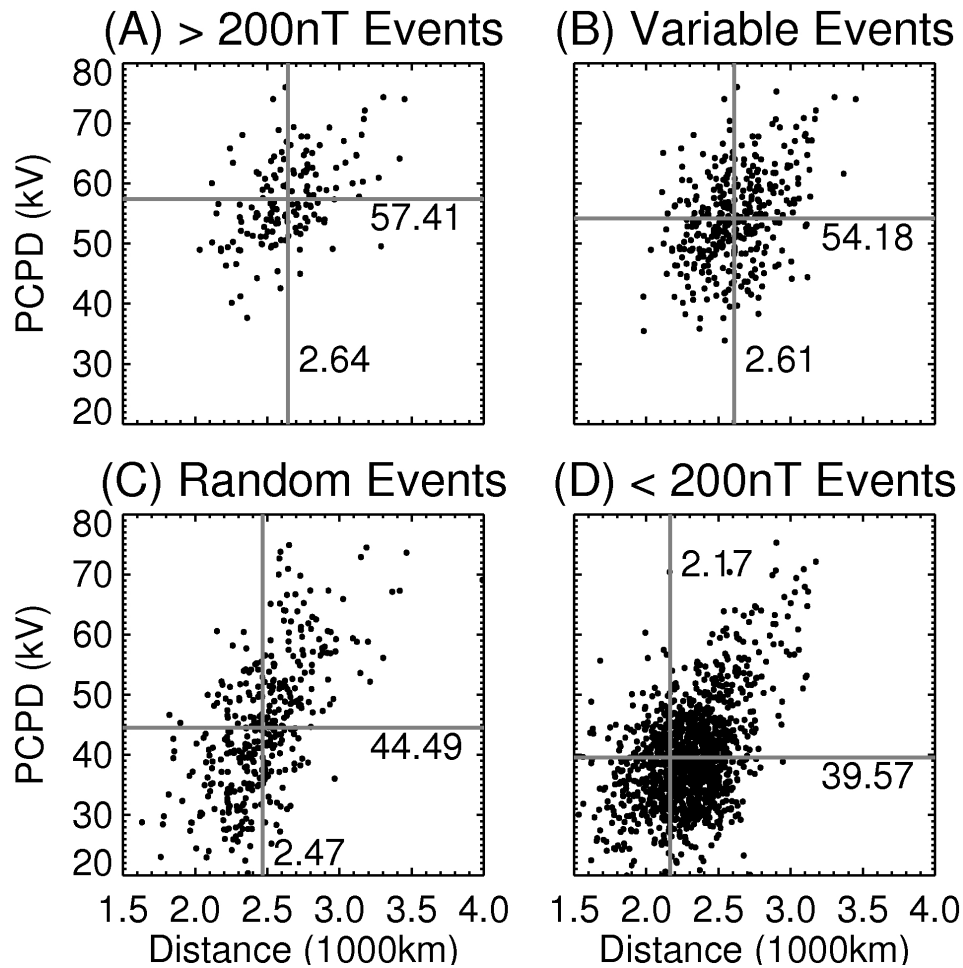


**Figure 6.9:** Scatter plots of PCPD versus distance between voltage extrema for: (a)  $AE \geq 200$  nT SMC events, (b) Variable-AE SMC events, (c) randomly selected events, and (d) non-enhanced events with  $AE \leq 200$  nT. The grey lines in each panel indicate the median values.

For SMC events it is not clear whether there is a relationship between polar cap size and PCPD. Recall that in Section 6.1.2 the superposed epoch study of distance between voltage extrema revealed that the distance was unchanging during SMC. It may be possible that the unchanging polar cap area expected during SMC could effectively decouple PCPD and the distance between the voltage extrema, but this will require much more detailed investigation.

Figure 6.10 contains the scatter plot comparison of the convection electric field and IMF  $B_z$ . When IMF  $B_z$  is strongly negative the convection electric field is also strong, resulting in a cluster of data points about a line with negative slope in all four

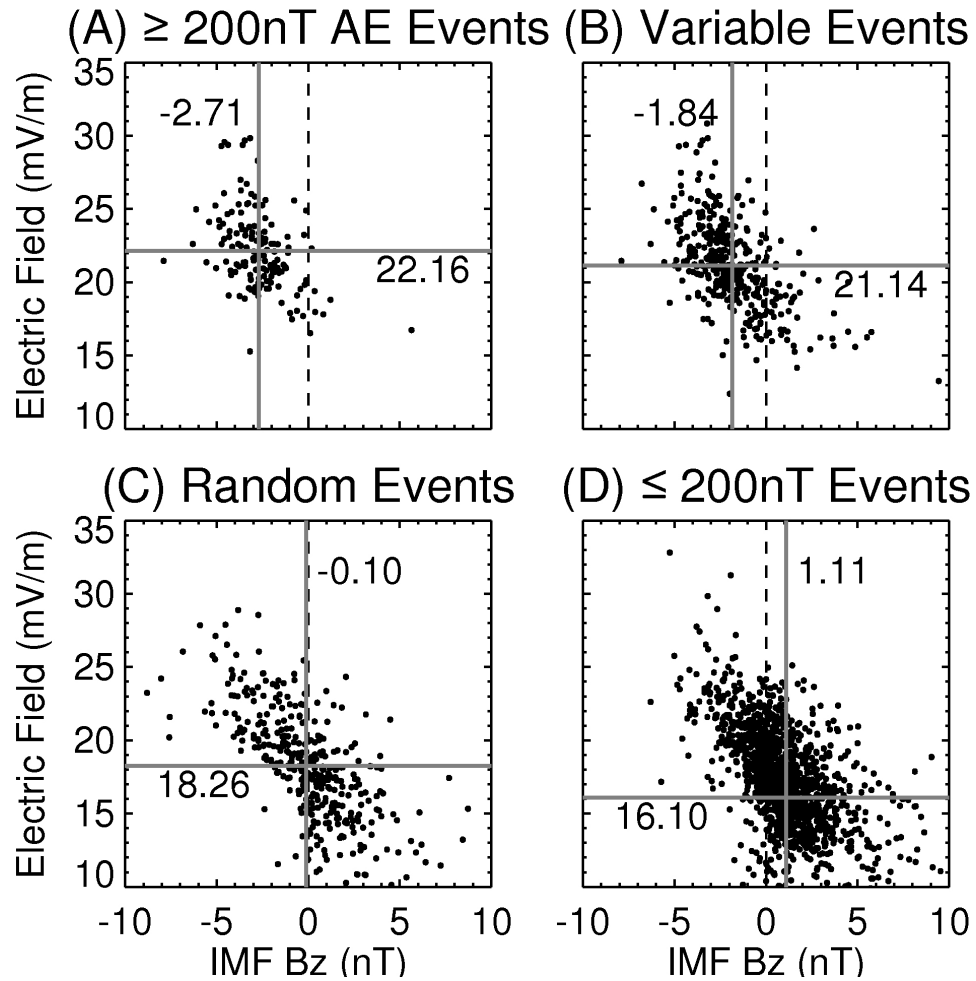


**Figure 6.10:** Scatter plots of convection electric field versus IMF Bz for: (a)  $AE \geq 200$  nT SMC events, (b) Variable-AE SMC events, (c) randomly selected events, and (d) non-enhanced events with  $AE \leq 200$  nT. The grey lines in each panel indicate the median values.

sets of events. This is indicative of IMF Bz driving convection in the magnetosphere when it is southward and expected. The events selected using the constant AE cutoff function had a median electric field value of 22 mV/m. The events selected using the variable AE cutoff had a median electric field value of 21 mV/m. The randomly selected events had an median voltage of 18 mV/m while the  $AE \leq 200$  nT events had a median voltage of 16 mV/m. Consistent with previous results, SMC is a phenomenon with a strong convection electric field.

## 6.3 Statistical Study Summary

These statistical studies revealed many interesting properties of SMC, as well as the relationships between them. A moderately negative IMF Bz drives SMC in the magnetosphere, with IMF Bz dropping roughly 2 hours before onset of most SMC events. The IMF Bz component rose to pre-SMC values 4 to 6 hours after onset. Furthermore, there was no preference in direction of IMF By for SMCs. It is also interesting to note that, in contrast, the  $AE \leq 200$  nT “non-enhanced” but steady events experienced an increase in IMF Bz leading up to onset.

The PCPD and the convection electric field both were large during SMC. Like the IMF components they increased roughly two hours prior to SMC onset. When convection was strong before onset it stayed strong, and when convection was weaker before onset it increased much more in a relative sense.

Investigation of the relationship between PCPD and polar cap size revealed that the distance between voltage centres was larger during SMCs than during non-SMC times. Both statistical analysis methods indicate that the PCPD is an appropriate proxy for convection. The relatively steady polar cap area during SMC results in changes in the convection electric field being reflected in changes in PCPD. More detailed investigation is required to determine the relationship between the polar cap area and the PCPD.

# CHAPTER 7

## SMC CASE STUDY

The improved variable AE selection criterion described in Chapter 5 was developed to identify SMC events with convection levels above a minimum convection threshold. Statistical studies of SuperDARN PCPD values and convection electric field estimates in Chapter 6, as well as the conceptual model in section 5.5, provided evidence supporting the hypothesis that the new enhanced convection criterion was performing well. The new criterion continued to identify enhanced events, with the conductivity effects on SMC selection greatly reduced. While the statistical methods are extremely useful in identifying the general properties of SMC, they can not reveal details of a particular SMC interval. To that end two SMC events will be discussed in detail.

The first SMC event, which occurred on October 20, 2001, was identified by both the modified method of *O'Brien et al.* (2002) and the variable AE cutoff function. The second SMC interval, which occurred on October 30, 2001, had AE values well below the 200 nT threshold of the modified selection criteria of *O'Brien et al.* (2002), so this event would not have been considered SMC according to traditional selection methods. This interval, however, did satisfy the new variable AE selection criterion. The AE threshold on this day was 93 nT, as per Equation 5.2.

The primary motivation of presenting these two case studies is to establish whether the extra events identified by the significantly lower AE threshold are similar to the SMC events selected using previously established methods. These two SMC intervals in particular were selected because they occurred at roughly the same time of year, and they both had optical observations of the entire northern auroral oval for the duration of the SMC events.

SMC has been suggested as a special type of convection in the magnetosphere (*Pytte et al.*, 1978, and *Sergeev et al.*, 1995). In order to compare with another enhanced convection mode in the magnetosphere a case study of a sawtooth event is also presented. The sawtooth event occurred on October 21, 2001. The sawtooth case study will highlight, using a data presentation identical to that of the SMC case studies, the properties of solar wind-magnetosphere coupling during strongly driven but not steady conditions. This particular sawtooth event was selected because it occurred at the same time of year as the two SMC intervals, and it had good optical auroral coverage.

## 7.1 SMC Case Study 1: October 20, 2001

The first SMC event occurred on October 20, 2001. The AE and AL indices for the entire day are presented in Figure 7.1. This SMC was selected using the traditional  $AE \geq 200$  nT enhanced convection criterion. Because the variable AE cutoff is lower than 200 nT in the winter months, this SMC is also identified using the new modified AE criterion. On this day the variable AE enhanced convection threshold is 94 nT. On this day the AE index ranged from 100 nT to more than 500 nT. This large range of values is due to the occurrence of several substorms on this day. During the SMC event (indicated by vertical lines in Figure 7.1) the AE index decreased from near 500 nT to about 200 nT.

Both selection methods identified the same start and end times (14:26 UT and 17:41 UT). This indicates that the steadiness criterion ( $dAL/dt \leq -25$  nT/min) determined the duration of this event, as this requirement is the same for both selection methods. Examination of the AL index reveals several vary rapid decreases, indicative of substorms. The first AL substorm signature occurred just after 5 UT, the second near 10 UT, and the third immediately preceded onset of the SMC event (14:26 UT). It was the substorm signature preceding the SMC that violated the steadiness criterion, but there is no similar signature at the end of the SMC indicating unsteady convection afterward. The derivative of AL with respect to time

was carefully examined to determine when and for how long convection was unsteady after the SMC.

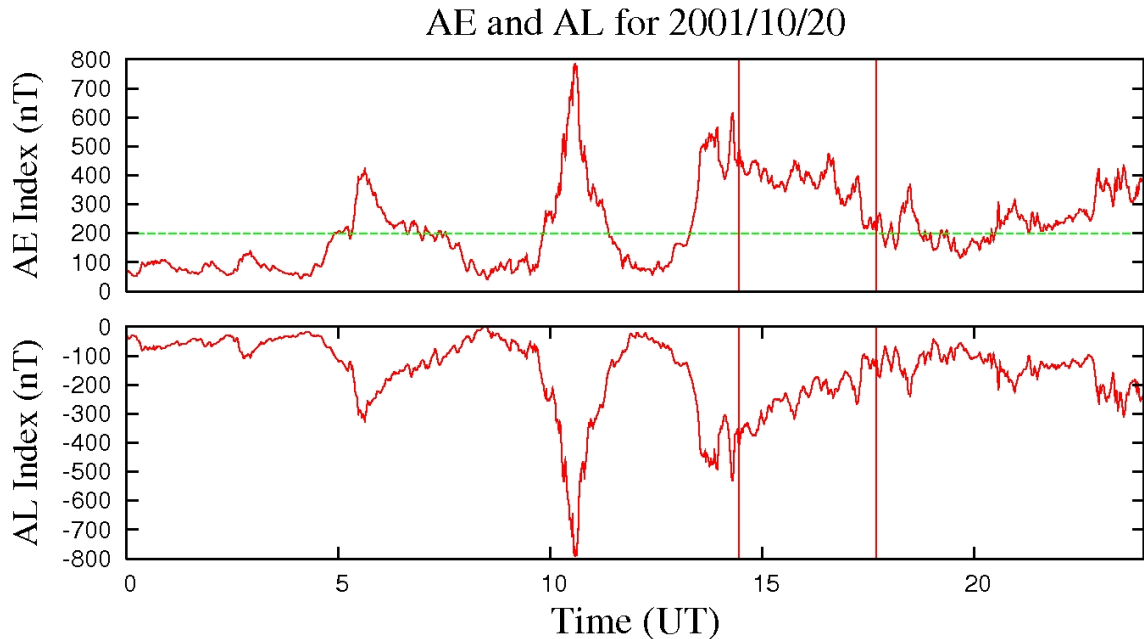


**Figure 7.1:** From top to bottom: (1) the AE index and (2) the AL index for October 20, 2001. The start and end of the SMC Event 1 is marked by vertical lines.

The steadiness criterion,  $dAL/dt \geq -25$  nT/min, was violated when  $dAL/dt = -29$  nT/min at 17:42 UT. The steadiness criterion was only violated at this one data point, after which the AL remained steady until 18:14 UT. The AE index dropped below 200 nT at 17:50 UT, so the modified criteria of *O'Brien et al.* (2002) would have deemed this event ended at 17:50 UT had it not been for that one AL data point. For convection to be considered enhanced according to the new variable-AE threshold of Equation 5.2, the AE index must be above 94 nT. If that single data point had not violated the steadiness requirement, the variable selection method would have ended the event at 18:14 UT. More work is required to develop a more robust method for quantifying steady convection using the AL index. Methods are currently being tested that scale the -25 nT/min threshold according to the AE index (T. Pulkkinen, personal communication) and allow a small percentage of data points to violate the steadiness criterion (R. L. McPherron, personal communication).

The Wideband Imaging Camera (WIC), which is part of the Far Ultra Violet

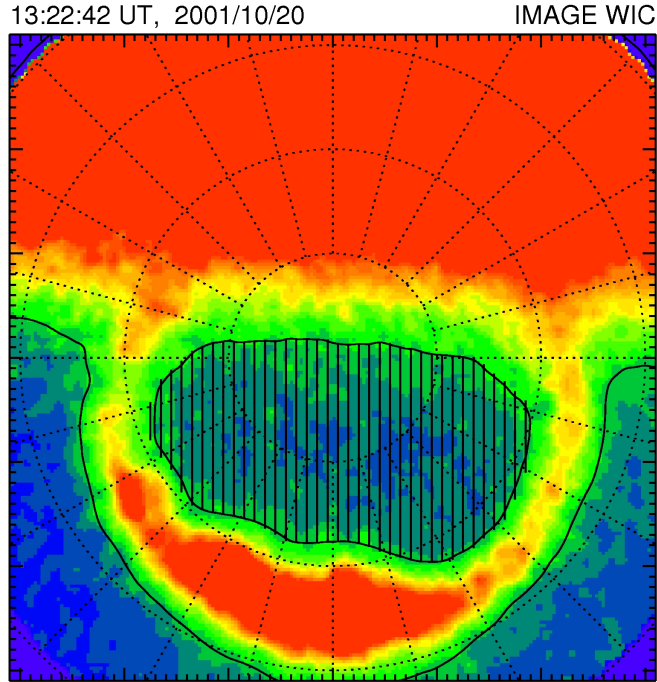


**Figure 7.2:** Auroral image obtained from the IMAGE satellite by WIC with the shaded region indicating the estimated polar cap area as determined through piece-wise integration. The image is projected on a magnetic latitude, magnetic local time grid, where the dashed circles represent 10 degree increments in magnetic latitude, and the straight dashed lines represent hours of MLT, with magnetic local noon towards the top of the figure.

(FUV) instrument package, aboard the IMAGE satellite recorded images of the entire northern auroral oval during this SMC event (*Mende et al.*, 2000a, *Mende et al.*, 2000b). A sample image recorded by the WIC is presented in Figure 7.2. The start time of this image is 15:42:54 UT, and the exposure time of each image is 10 seconds. The WIC camera records ultraviolet light emissions from the atmosphere in the UV wavelength band from 140 - 180 nm. This sample image is presented in units of raw counts. The absolute calibration of the image is not important for this study, but rather it is the general morphology of the aurora and the relative changes in the pattern. The image is projected on a magnetic latitude, magnetic local time grid, where the dashed circles represent 10 degree increments in magnetic latitude, and the straight dashed lines represent hours of MLT, with magnetic local noon towards the top of the figure.

The auroral oval is the red and yellow coloured ring of bright aurora between 60 and 70° magnetic latitude. The bright emission that fills the top of the figure is the ultraviolet dayglow caused by sunlight. The dayglow can make calculations of the absolute size of the polar cap very difficult, but this study requires only relative areas, so the dayglow contamination of the image is not a significant problem in this case.

From the sequence of images it is possible to obtain an estimate of the polar cap size and its variations during the SMC event. These results will be compared with the work of *DeJong and Clauer (2005)*. Figure 7.3 is a summary of all WIC images that were recorded between 12 and 20 UT on October 20, 2001. The bottom two panels are composed of slices extracted from all the WIC images. This type of data presentation is referred to as a keogram. Figure 7.3 contains the luminosity measurements within 10 km of 6 and 18 MLT, effectively a horizontal slice through the middle of Figure 7.2. Figure 7.3 contains the luminosity measurements within 10 km of 12 and 24 MLT, effectively a vertical slice through the middle of Figure 7.2.

The work of *DeJong and Clauer (2005)* relied on the assumption that when convection is steady the area of the polar cap is unchanging. *DeJong and Clauer (2005)* defined steady polar cap area numerically as changing less than 10% per hour. Unfortunately, their description of the area calculation process is rather vague. Because of this ambiguity it is not possible to determine if the SMCs in the present study possess steady convection according to the criterion of *DeJong and Clauer (2005)*.

The polar cap area boundary was defined as the contours equatorward of which the luminosity fell below a maximum threshold defined by the user. This contour was determined from an image that was smoothed using a two dimensional boxcar filter of order 12. The maximum threshold was not the same for all events, as the background brightness in the polar cap could be quite different for different events. For SMC Event 1 a value of 550 raw counts for the WIC was used. With the perimeter of the auroral oval in place, the area was estimated through piece-wise integration. The polar cap boundary was projected onto a flat two-dimensional

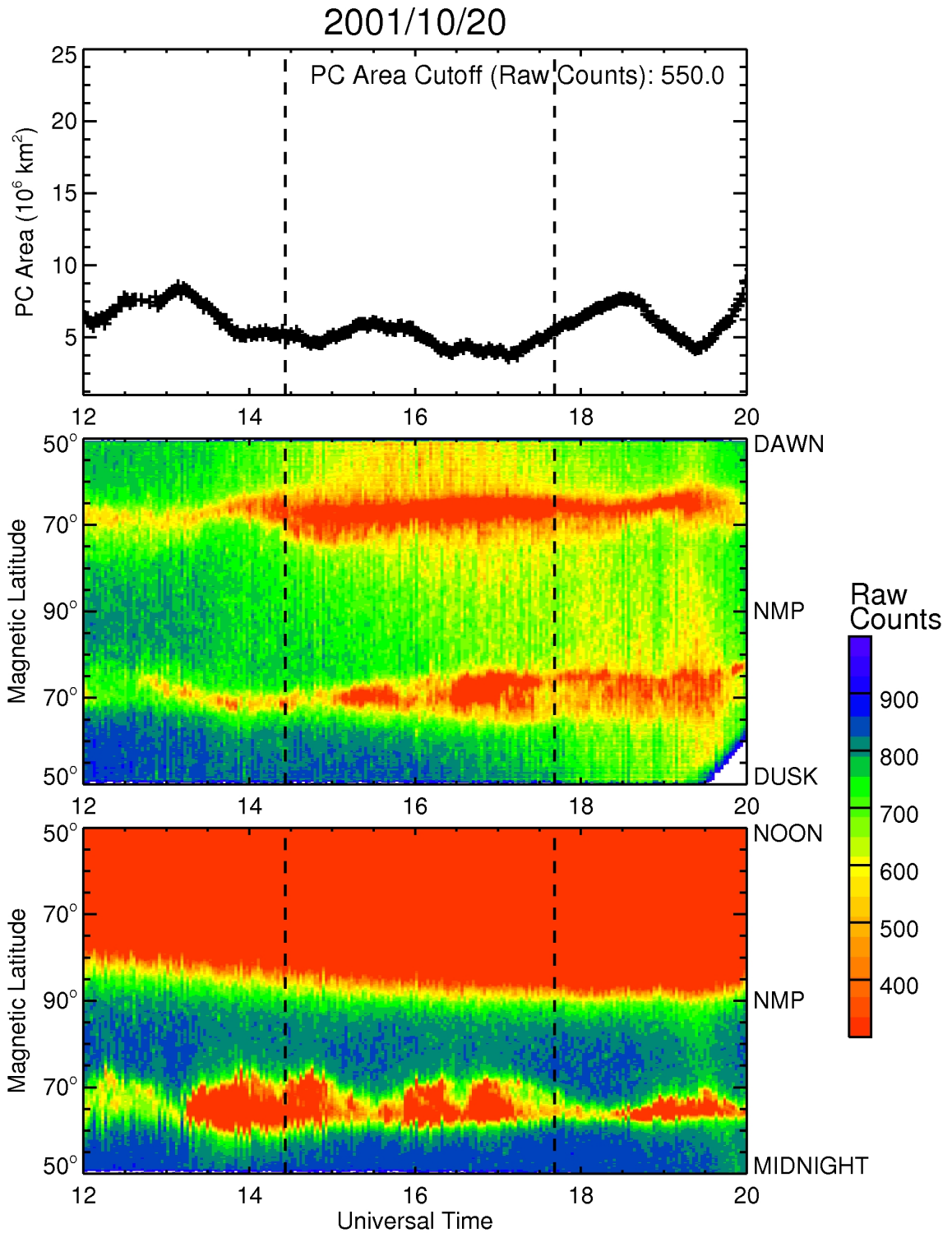


**Figure 7.3:** From top to bottom: (1) the polar cap area, (2) the keogram from dawn to dusk, and (3) the keogram from noon to midnight on October 20, 2001. The start and end of SMC Event 1 is denoted by the vertical dashed lines.

coordinate system centred on the magnetic pole, with the  $x$  axis pointing from dusk to dawn in MLT and the  $y$  axis pointing from midnight to noon in MLT. A two dimensional projection of the spherical solid angle was deemed sufficient for the purposes of this thesis, since the primary objective is to investigate the change in polar cap area. The piecewise integration progressed in steps of 111 km ( $1^\circ$  latitude) in the  $x$  direction. For each incremental vertical stripe, the polar cap area was determined by integrating from the maximum  $y$  value to the minimum  $y$  value. The total polar cap area for each auroral image is the sum of the areas of the incremental vertical slices. A graphical example of the area calculation is displayed in Figure 7.2. The solid closed contour represents the polar cap, and the vertical lines represent the starting point of successive integrations from left to right.

Over the course of SMC Event 1 the average polar cap area was found to be  $4.9 \times 10^6$  km<sup>2</sup> with a standard deviation of  $0.7 \times 10^6$  km<sup>2</sup> (14% of the mean). In contrast, the average area for the whole day was  $5.9 \times 10^6$  km<sup>2</sup> with a standard deviation of  $1.8 \times 10^6$  km<sup>2</sup> (20% of the mean). The polar cap area was therefore much less variable during the SMC interval. A second approach was also used to quantify the steadiness of the polar cap area. The number of data points that fell within 10% of the hourly mean was determined for the duration of the SMC. Of the 96 polar cap area values during the interval 73% were within 10% of the hourly mean. Of the 173 polar cap area values on this day not included in the SMC interval, 53% fell within 10% of the hourly mean. Both polar cap area variability estimations indicate that the polar cap area was less variable during the identified SMC interval.

*Frey et al.* (2004) identified a substorm onset over Russia at 15:35 UT based on the same WIC images used to estimate the polar cap area. A substorm onset was identified when the following three criteria were met: (1) a clear local brightening of the aurora must occur, (2) the aurora had to expand to the poleward boundary of the auroral oval and expand azimuthally in local time for at least 20 minutes, and (3) the substorm onset was only selected as a separate event if at least 30 minutes had passed after the previous onset.

This identified substorm onset occurs in the middle of SMC Event 1 and con-

tradicts the notion that this interval is a time of steady convection as substorms represent times of unstable convection. There was no substorm signature in the AL index, but this may be due to poor magnetometer coverage in the vicinity of the substorm during the event. As well, there were no satellite measurements from the magnetotail available, so it is impossible to know if any large scale reconfiguration of the magnetotail occurred at the time of this event.

This situation illustrates why it can be dangerous to use ground based magnetometers to determine convection states in the magnetosphere and why a more robust definition of steady convection is required.

The solar wind conditions measured by the ACE satellite were used to provide insight into the role of the solar wind and the IMF during SMC Event 1. One of the primary functions of ACE is to measure the magnitude and direction of the IMF, using the Magnetic Field Instrument (MAG) (*Smith et al.*, 1998). The measurements made by this satellite must be time-shifted to account for the finite propagation time of the solar wind from ACE to Earth. The time shifted data are used as an input parameter for SuperDARN convection maps. As described in Section 4.12, the IMF data determine the statistical a priori convection model that is used to constrain the convection map fitting procedure.

The unshifted IMF data measured from 0 to 24 UT at ACE are presented in Figure 7.4. The data are in GSM coordinates. SMC Event 1 was characterised by a negative IMF Bz component (third panel) that oscillated between 0 and -5 nT. The IMF By component (second panel) was predominantly positive with a magnitude of about 5 nT, while the IMF Bx (top panel) component was near zero. The magnitude of the IMF (bottom panel) was very stable and near 8 nT during the SMC event.

The unshifted solar wind speed, pressure and density, as measured by the ACE Solar Wind Experiment (SWE) (*McComas et al.*, 1998), are pictured in Figure 7.5. The solar wind conditions over the course of SMC Event 1 were stable. The solar wind speed (bottom panel) was near or below 400 km/s and the proton density (top panel) was about  $4 \text{ cm}^{-3}$ .

The time delay between ACE and the magnetopause was estimated from the

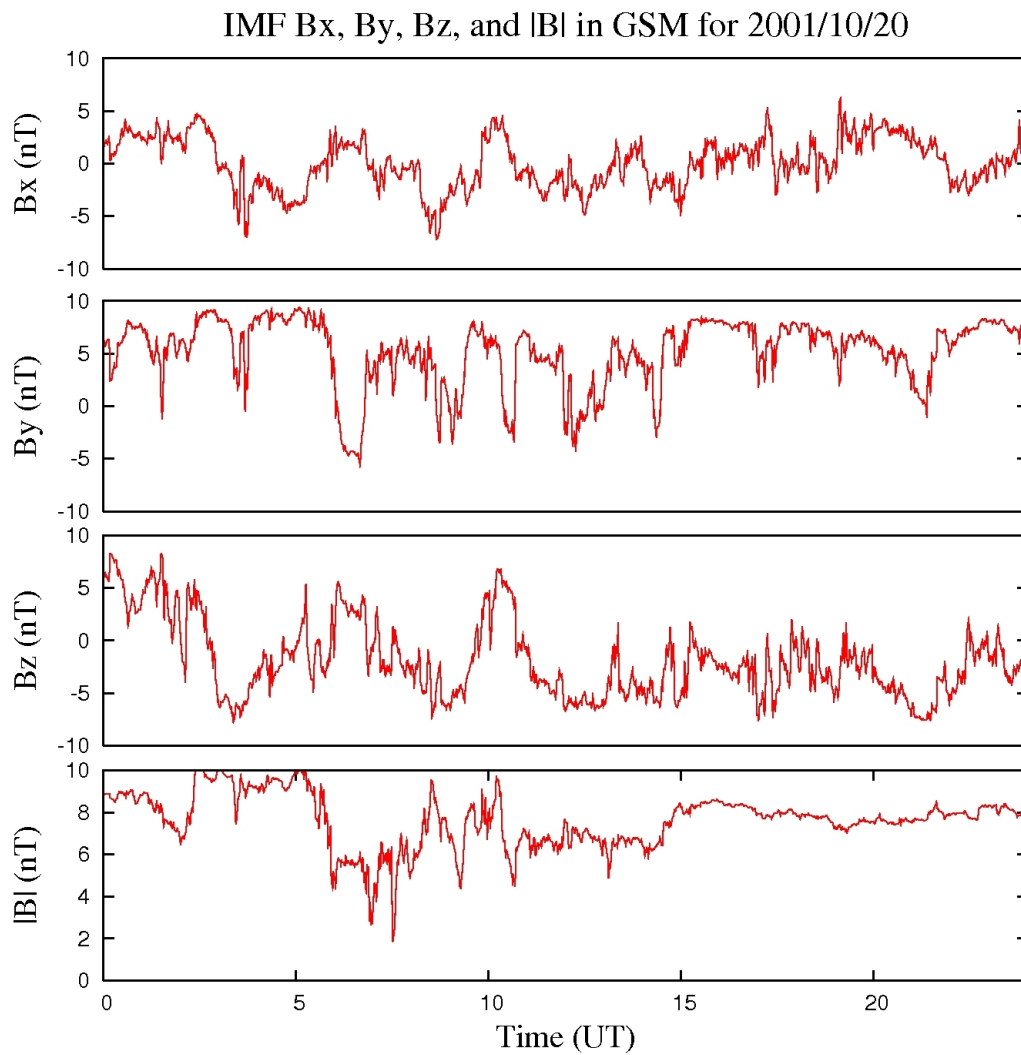


**Figure 7.4:** From top to bottom: (1) IMF Bx, (2) IMF By, (3) IMF Bz and, (4) IMF magnitude in GSM coordinates for October 20, 2001.

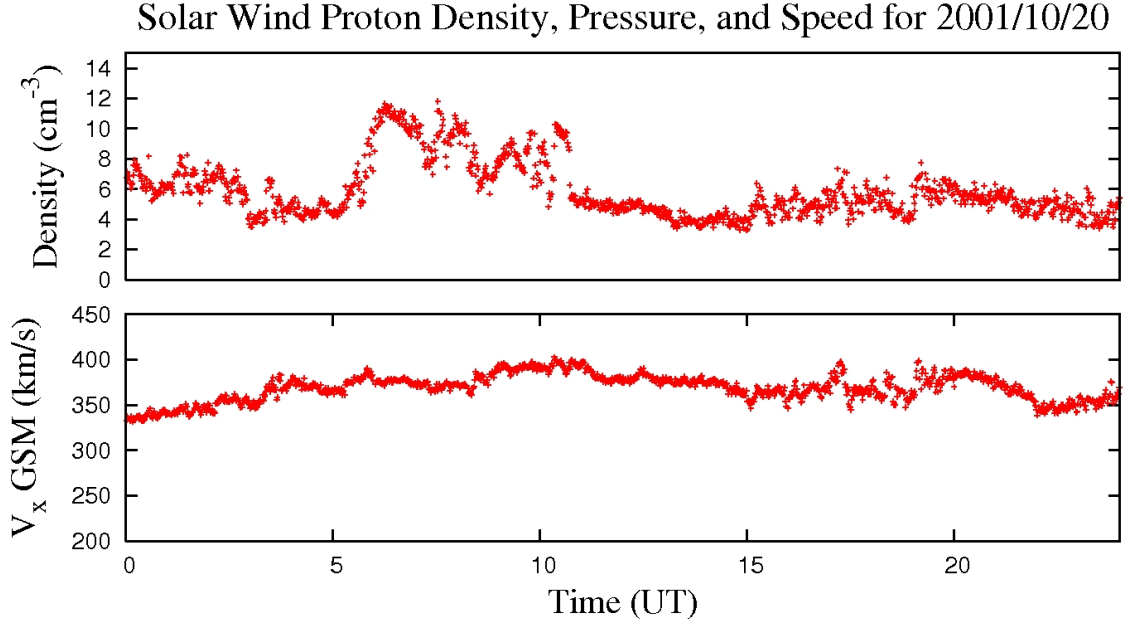


**Figure 7.5:** From top to bottom: (1) the solar wind proton density, and (2) the proton velocity of the solar wind for October 20, 2001.

solar wind and IMF conditions. It is a simple ballistic delay for protons using the  $x$  component of the solar wind speed and the distance between ACE and the Earth's magnetopause. The proton density and proton speed allows one to determine the location of the magnetopause with the following equation from *Walker and Russell, 1995*,

$$L_{mp}[R_E] = 107.4(n_{sw}u_{sw}^2)^{-1/6}, \quad (7.1)$$

where  $n_{sw}$  is the solar wind proton number density adjusted for helium content in units of cubic centimetres,  $u_{sw}$  is the solar wind speed in kilometers per second,  $R_E$  is the radius of the Earth in kilometers, and  $L_{mp}$  is the number of  $R_E$  upstream the front of the magnetopause is located (*Walker and Russell, 1995*). Using a solar wind speed of 360 km/s and an adjusted proton density of  $6 \text{ cm}^{-3}$ , the location of the magnetopause was estimated to be  $11.2 R_E$  upstream. The location of ACE varied 0.063% over the day and therefore can be considered stationary at a location of  $1.4 \times 10^6$  km upstream. The calculated time delay is therefore roughly 62 minutes, and due to the uncertainties in the estimates, for the purpose of this case study a time delay of 60 minutes was used.

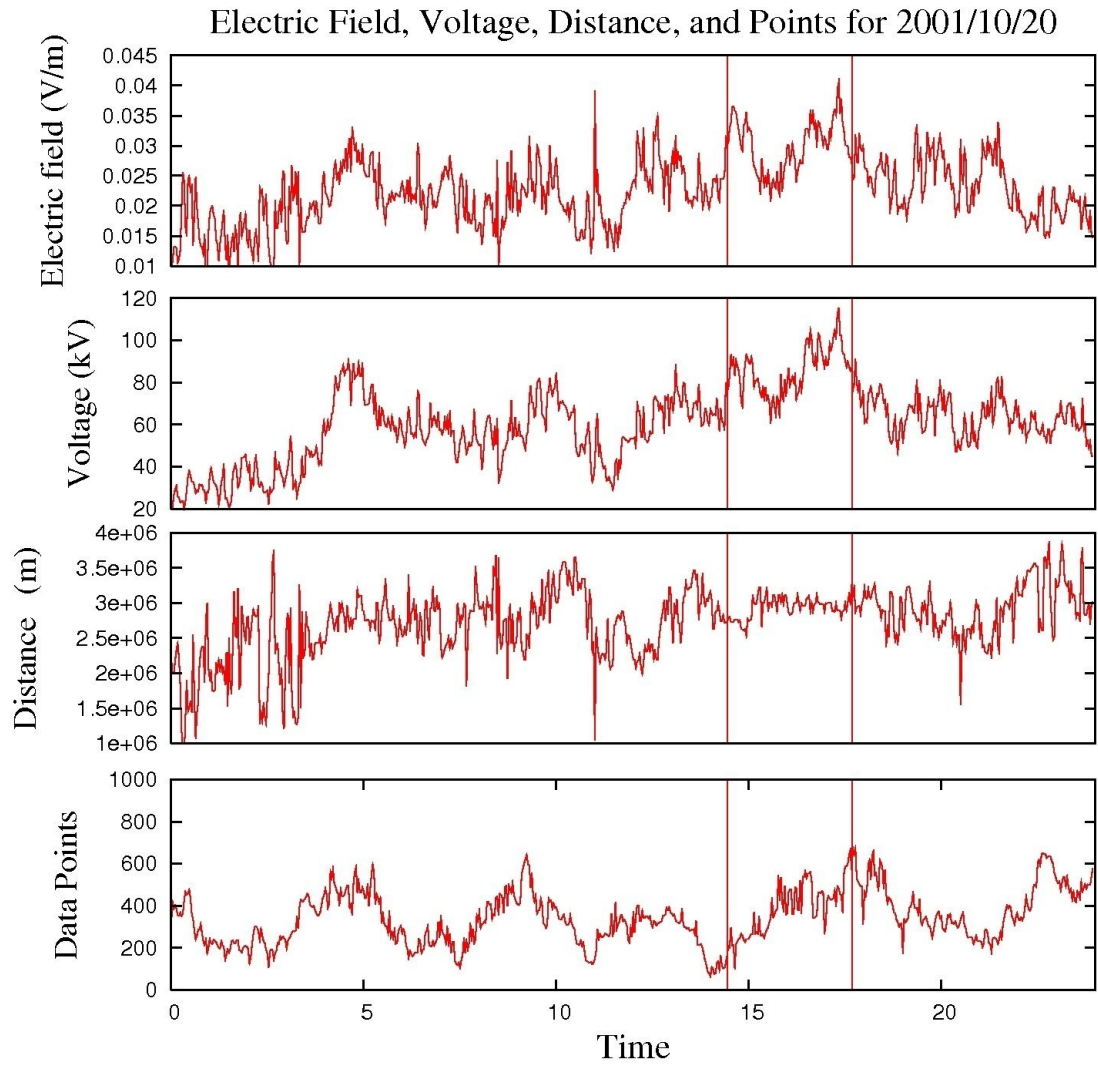


**Figure 7.6:** From top to bottom: (1) the average cross polar cap electric field, (2) the PCPD, (3) the distance between voltage centres, (4) the number of data points in the SuperDARN convection maps for October 20, 2001.

The SuperDARN convection maps were produced with the ACE data time shifted by 60 minutes. SuperDARN parameters of interest are presented in Figure 7.6. On average the PCPD (second panel) was largest during the SMC event, exceeding 100 kV at times. The convection electric field (top panel), which was determined according to the method described in section 6.1.2, was also very enhanced during the SMC. A decrease in both the voltage and the cross polar cap electric field were observed near the time of the identified substorm onset but interestingly the distance between the voltage centres (third panel) was very steady. In fact, the distance was much steadier during the SMC. The number of SuperDARN data points (bottom panel) increased from 200 to 600 during the SMC event. The large number of data points is a good indicator that SuperDARN measurements are strongly influencing the convection map fitting process.

## 7.2 SMC Case Study 2: October 30, 2001

SMC case study 2 occurred on October 30, 2001. This is an example of a SMC interval that would not have been identified using the traditional 200 nT AE threshold but was detected using the new variable AE threshold. Two events were identified. SMC Event 2a occurred from 4:33 UT to 7:47 UT, and SMC Event 2b occurred from 8:23 UT to 11:48 UT. The AE index and AL index for this day are presented in Figure 7.7. The horizontal dashed line in the top panel indicates the enhanced convection AE cutoff of 93 nT for this particular day, as determined using Equation 5.2. The AE index was above 93 nT from roughly 1 UT until the end of SMC event 2b. There was a noticeable rapid decrease of the AL index to near -400 nT at 4:30 UT. The sharp drop in the AL index resembled the classic AL signature of a substorm. SMC event 2a began at 4:33 UT. During the course of this SMC the AL index climbed back to -100 nT, peaking near 6 UT. The AL index then gradually became more negative. This decline continued till 7:47 UT when the AL index dropped sharply to -400 nT. This was the second substorm signature observed in the AL index on this day and also marked the end SMC Event 2a. This

is consistent with the work of *Sergeev et al. (1995)*, in which all SMC events studied began and ended with substorms. SMC Event 2b began shortly after at 8:23 UT and lasted until 11:48 UT. Unlike Event 2a this one did not end with a substorm. Event 2b ended after a gradual decrease of AE.

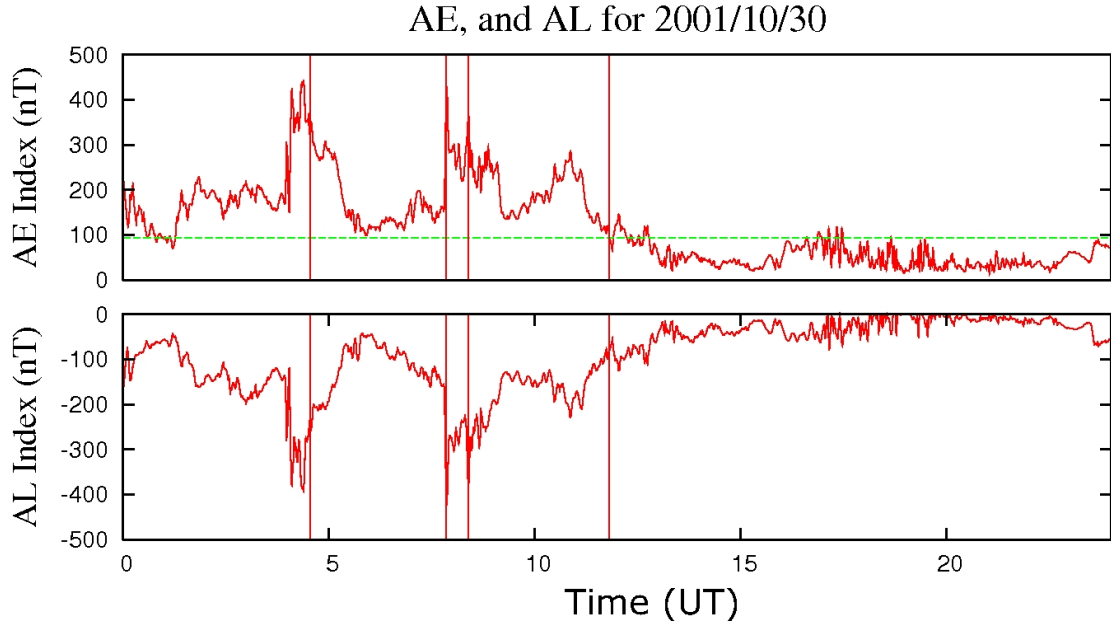


**Figure 7.7:** From top to bottom: (1) AE index and, (2) AL index for October 30, 2001. The start and end times of SMC Event 2a and 2b are indicated by the vertical lines.

Figure 7.8 provides a general overview of the auroral images from IMAGE WIC recorded during SMC Event 2a. Figure 7.8 is presented in the same format as Figure 7.3 for Event 1. The polar cap area contour for October 30, 2001 was determined at the 550 raw count level, which is the same value used in case study 1. Because the background instrument count levels are different on this day, a comparison of the absolute polar cap area of the SMCs should not be performed. The area estimates are intended to illustrate relative changes for a particular interval. The WIC instrument has a good view of the auroral oval during nearly all of Event 2a. During Event 2b, however, the WIC could not observe the northern auroral oval because of the spacecraft’s position.

The intensity of the aurora near midnight began to increase after about 1 UT, at roughly the same time as the AL index began to slowly decrease. These character-

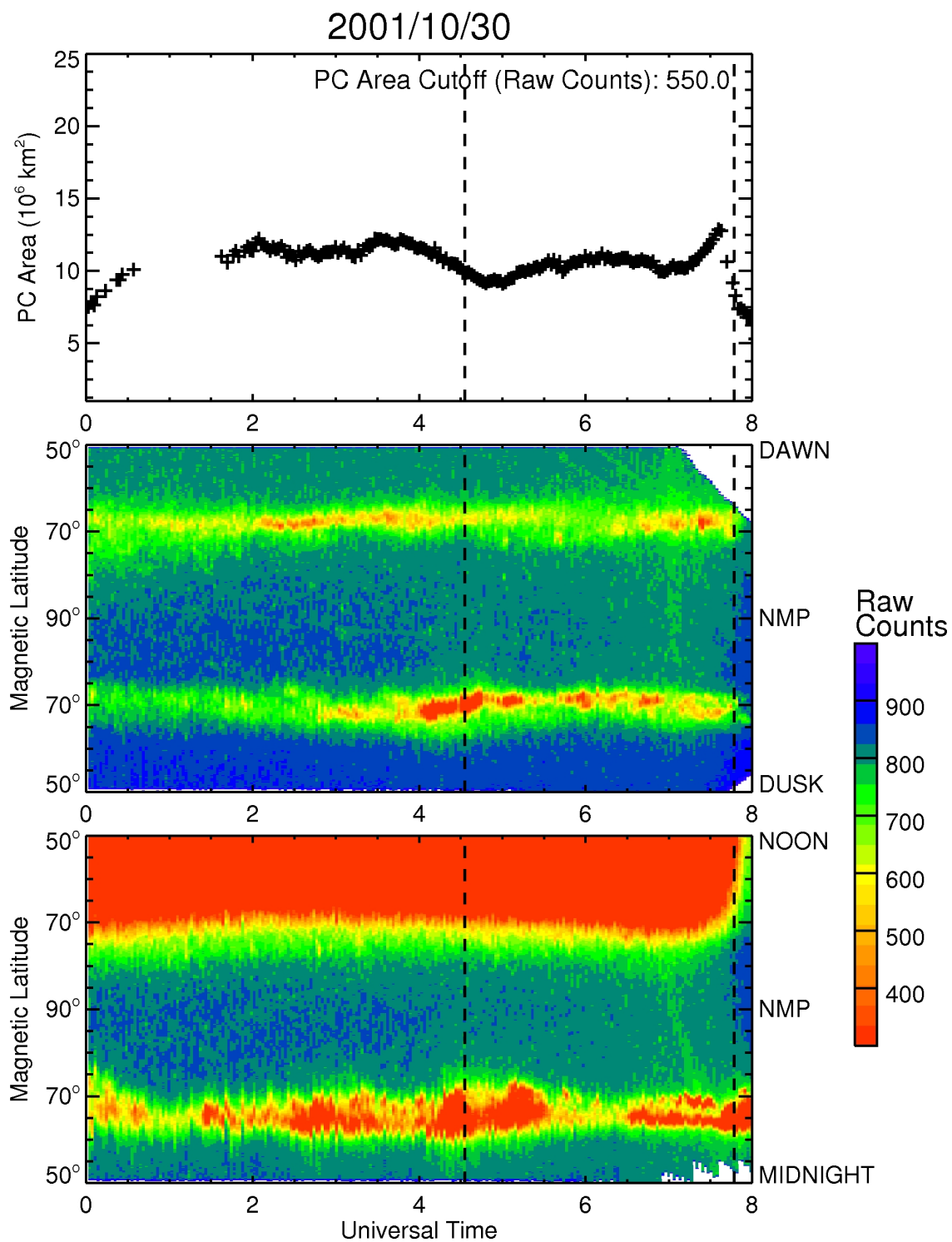


**Figure 7.8:** From top to bottom: (1) the polar cap area, (2) the keogram from dawn to dusk, and (3) the keogram from noon to midnight on October 30, 2001. The start and end of SMC Event 2a is denoted by the vertical dashed lines.

istics are consistent with those of substorm growth phase (*Elphinstone et al.*, 1996), but the conditions persist from 1 UT to 4:20 UT, which is longer than a typical growth phase.

Before the onset of SMC Event 2a at 4:20 UT the AL index (Figure 7.7) was variable enough to violate the steady convection criterion of SMC. Interestingly, the polar cap area measurements made during this time (Figure 7.8), indicate that the polar cap area was stable near  $1.2 \times 10^7$  km<sup>2</sup> with a standard deviation of the polar cap area equal to  $0.4 \times 10^6$  km<sup>2</sup> (3% of the mean). In addition to this 100% of polar cap area values fell within 10% of the mean area during this period, suggesting that convection may have been steady during this period. This contradiction again brings attention to the discrepancy between the steady convection requirement of *O'Brien et al.* (2002) ( $dAL/dt \geq -25$  nT/min) and the polar cap area measurements. The steady convection requirement of *O'Brien et al.* (2002) was an empirical rule of thumb and reassessment is needed, particularly in the winter months when the new AE cutoff can be as low as 90 nT.

At about 4:20 UT the AL index decreased rapidly from -150 nT to -400 nT. The onset of this substorm was present in the auroral data, as the noon-midnight keogram reached its most poleward extent at roughly 4:20 UT. The polar cap area decreased from 4 UT until just after the onset of the SMC.

During SMC Event 2a the area of the polar cap was stable. The average polar cap area during the interval was  $10^7$  km<sup>2</sup> with a standard deviation of  $0.68 \times 10^5$  km<sup>2</sup> (7% of the mean). The mean polar cap area for the day was  $9.0 \times 10^6$  km<sup>2</sup> with a standard deviation of  $2.6 \times 10^6$  km<sup>2</sup> (29% of the mean). Like SMC Event 1, the polar cap area was less variable during this SMC interval than all data obtained during the day. Of the 93 polar cap area estimates recorded during SMC Event 2a, 95% fell within 10% of the hourly mean. The 276 non-SMC data points had 47% within 10% of the hourly mean. Like SMC Event 1, the polar cap area was less variable during this SMC interval than all non-SMC data obtained during the day.

In Figure 7.9 the unshifted IMF components and magnitude from ACE are shown. Near 0 UT the IMF Bz component became negative and stable at -2.5 nT.

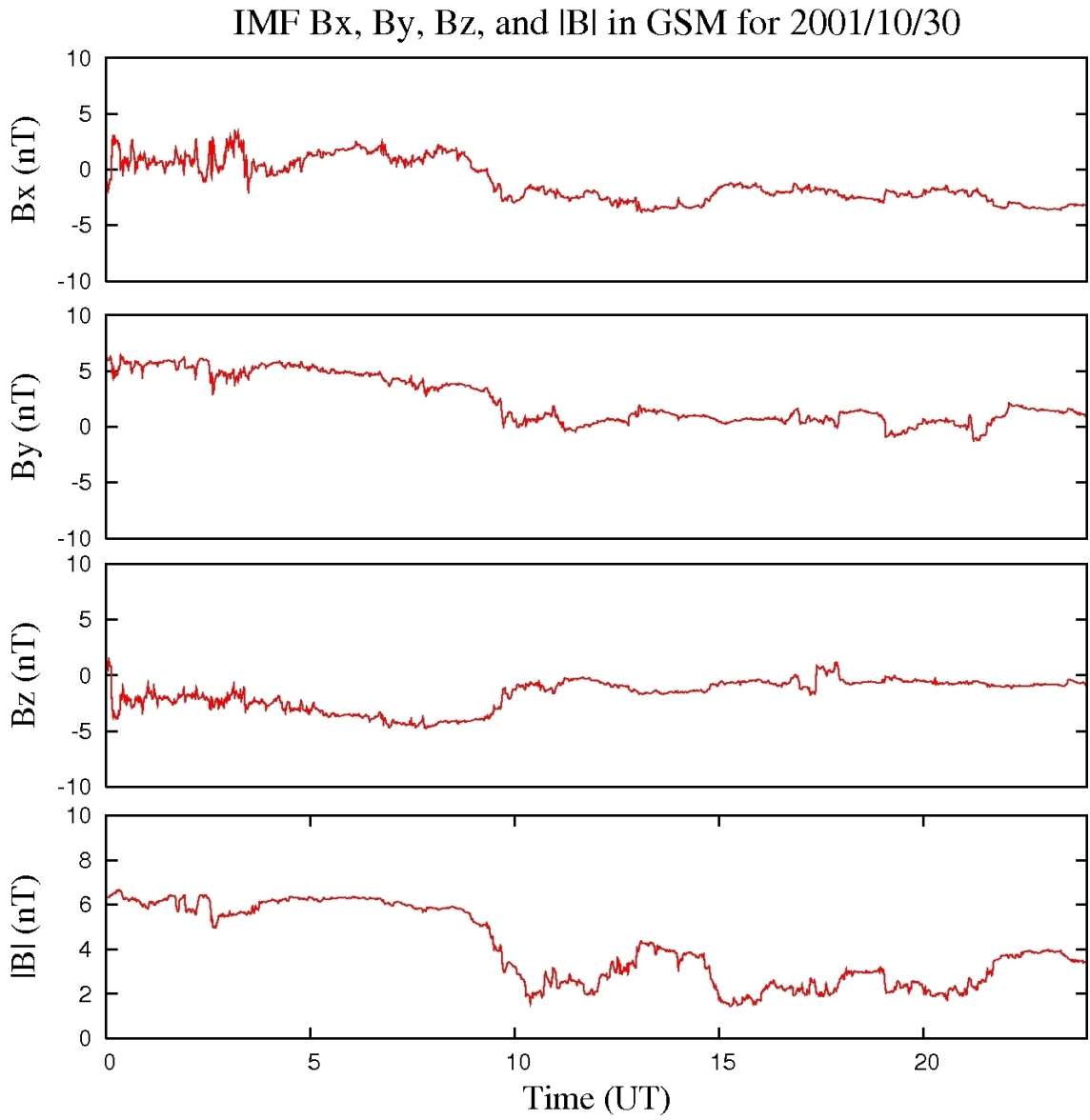


**Figure 7.9:** From top to bottom: (1) IMF  $B_x$ , (2) IMF  $B_y$ , (3) IMF  $B_z$  and, (4) IMF magnitude in GSM coordinates for October 30, 2001.

At 10 UT the IMF Bz component increased fairly rapidly to 0 nT. The IMF By component decreased very slowly from 5 nT to near 0 nT from 0 UT to 10 UT. IMF Bx, which was near 0 nT until 9 UT, experienced the opposite trend of IMF Bz, dropping relatively quickly around 10 UT to -2.5 nT.

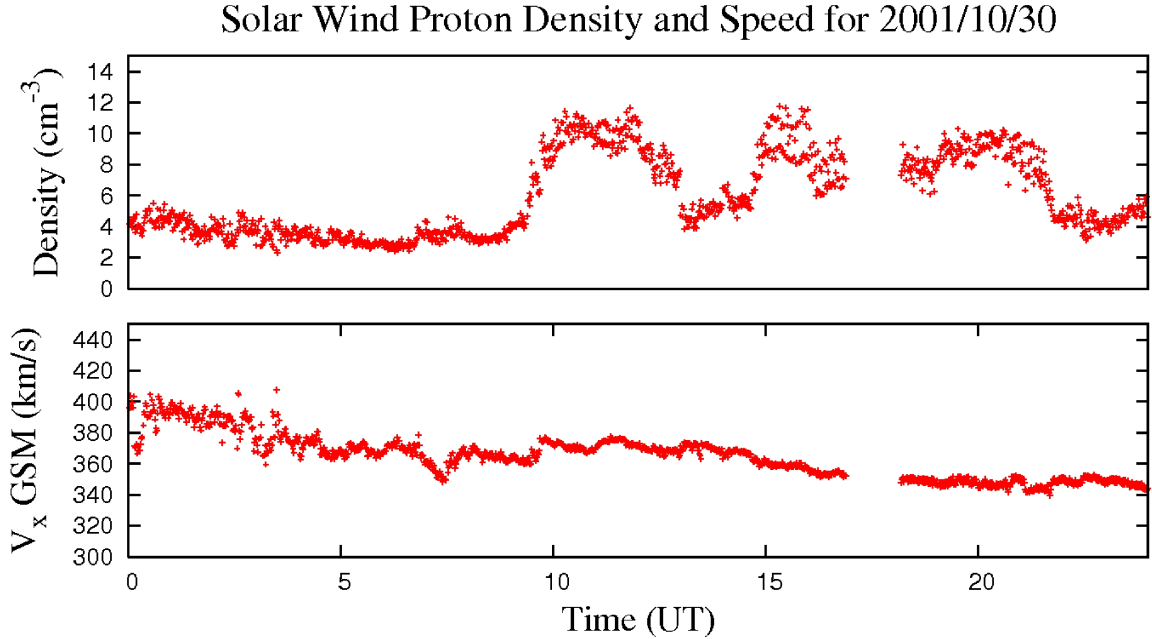


**Figure 7.10:** From top to bottom for: (1) the solar wind proton density, and (2) the proton velocity of the solar wind for October 30, 2001.

As in Section 7.1, the solar wind and IMF measurements made by ACE are used to estimate the time delay from ACE to the magnetopause. The proton speed and density from ACE SWE for October 30, 2001, are presented in Figure 7.10. Over the course of the day the proton speed is fairly steady. It decreases very slowly from about 400 km/s to just below 350 km/s. The position of the ACE satellite did not change substantially, changing less than 0.1% during the day. This is small enough that the ACE satellite can be considered stationary at  $1.4 \times 10^6$  km upstream.

The estimated location of the magnetopause was calculated using Equation 7.1. The magnetopause was roughly constant for the first 10 hours of the day because the properties of the solar wind were so stable. A proton speed of 375 km/s was used with a proton density, adjusted for alpha particles, of  $5.2 \text{ cm}^{-3}$ . The magnetopause was found to be located roughly 11 Earth radii upstream, leaving a distance

of  $1.34 \times 10^6$  km between ACE and the magnetopause. With the proton speed of 375 km/s the time delay was 60 minutes.

At roughly 9:30 UT there was a sharp increase in the proton density when it suddenly tripled from  $4 \text{ cm}^{-3}$  to  $12 \text{ cm}^{-3}$ . This increase in proton density will affect the estimate of the position of the magnetopause. With a solar wind speed of 375 km/s and a proton density of  $14.3 \text{ cm}^{-3}$ , adjusted to account for the percentage of alpha particles in the solar wind, the magnetopause moved to roughly 9.5 Earth radii, leaving a distance of  $1.35 \times 10^6$  km between ACE and the magnetopause. The time delay was still 60 minutes.

The SuperDARN data are presented in Figure 7.11, and these consist of the PCPD, the convection electric field, the distance between voltage centres, and the number of SuperDARN data points. The maximum voltage occurred after the onset of SMC Event 2a, and in general the PCPD values were largest during the SMC intervals, indicating that convection was enhanced. Like SMC Event 1 in Section 7.1, the distance between voltage centres was not highly variable, so the changes in the electric field are very similar to those in the PCPD. Both PCPD and the convection electric field gradually decreased towards the end of the SMC Event 2b. This is consistent with the SMC terminating when the enhanced convection AE criterion was no longer satisfied. This is in contrast with SMC Events 1 and 2a which both terminate due to rapid changes in AL. The number of SuperDARN data points recorded on this day was high. From 0 to 5 UT there were between 600 and 800 data points in each map. From 5 UT to 11 UT the number of data point was more than 400.

The set of observations during SMC Case Study 2 are greatly augmented by the data from geosynchronous satellites GOES-8 and GOES-10. The satellites orbit on the Earth's nightside where they were monitoring magnetotail conditions. The GOES satellites are operated by the National Oceanic and Atmospheric Administration who make the data publicly available through the National Geophysical Data Center (<http://goes.ngdc.noaa.gov/data/avg/>).

The magnetic field instruments onboard the GOES-8 and GOES-10 record

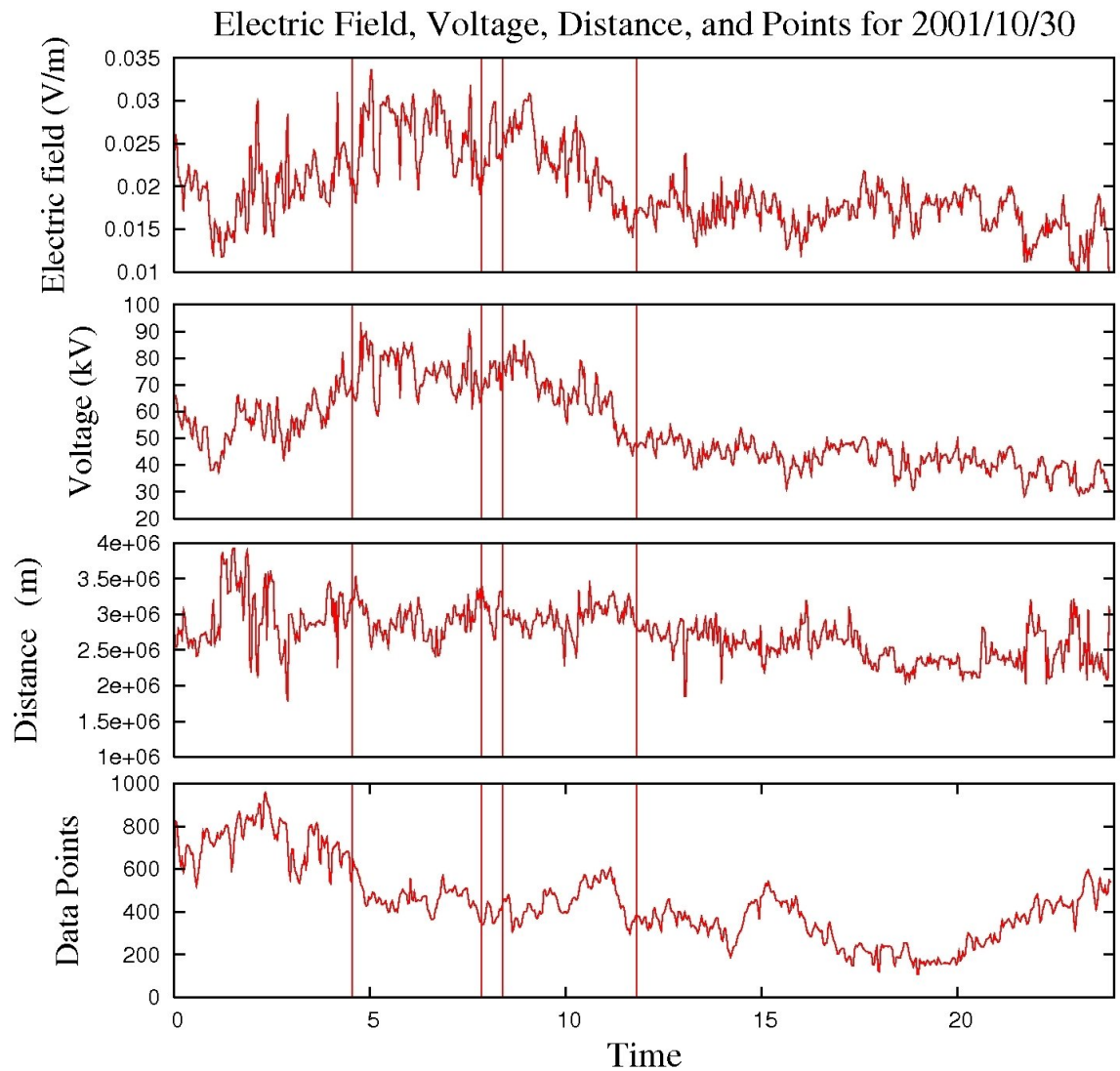


**Figure 7.11:** From top to bottom: (1) the average cross polar cap electric field, (2) the PCPD, (3) the distance between voltage centres, (4) the number of data points in the SuperDARN convection maps for October 30, 2001.

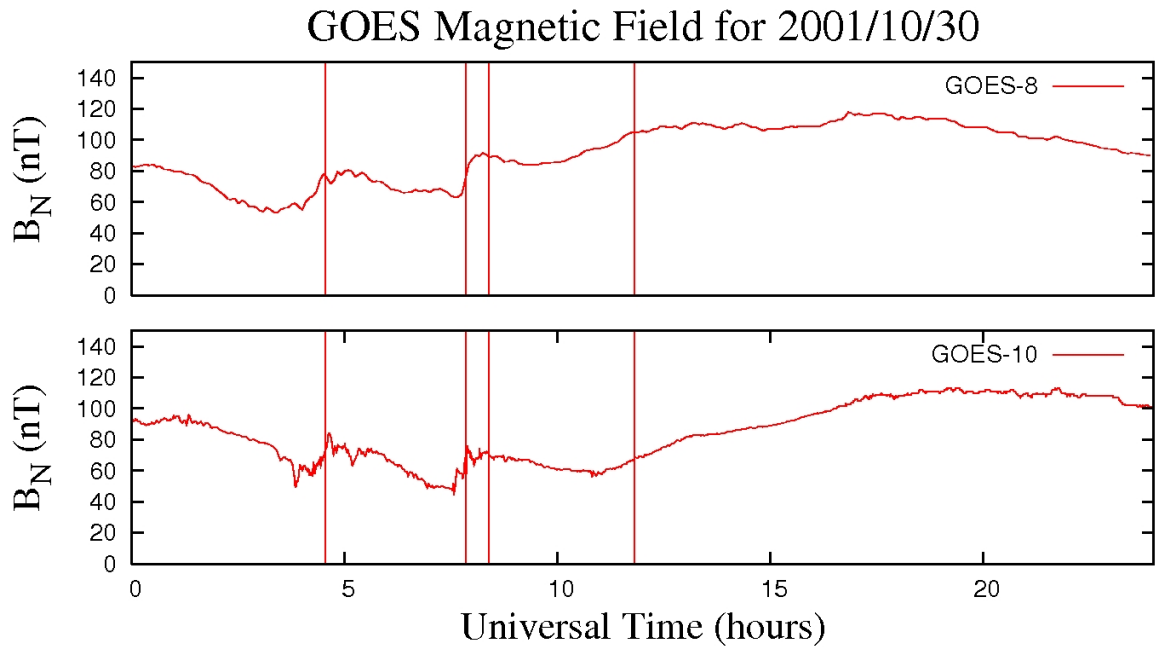


**Figure 7.12:** The northward magnetic field component measured at the GOES-8 and GOES-10 satellites on October 30, 2001. (data courtesy of National Geophysical Data Center (<http://goes.ngdc.noaa.gov/data/avg/>))

three components: northward, eastward, and earthward. GOES-8 orbits at a fixed geographic longitude of  $75^\circ$  West over North and South America and the Atlantic Ocean. GOES-10 orbits at  $135^\circ$  West geographic longitude over North America and the Pacific Basin. Figure 7.12 displays the northward magnetic field components measured at GOES-8 and GOES-10 on October 30, 2001. The northward magnetic field component is an indicator of the degree of stretching of the magnetotail, and the largest values correspond to the least stretched or most dipolar configuration. At 0 UT GOES-8 was located approximately at 19 MLT, and GOES-10 was near 15 MLT. From 0 UT to 4:20 UT the northward component decreased from nearly 90 nT to 60 nT at both satellites, which indicates a gradual change from dipolar to stretched. This could be simply due to the satellite orbiting from the dusk sector into the midnight sector, where the field naturally becomes less dipolar. At the time of substorm onset, 4:20 UT, there was a dipolarisation of the magnetic field in the magnetotail. The associated increase in the northward field component was detected at both satellites. In situ measurements of the magnetotail indicate signif-

icant reconfiguration of the magnetotail occurred between 4 and 5 UT during the first substorm.

During SMC Event 2a, GOES-8 measured a northward component that was fairly stable, decreasing gradually from 80 nT to about 70 nT. GOES-10 reported a slightly more variable northward component which gradually decreased from 70 nT to 50 nT. At the end of the first SMC both satellites recorded a sharp dipolarisation, evident in the sharp increase in the northward magnetic field component. This dipolarization corresponded with the second substorm onset that was seen in the AL data and this terminated SMC Event 2a.

GOES-8 was located in the dawn sector during the course of the second SMC event. The northward component at GOES-8 gradually increased from 80 nT to 100 nT. GOES-10 was located in the midnight sector when the second SMC event began. It too reported a fairly constant northward component at 70 nT. Both GOES satellites provide evidence to suggest that the magnetotail did not experience any sudden reconfiguration, such as those due to a substorm, during or following SMC Event 2b.

### **7.3 Sawtooth Case Study: October 21, 2001**

The sawtooth event that occurred on October 21, 2001, was one of a set identified by M. Henderson and R. McPherron (personal communication). This sawtooth event had four individual “teeth” occurring at 16:46 UT, 18:34 UT, 20:00 UT, and 23:07 UT. Because this sawtooth event occurred one day after the SMC on October 20, 2001, and nine days before the SMCs on October 30, 2001, the photo-conductivity conditions in the ionosphere are very similar for all events. With similar conductivity conditions the AE indices are expected to be a fairly consistent indicator of the relative level of convection for these events.

The AE and AL indices from October 21, 2001 are presented in Figure 7.13. The onset times of four “teeth” are indicated by vertical lines. Following the onsets, the AE index became extremely large very quickly, reaching values near 1500 nT

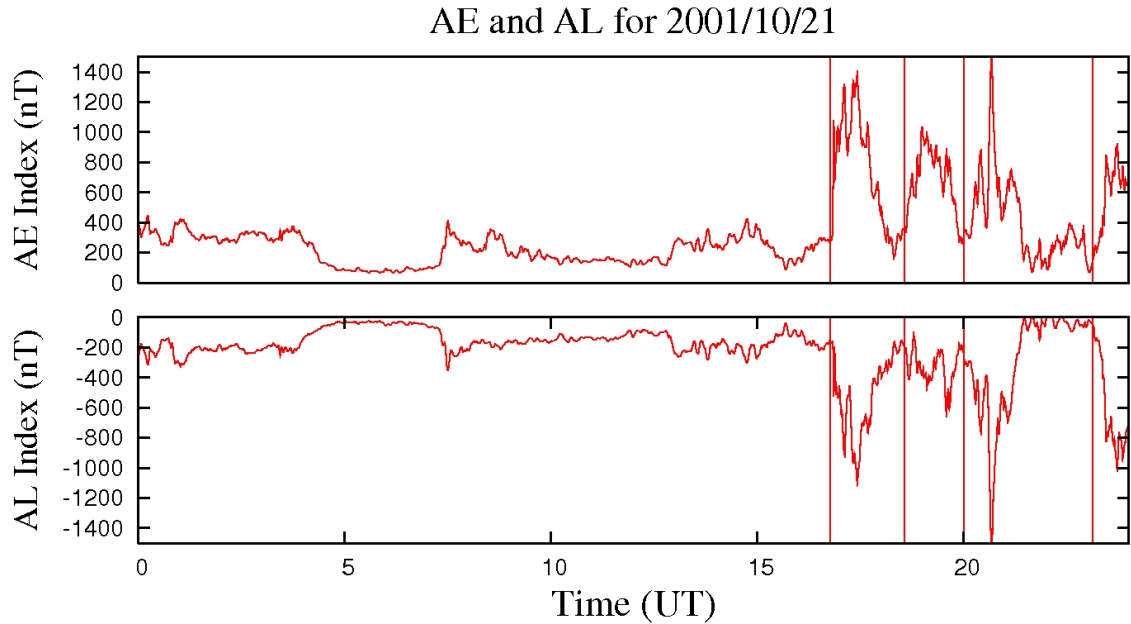


**Figure 7.13:** From top to bottom for: (1) the AE index and, (2) the AL index for October 21, 2001. Vertical lines mark sawtooth onsets.

in a matter of minutes. The magnitude of the AL index became very large as well during these events, indicating that a large substorm current wedge was present. Interestingly, while all events had a large enhancement of AE, the second event starting at 18:34 UT did not experience a correspondingly large deflection of AL. It is not known why this event differs from the others, but it may be related to poor magnetometer operation at a few stations, since only 8 out of a possible 12 AE magnetometer stations were in operation that day. The AE and AL enhancements during the sawtooth case study are much larger than those observed during the SMC events presented, indicating that the AE current system is much more enhanced during the sawtooth intervals.

The IMAGE satellite was able to make auroral luminosity measurements of the entire auroral oval during nearly the entire sawtooth case study. With the WIC images estimates of the polar cap area could be obtained for nearly 10 hours. Qualitatively and quantitatively the polar cap area measurements in Figure 7.14 are in stark contrast to those obtained during the previously studied SMCs. The raw counts detected by WIC were much higher than those during the SMC intervals, so a different value had to be chosen for a polar cap threshold. A value of 700 raw counts

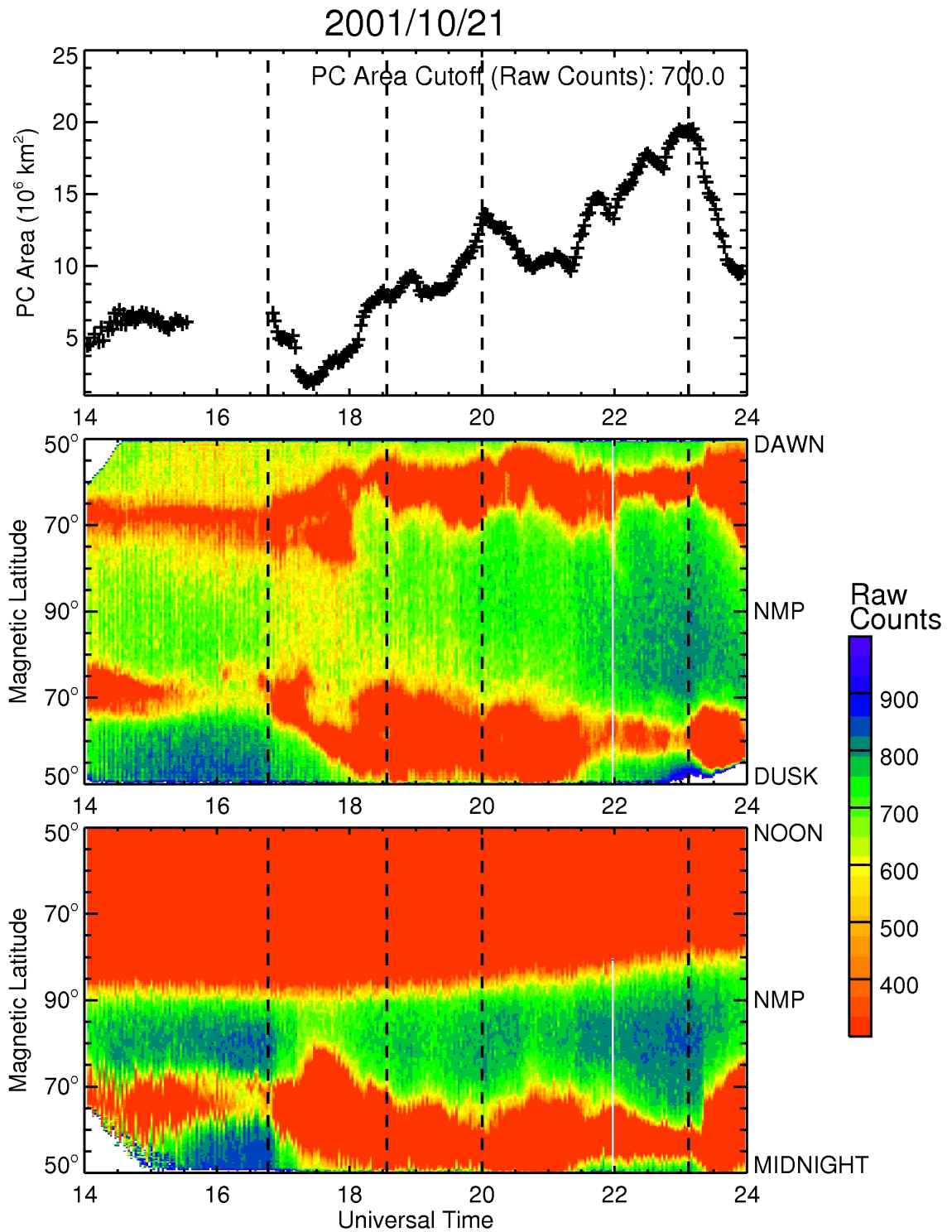


**Figure 7.14:** From top to bottom: (1) the polar cap area, (2) the keogram from dawn to dusk, and (3) the keogram from noon to midnight on October 21, 2001. The sawtooth onset times are denoted by the vertical dashed lines.

was used. Like the SMC cases, it is not appropriate to consider the absolute value of the polar cap size, rather it is the relative change in size that is important. Over the day the area of the polar cap varied from  $10^6$  km<sup>2</sup> up to  $2 \times 10^7$  km<sup>2</sup>, indicating that conditions were far from steady during this sawtooth event. The mean polar cap area during this day was  $9.9 \times 10^6$  km<sup>2</sup> with a standard deviation of  $5 \times 10^6$  km<sup>2</sup> (50% of the mean). The polarcap area was highly variable during this day as compared to both SMCs studied. Furthermore, of the 254 polar cap area measurements made, 42% were within 10% of the mean. The variability of the polar cap area supports previous studies (e.g., *Henderson et al.*, 2006, *DeJong et al.*, 2007) that convection is steadier during times of SMC. A steady polar cap area implies the reconnection rates on the dayside are balanced with the reconnection rates in the magnetotail.

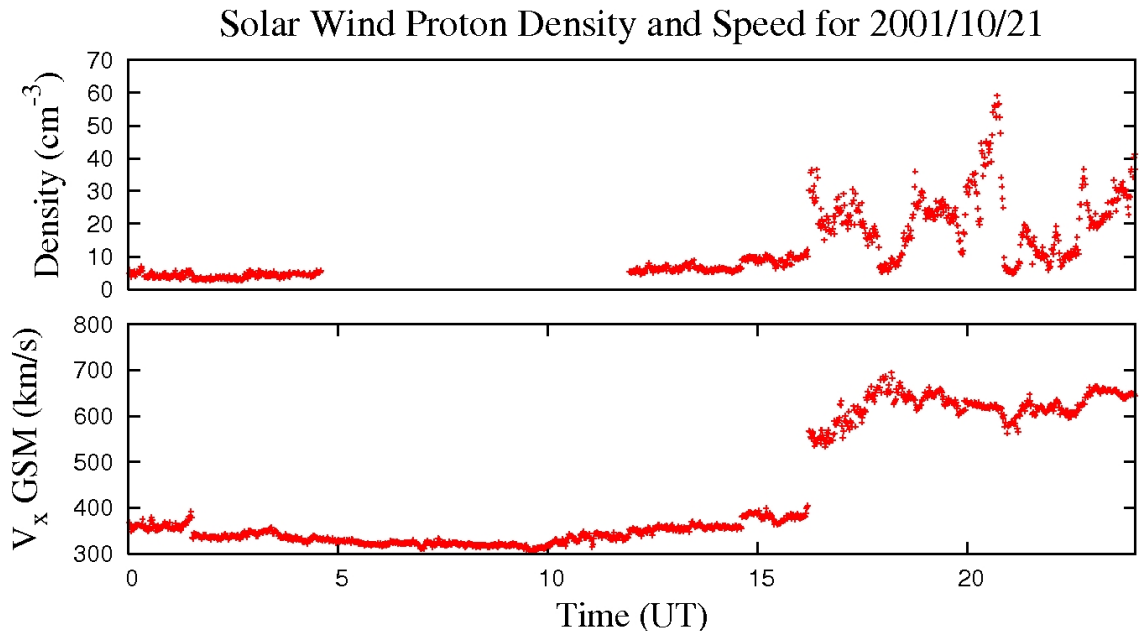


**Figure 7.15:** From top to bottom for the day: (1) the solar wind proton density, and (2) the proton velocity of the solar wind for October 21, 2001.

The solar wind conditions recorded on October 21, 2001 are displayed in Figure 7.15. Measurements of solar wind density were disrupted many times during this day, leading to the large data gaps in the top panel of Figure 7.15. Solar wind conditions were calm leading up to the sawtooth event. The solar wind proton density was roughly  $5$  cm<sup>-3</sup>, with speeds below 400 km/sec. Near 16:15 UT, about a

quarter of an hour before the onset of the first sawtooth at 16:46 UT, the solar wind speed increased very rapidly to 650 km/s. Simultaneously the density also increased suddenly up to  $30 \text{ cm}^{-3}$ . For the duration of the sawtooth event the solar wind speed was in excess of 600 km/s and quite steady. The solar wind density, in contrast, was far from steady. Three large fluctuations occurred at 16:30 UT, 17:30 UT, and 20:00 UT. These density enhancements should also correspond to increases in solar wind ram pressure, since the solar wind speed remained stable. Based on the solar wind plasma data, it is possible that several of the sawteeth could have been triggered by solar wind pressure pulses.

The IMF conditions at ACE on October 21, 2001, are presented in Figure 7.16. During the hours leading up to the sawtooth event IMF Bz and IMF Bx were nearly 0 nT, while IMF By was about 8 nT. All components were very stable. At roughly the same time as the solar wind pressure and speed increased IMF Bz and IMF By changed sharply to -20 nT and 20 nT, respectively. The IMF magnitude also jumped from 8 nT to 25 nT at this time and remained large for the duration of the sawtooth event. All three IMF components experienced large variations throughout the rest of the day, and rapid rotations of the magnetic field occurred at about the same time as the large changes in the proton density.

In order to produce the SuperDARN convection maps for the sawtooth interval with ACE data, it is necessary to estimate the time delay from ACE to the magnetopause for these solar wind conditions. For the SMC cases the time delay to the magnetopause was estimated using the solar wind speed and proton density. Fortunately, for the sawtooth event there is a much more accurate method of timing. The GOES-8 and GOES-10 satellites were on the dayside of the Earth at the time of the first sawtooth. When in the dayside, geosynchronous satellites are in an excellent location to detect impulsive solar wind disturbances, such as pressure pulses, when they perturb the middle magnetosphere. The northward magnetic field component at GOES-8 and GOES-10 are presented in Figure 7.17. The identified onset time of each sawtooth is marked by vertical dotted lines in Figure 7.17. At the onset of the first sawtooth the GOES-8 satellite was located near 12 MLT. The

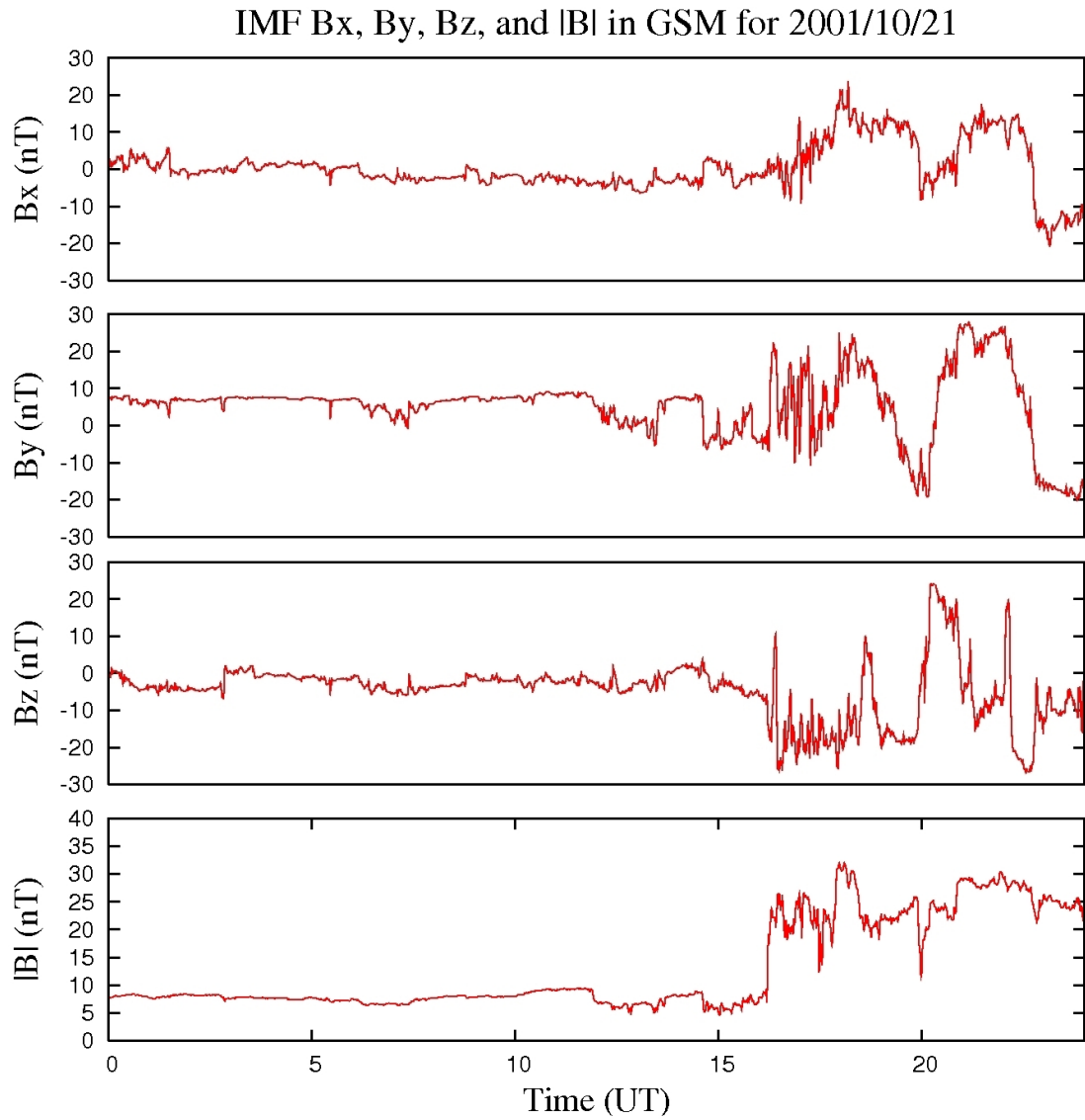


**Figure 7.16:** From top to bottom: (1) IMF Bx, (2) IMF By, (3) IMF Bz and, (4) IMF magnitude in GSM coordinates for October 21, 2001.

northward magnetic field component increased sharply to nearly double its initial value and then reversed to an equally large value in the southward direction. The large southward deflection indicates that GOES-8 crossed the magnetopause and entered the magnetosheath. GOES-10 which was in the dawn sector near 8 MLT recorded the initial response to the pressure pulse at 16:51 UT, which is the same time it was observed at GOES-8. Therefore according to the northward magnetic field components at GOES-8 and GOES-10 the time delay from ACE should be 36 minutes. It took 40 minutes after 16:51 UT before GOES-10 detected the strong southward magnetic field component of the magnetosheath. This delay was due to the time required for GOES-10, which was initially in the dawn sector to orbit close to the highly compressed frontside magnetopause.

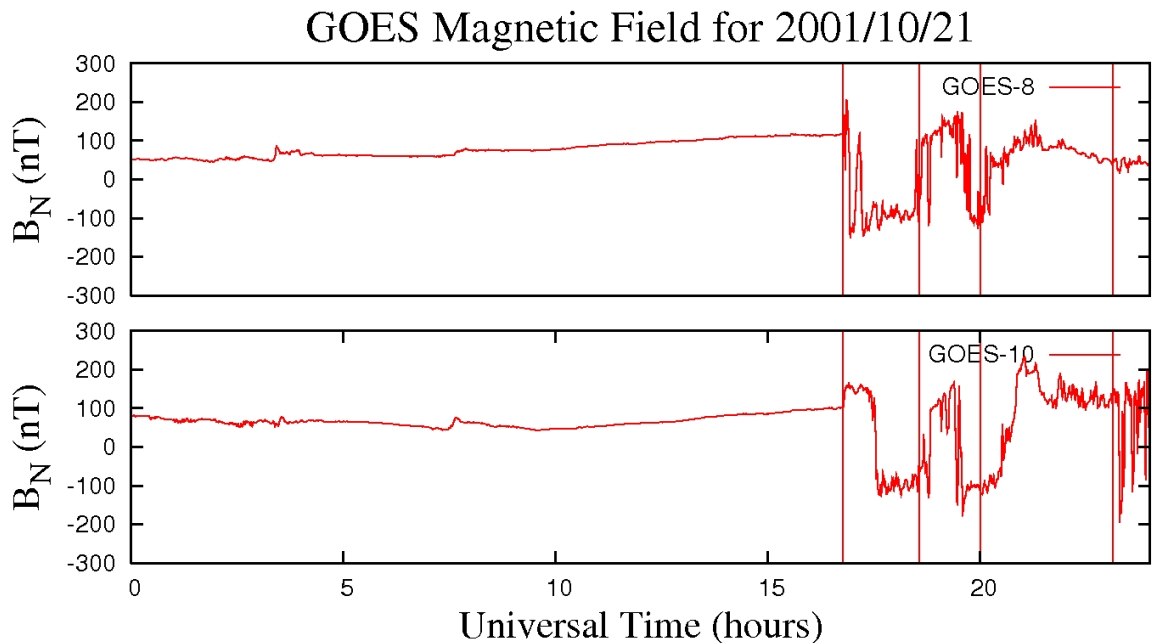


**Figure 7.17:** The northward magnetic field component measured at the GOES-8 and GOES-10 satellites on October 21, 2001. (data courtesy of National Geophysical Data Center (<http://goes.ngdc.noaa.gov/data/avg/>))

The time delay was also calculated based on the solar wind conditions at ACE. During this day the location of ACE varied 0.063%, so once again ACE can be considered stationary at a distance of  $1.4 \times 10^6$  km upstream. During the sawtooth event the solar wind speed  $x$  component was roughly 650 km/s. There were several

proton density fluctuations over the course of this event. The maximum proton density adjusted for helium content was roughly  $77 \text{ cm}^{-3}$  and the minimum proton density adjusted for proton content was  $5.6 \text{ cm}^{-3}$ . Equation 7.1 was again used to estimate the location of the magnetopause. For the maximum proton density the magnetopause was located 6.0 earth radii upstream. Therefore the time delay should be 35 minutes. For the minimum proton density the magnetopause was 9.3 Earth radii upstream, leading to a time delay of 34 minutes. The magnetopause distance of 6.3 is more consistent with GOES-8 and GOES-10, which orbit at  $6.6 R_E$ , crossing into the magnetosheath. These time delay estimations based on ACE data are very similar to the time delay obtained from feature matching in the ACE and GOES data streams.

SuperDARN provided measurements of ionospheric convection over the course of the sawtooth case study. The electric field, voltage, distance between voltage extrema, and the number of SuperDARN data points are displayed in Figure 7.18. On average, the SuperDARN had excellent coverage. On this day there were times when SuperDARN recorded close to 1200 data points. Values obtained from the SuperDARN convection maps are therefore highly reliable. To confirm this, two different time delays were used to shift the ACE data. A 60 minute time delay and a 30 minute time delay were both used, and both gave nearly identical results, indicating the initial statistical model was inconsequential for the resulting convection maps.

The onset of each sawtooth is marked by a vertical line in Figure 7.18. The magnitudes of these parameters were large for the duration of this sawtooth as well. The PCPD was greater than 100 kV at times, while the electric field neared  $40 \text{ mV/m}$ , indicating convection was very strongly enhanced. The distance between voltage centres was also large, having magnitudes close to  $5 \times 10^6 \text{ m}$ . The voltage, electric field, and distance between voltage centres was highly variable throughout the day as well. In general, the sawtooth event was much more disturbed and variable than the SMC case studies in all aspects, which is not unexpected.

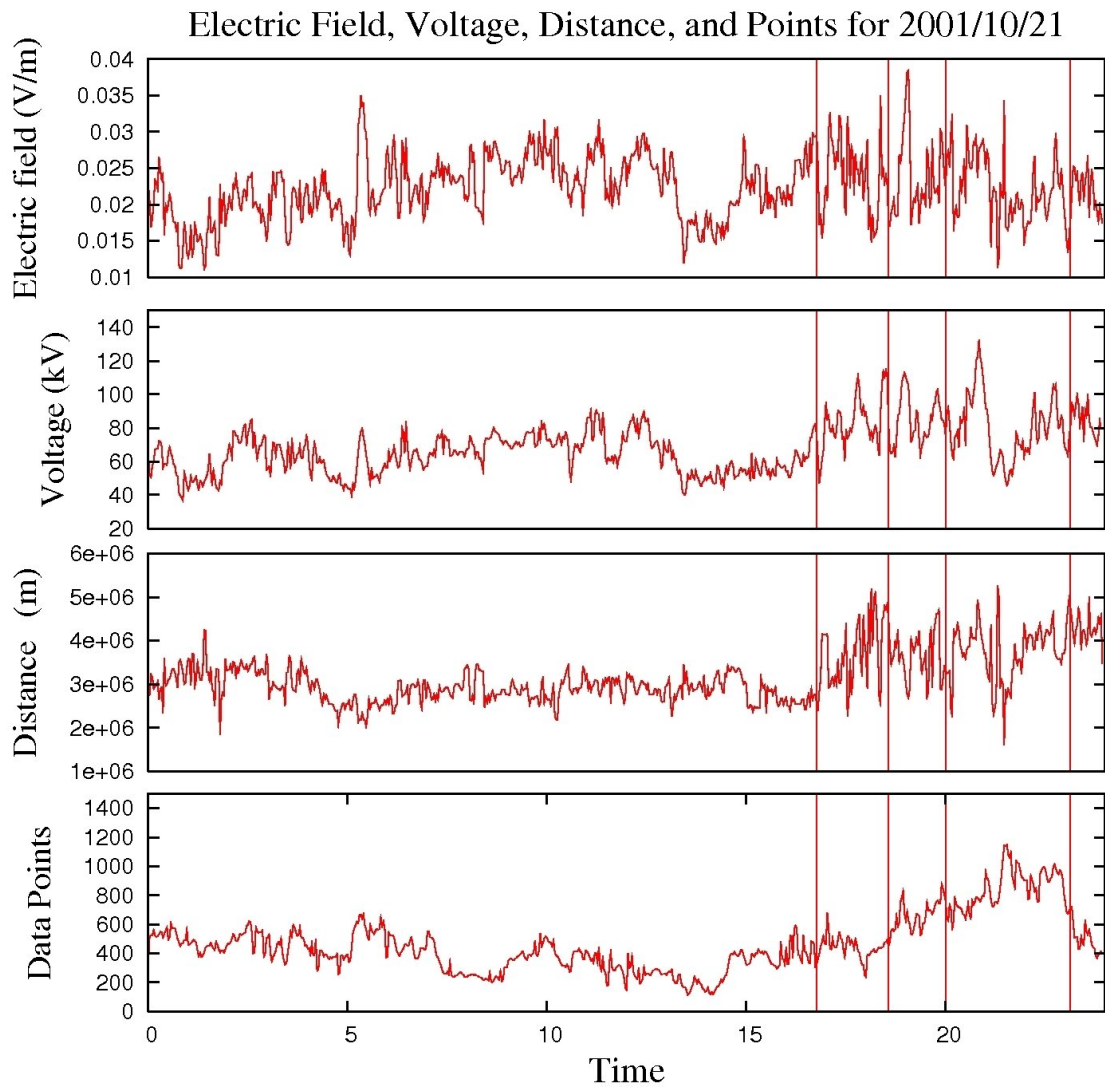


**Figure 7.18:** From top to bottom: (1) the average cross polar cap electric field, (2) the PCPD, (3) the distance between voltage centres, (4) the number of data points in the SuperDARN convection maps for October 21, 2001. The vertical lines mark sawtooth onsets.

## 7.4 Case Study Results

Based on the analysis presented in the three case studies, several things can be concluded regarding the variable selection method and SMC. Events selected by the variable SMC selection method displayed all the qualitative characteristics of SMC. When compared to an event selected using the modified SMC selection method of *O'Brien et al.* (2002), it was found that both resulted from moderate solar wind and IMF conditions and that both possess enhanced convection. To quantify the steadiness of convection a method similar to that of *DeJong and Clauer* (2005) was employed. During the SMC events the majority of polar cap area estimations fell within 10% of the hourly mean. There was also evidence that the steadiness requirement developed by *O'Brien et al.* (2002) was problematic. Future work will be required to refine this criterion.

The sawtooth case study revealed that magnetospheric convection is unstable during sawtooth events, resulting in drastic changes in the state of the magnetotail. SMC events, on the contrary, did not display similar large scale reconfiguration of the magnetotail.

# CHAPTER 8

## CONCLUSION AND FUTURE WORK

### 8.1 Summary

Steady magnetospheric convection (SMC) is qualitatively defined as times of enhanced convection in the magnetosphere during which the stability of the magnetotail is maintained. In the past, intervals of SMC have been identified and studied using data sets comprised of ground based magnetometer measurements, IMF conditions, and ultraviolet aurora images. The analysis of these data have increased our understanding of SMC and the dynamics of the magnetosphere. This positive progress was made despite that the data sets used were all the result of indirect observations of convection. SMC is a convection based phenomenon. This thesis is a presentation of the first statistical study of direct convection observations during SMC.

SuperDARN makes direct observations on a global scale of ionospheric convection. One must understand both the advantages and limitations of this tool before applying it to SMC studies. One limitation is that the SuperDARN radar network does not have enough radars to measure the entire ionospheric convection pattern. Complex algorithms are used to interpolate across the data gaps. These algorithms are based on statistical models and are highly dependent on the amount of data the radar network obtains. Many complex factors play into radio wave propagation, making continual data reception in every possible data volume nearly impossible. Because SuperDARN convection maps can be strongly influenced by an inherently steady statistical convection model, it is prudent to first identify SMC based on the previous work conducted by others and then use SuperDARN to study the conditions

that arise during SMC.

SMC events used in this thesis were initially selected based on the work of *O'Brien et al.* (2002). Before SuperDARN was even employed in this study a very interesting trend was discovered in the data set. The SMC events selected revealed strong solar cycle and seasonal dependences. Near solar maximum and during the northern summer months more SMC events were identified. The solar cycle variation was expected since convection varies with the solar cycle. The seasonal dependence, on the other hand, was not expected. Convection in the magnetosphere is not known to vary so drastically with season; therefore it is likely that the previous methods used to identify SMC are being effected by parameters other than convection.

SMC events selected using the modified method of *O'Brien et al.* (2002) were identified using ground based magnetometers that respond to auroral electrojet currents flowing in the ionosphere. These currents are not only controlled by convection but also depend on the conductivity of the ionosphere which, in turn, is highly dependent on the amount of sunlight that reaches the Earth. In winter months little sunlight reaches to the high latitudes resulting in low ionospheric conductivity, while in the summer months the more direct sunlight at high latitudes results in greater ionospheric conductivity. If one wishes to use ground based magnetometer measurements to quantify only convection, variable conductivity must be accounted for.

As a first attempt at eliminating this problem, the seasonal dependence displayed by the number of SMC events per month was largely reduced with a new variable-AE SMC selection method. The new requirements placed on ground based magnetometer measurements vary as a function of season to reduce the effects of variable ionospheric conductivity on SMC selection. With the seasonal dependence diminished, evidence was required to show that the variable-AE SMC selection method is an improvement on previous methods and identifies events based on a minimum convection threshold. SuperDARN global convection maps were used for this task.

SuperDARN can measure the ionospheric convection pattern once every two minutes. The level of convection in each pattern is usually quantified by a parameter called the cross polar cap potential difference (PCPD). The PCPD is not a true

measure of convection but is commonly used as a proxy. The larger this voltage measurement, the more enhanced convection is assumed to be. If the variable SMC selection method is selecting events based on a minimum convection threshold, the average PCPD should be roughly constant during all seasons. To compare the different methods the average SuperDARN PCPD was determined for the modified method of *O'Brien et al. (2002)* and for the variable-AE SMC selection method. To ensure that the conditions during these events were distinct from typical and non-enhanced magnetospheric activity, two additional test populations were studied. These populations consisted of randomly selected events, to quantify typical conditions, and events with low AE, to quantify low magnetospheric activity.

The events selected using the modified method of *O'Brien et al. (2002)* displayed a lower average PCPD in the summer as compared to the winter. This indicates that the events selected by the modified method of *O'Brien et al. (2002)* were not based on a minimum convection threshold. On the other hand, events selected with the variable-AE method displayed a more consistent voltage over the year. The randomly selected events also displayed roughly equivalent voltages for both winter and summer but had a yearly voltage average that was much lower than both SMC selection methods. The events with weak convection also had roughly equivalent voltages over the course of the year with a yearly average voltage that was lower than all other events sets.

The results from SuperDARN are quite promising, as they appear to support the hypothesis that conductivity causes the seasonal dependence of the total events distribution. These results however are not conclusive since the uncertainties in SuperDARN convection maps are unknown. Additional evidence is therefore required to support this claim.

To augment the evidence from SuperDARN a conceptual model of SMC detection was developed based entirely on conductivity. With several simplifying assumptions, an analytical average events distribution was produced. This resulting distribution displays the same seasonal trend as the experimental distribution obtained through the modified method of *O'Brien et al. (2002)*. The model provided

strong support that conductivity variations are contributing to the seasonal trend. In addition to this, the conceptual model implies that a flat distribution would be composed of events selected with a constant minimum convection threshold. Thus the combined evidence from SuperDARN and the conceptual model strongly support the hypothesis that seasonal changes in ionospheric conductivity caused the seasonal variation in the number of SMC events selected.

With an improved SMC selection method in place, it is important to show that the additional events satisfy the qualitative criteria of SMC. Properties of SMC can also be better determined quantitatively. Several approaches were used. The superposed epoch analysis is statistical in nature and allows one to examine in a general sense how conditions in the solar wind and the magnetosphere evolve during SMC. The superposed epoch analysis revealed that the IMF Bz component increases for about 2 hours before SMC onset. This trend was evident in SMCs selected using traditional and the new variable-AE methods.

The SuperDARN convection maps were also examined with the superposed epoch analysis. It was found that enhanced PCPD exists during the intervals selected with both the modified method of *O'Brien et al. (2002)* and with the variable SMC selection method. The SMC events were found to be enhanced in comparison to the typical and non-enhanced data sets. Leading up to SMC onset, there was an increase in PCPD. This “growth phase” lasted for about 2 hours.

SuperDARN PCPD is only a proxy for convection. This voltage depends not only on the strength of the convection electric field but also on the distance between the centres of the convection cells. The convection electric field is a much better measure of convection, but it is difficult to determine. To obtain an estimate of the average cross polar cap electric field, the value of PCPD was divided by the distance between the voltage extrema. The superposed epoch analysis showed that the polarcap electric field was enhanced during SMC and also had a similar “growth phase” leading up to SMC onset.

A superposed epoch analysis was also performed on the distance between voltage extrema. The cumulative distributions showed that the distance increased before

onset for both sets of SMC events. During the SMC events, however, there were no large changes in the distance. The superposed epoch analysis provides evidence indicating that the polar cap was large and stable during SMC.

The superposed epoch analysis of the number of data points in the SuperDARN convection maps revealed a gradual increase in data coverage. This was interesting because during unstable active times such as substorms the amount of SuperDARN often decreases. Since the SuperDARN data volume is not adversely affected by conditions during SMC, SuperDARN is a useful tool to study SMC.

The superposed epoch analysis was a very useful approach for statistical studies of the time evolution of SMC. A scatter plot analysis was performed to supplement the statistical studies with information about typical properties of SMC and relationships between them.

The scatter plot analysis of upstream IMF orientation revealed that SMC is driven by a moderately negative IMF  $B_z$  component and there is no preferred direction of IMF  $B_y$ . The extra SMC events detected using the variable-AE method appear to have a preponderance of large IMF  $B_y$  components. This may be indicative of a slightly weaker driving of convection by an IMF that is highly tilted from the southward.

The PCPD was most enhanced for the SMC events selected with the modified method of *O'Brien et al. (2002)*. The variable method possessed enhanced convection as well but to a lesser degree. In comparison to the test set, the scatter plot analysis suggests that enhanced PCPD is a defining feature of SMC.

PCPD can be a proxy for convection because it depends on the strength of convection, but it also depends on the distance between the centres of the convection cells. The scatterplot analysis was a very useful method to establish if there is a relationship between PCPD and distance. Comparing all events sets, the voltage did have a dependence on distance, with increased voltage for increased distance. The SMC events, however, did not display a clear trend. This result combined with the result from superposed epoch analysis indicates that the polar cap area does not change during SMC and may effectively decouple PCPD and distance during SMC.

The statistical approaches have shown that convection is enhanced for SMC events selected with both methods and that these events are driven by a moderately negative IMF Bz component. The evidence also suggests the PCPD is an effective proxy for convection during SMC.

Following the statistical analysis, a series of three case studies were presented. The first SMC case study was selected by both the modified method of *O'Brien et al.* (2002) and the variable-AE SMC selection method. The second event had a much weaker AE index overall and was only selected by the variable-AE SMC selection method. The third case study was of a sawtooth event, which was included for comparison with SMC.

The three main goals of the case studies were: (1) to show that SMCs selected by both methods possess enhanced and steady convection, (2) to show that the additional events selected by the variable AE method satisfy the qualitative requirements of SMC, and (3) to demonstrate that SMC is distinct from other active phenomena in the magnetosphere. The case studies employed a wide variety of data sets to give several perspectives. These data sets provided detailed information on the state of convection in the ionosphere on a global scale, the upstream conditions of the solar wind, and in two cases in situ observations of conditions in the magnetosphere from geosynchronous satellites. All three case studies were chosen because they occurred at nearly the same time of year, so photo-conductivity conditions in the ionosphere would have been very similar for all these events.

SMC Event 1 occurred on October 20, 2001, beginning at 14:26 UT and ending at 17:41 UT. This interval was selected by both the modified method of *O'Brien et al.* (2002) and the variable-AE selection method. Careful analysis of the AL index revealed that the steady convection criterion was problematic. As well, a substorm onset as identified by *Frey et al.* (2004) during SMC Event 1 also indicated that the steadiness requirement of *O'Brien et al.* (2002) may be flawed. During the interval IMF Bz fluctuated but on average was moderately negative at -2 nT, which is in agreement with past SMC studies (e.g. *DeJong and Clauer, 2005, O'Brien et al., 2002*). IMF By was positive and large at 7 nT. Based on SuperDARN measurements,

convection was enhanced during this event with a PCPD between 80 to 100 kV.

The second SMC case study occurred on October 30, 2001. Two SMC events were identified on this day using the new variable-AE selection method. The first started at 4:33 UT and ended at 7:47 UT . The second started at 8:23 UT and ended at 11:48 UT. These events would not have been identified by previous SMC methods, as the AE index was below 200 nT. Both intervals began with substorms. The first SMC event ended with a substorm while the second ended due to weak convection. IMAGE WIC data was only available for the first SMC event on this day but again indicated that the polar cap area was steady. The distance between voltage extrema also provided evidence that the polar cap area was steady during the second SMC event. The IMF Bz component was moderately negative at -3 nT with IMF By being positive at 5 nT. SuperDARN data indicated that convection was enhanced with the PCPD between 60 to 80 kV and a large convection electric field. The GOES satellite constellation made in situ measurements indicating that no large scale reconfiguration of the magnetotail occurred during these intervals. Conditions during this event were similar in nature to those of SMC event 1, but all quantities like PCPD and IMF magnitude were slightly smaller. This is not unexpected since the AE index for this event was smaller. The second case study exhibited all qualitative propagation of SMC, but was slightly weaker overall.

A case study of a sawtooth event was performed as well, with four individual “teeth” identified. This event was characterised by large fluctuations in the AE index. The polar cap area was not steady, as determined by IMAGE WIC observations and the distance between voltage extrema. The PCPD and the convection electric field were highly variable. IMF Bz and IMF By displayed large fluctuations with both components varying between 20 nT and -20 nT. ACE and GOES provided evidence suggesting that all four sawteeth on this day were triggered by variations in the solar wind. The sawtooth event was clearly different from the SMC intervals. The sawtooth event exhibited much stronger and more variable conditions.

## 8.2 Future Work

Work in this thesis was a first step towards understanding SMC in terms of global convection using SuperDARN. It is not an attempt to produce a SuperDARN definition of SMC; rather it is an evaluation of current SMC selection methods using observations of global convection by SuperDARN. Ideally, SMC events would be defined using observations of global convection. Because the SuperDARN convection mapping technique employs statistical convection patterns to constrain the fitting algorithms, one must be extremely cautious when attempting to quantify the steadiness of these convection patterns. It is this inherently steady model that may cause problems identifying SMC using SuperDARN. Before a SuperDARN definition of SMC is produced, work is required to deduce the properties of SMC seen by SuperDARN using convection maps where data, not models, dominate.

Interestingly the variable-AE SuperDARN SMC maps contained more data points on average than all other sets of events studied. Further investigation is required to determine if the SuperDARN data rate responds to the steadiness of the magnetospheric system during SMC.

The seasonal variations in ionospheric conductivity that affect AE are also expected to impact the “steadiness” criterion ( $dAL/dt \geq -25$  nT). This criterion is already problematic, since all it takes is one noisy data spike to cut short a SMC interval or even to preclude the selection of an interval. As well, there were issues with the reliability of the AL index due to poor magnetometer coverage. Modification of the AL criterion may also change the occurrence distribution that was used to develop the variable-AE cutoff function in Equation 5.2. Further refinement of the SMC criteria is essential.

Recall that on average the PCPD was generally lower in the northern summer months for SMCs selected using the modified method of *O’Brien et al. (2002)*. Since the uncertainties in the SuperDARN voltages are unknown further work is required to determine if this trend is actually significant. Further insight into the problem could be provided by calculating the average PCPD values for southern hemisphere

radars to see if the seasonal trend is reversed.

In addition to the seasonal effects, the number of SMC events is not found to be directly proportional to the sunspot number. The solar cycle peak may be related to the increased occurrence of magnetic clouds associated with coronal mass ejections, inside of which the IMF is usually steady. This behaviour requires further investigation.

*Bryant* (2008) studied substorms using an auroral power indicator. It is a calculation of energy deposited in the atmosphere by precipitating energetic auroral particles. It would be very interesting to apply this method to SMC studies, as bright and structured aurora is common during SMC intervals (*Henderson et al.*, 2006). This type of study could reveal if auroral particles were depositing energy steadily in the atmosphere as a whole, despite the large variability in brightness in localised areas.

## REFERENCES

- Ahn, B. H., H. W. Kroehl, Y. Kamide, and E. A. Kihn (2000), Seasonal and solar cycle variations of the auroral electrojet indices, *Journal of Atmospheric and Solar-Terrestrial Physics*, *62*, 1301–1310.
- Akasofu, S. I. (1964), The development of the auroral substorm, *Planetary and Space Science*, *12*, 273–282.
- Baumjohann, W., and R. Treumann (1996), *Basic Space Plasma Physics*, Imperial College Press, London.
- Belian, R. D., C. T. E., and G. D. Reeves (1995), Quasi-periodic, substorm associated, global flux variations observed at geosynchronous orbit, in *Space Plasmas: Coupling Between Small and Medium Scale Processes*, edited by M. Ashour-Abdalla, T. Chang, and P. Dusenbery, p. 143, AGU, Washington, D.C.
- Bilitza, D. (2001), International reference ionosphere 2000, *Radio Sci.*, *36*, 261–275.
- Bonetti, A., H. S. Bridge, A. J. Lazarus, B. Rossi, and F. Scherb (1963), Explorer 10 plasma measurements, *Journal of Geophysical Research*, *68*(13), 4017–4063.
- Brekke, A., and C. Hall (1988), Auroral ionospheric quiet summer time conductances, *Annales Geophysicae*, *6*(7), 361–376.
- Bryant, C. R. (2008), In-depth analysis of substorm recovery phase using electron and proton induced emissions from satellite observations, Ph.D. thesis, University of Calgary.
- Cai, X., M. G. Henderson, and C. R. Clauer (2006), A statistical study of magnetic dipolarization for sawtooth events and isolated substorms at geosynchronous orbit with goes data, *Annales Geophysicae*, *24*, 3481–3490.
- Cowley, S., J. Morelli, and M. Lockwood (1991), Dependence of convection flows and particle precipitation in the high-latitude dayside ionosphere on the x and y components of the interplanetary magnetic field, *Journal of Geophysical Research*, *96*, 5557–5564.
- Davis, T. N., and M. Sugiura (1966), Auroral electrojet activity index AE and its universal time variations, *Journal of Geophysical Research*, *71*(3), 785–801.
- DeJong, A. D., and R. Clauer (2005), Polar UVI images to study steady magnetospheric convection events: Initial results, *Geophysical Research Letters*, *32*, doi: 10.1029/2005GL024498.

- DeJong, A. D., X. Cai, R. C. Clauer, and J. F. Spann (2007), Aurora and open magnetic flux during isolated substorms, sawteeth, and SMC events, *Annales Geophysicae*, *25*, 1865–1876.
- Delouis, H., and P. Mayaud (1975), Spectral analysis of geomagnetic activity index aa over 103-year interval, *Journal of Geophysical Research*, *80*, 4681–4688.
- Dungey, J. W. (1961), Interplanetary magnetic field and the auroral zones, *Physical Review Letters*, *6*(2), 47–48.
- Elphinstone, R. D., J. S. Murphree, and L. L. Cogger (1996), What is a global auroral substorm?, *Reviews of Geophysics*, *34*(2), 169–232.
- Farrugia, C. J., F. T. Gratton, and R. B. Torbert (2001), Viscous-type processes in the solar wind-magnetosphere interaction, *Space Science Reviews*, *95*(1-2), 443–456.
- Feldstein, Y. I., and G. V. Starkov (1967), Dynamic of auroral belt and polar geomagnetic disturbances, *Planetary Space Science*, *15*, 209229.
- Frey, H. U., S. B. Mende, V. Angelopoulos, and E. F. Donovan (2004), Substorm observations by IMAGE-FUV, *Journal of Geophysical Research*, *109*, doi: 10.1029/2003JA010129.
- Fritz, T. A., and Q. G. Zong (2005), The magnetospheric cusps: A summary, *Surveys in Geophysics*, *26*, 409–414.
- Gauld, J. K., T. K. Yeoman, J. A. Davies, S. E. Milan, and F. Honary (2002), SuperDARN radar HF propagation and absorption response to the substorm expansion phase, *Annales Geophysicae*, *20*(16311645).
- Golsing, J. T., M. F. Thomsen, S. J. Bame, R. C. Elphic, and C. T. Russell (1990a), Plasma flow reversals at the dayside magnetopause and the origin of asymmetric polar cap convection, *Journal of Geophysical Research*, *95*, 8073.
- Gonzalez, A. L. C., W. D. Gonzalez, S. L. G. Dutra, and B. T. Tsurutani (1993), Periodic variation in the geomagnetic activity: A study based on the Ap index, *Journal of Geophysical Research*, *98*, 9215–9231.
- Gonzalez, W. D., B. T. Tsurutani, and A. L. C. D. Gonzalez (1999), Interplanetary origin of geomagnetic storms, *Space Science Reviews*, *88*, 529–562.
- Goodrich, C. C., T. I. Pulkkinen, J. G. Lyon, and V. G. Merkin (2007), Magnetospheric convection during intermediate driving: Sawtooth events and steady convection intervals as seen in Lyon-Fedder-Mobarry global MHD simulations, *Journal of Geophysical Research*, *112*.
- Greenwald, R. A., et al. (1995), DARN/SuperDARN: A global view of the dynamics of high-latitude convection, *Space Science Reviews*, *71*, 761–769.

- Henderson, M. G., G. D. Reeves, R. Skoug, M. F. Thomsen, M. H. Denton, S. B. Mende, T. J. Immel, P. C. Brandt, and H. J. Singer (2006), Magnetospheric and auroral activity during the 18 April 2002 sawtooth event, *Journal of Geophysical Research*, *111*, doi:10.1029/2005JA011111.
- Huang, C.-S., D. A. Andre, G. J. Sofko, and A. V. Kustov (2000), Super Dual Auroral Radar Network observations of ionospheric multicell convection during northward interplanetary magnetic field, *Journal of Geophysical Research*, *105*(A4), 7419–7428.
- Hughes, J. M., and W. A. Bristow (2003), Superdarn observations of the harang discontinuity during steady magnetospheric convection, *Journal of Geophysical Research*, *108*, doi:10.1029/2002JA009681.
- Hughes, W. J. (1995), The magnetopause, magnetotail, and magnetic reconnection, in *Introduction To Space Physics*, edited by M. G. Kivelson and C. T. Russell, chap. 9, pp. 227–284, Cambridge University Press.
- Hundhausen, A. J. (1995), The solar wind, in *Introduction To Space Physics*, edited by M. G. Kivelson and C. T. Russell, pp. 91–128, Cambridge University Press.
- Hunsucker, R. D., and J. K. Hargreaves (2003), *The High-Latitude Ionosphere and its Effects on Radio Propagation*, Cambridge Atmospheric and Space Science Series.
- Johnson, F. S. (1961), *Satellite Environment Handbook*, Stanford University Press, Stanford California.
- Kamide, Y., and S. Kokubun (1996), Two-component auroral electrojet: Importance for substorm studies, *Journal of Geophysical Research*, *101*(A6), 13,027–13,046.
- Kelley, M. C. (1989), *The Earth's Ionosphere: Plasma Physics and Electrodynamics*, Academic Press.
- Koskinen, H. E. J., R. E. Lopez, R. J. Pellinen, T. I. Pulkkinen, D. N. Baker, and T. Bösinger (1993), Pseudobreakups and substorm growth phase in the ionosphere and magnetosphere, *Journal of Geophysical Research*, *98*, 5801–5813.
- Luhmann, J. G. (1995), Ionospheres, in *Introduction To Space Physics*, edited by M. G. Kivelson and C. T. Russell, chap. 7, pp. 183–202, Cambridge University Press.
- McComas, D., S. Blame, P. Barker, W. Feldman, J. Phillips, P. Riley, and J. Griffiee (1998), Solar wind electron proton alpha monitor (SWEPAM) for the advanced composition explorer, *Space Science Reviews*, *86*, 563–612.
- McPherron, R. L. (1970), Growth phase of magnetospheric substorms, *Journal of Geophysical Research*, *75*, 5592–5599.
- McPherron, R. L. (1972), Substorm related changes in the geomagnetic tail: The growth phase, *Planetary Space Science*, *20*, 1521–1539.

- McPherron, R. L., T. P. O'Brien, and S. Thompson (2005), Solar wind drivers for steady magnetospheric convection, in *Multiscale Coupling of Sun-Earth Processes*, edited by A. T. Y. Liu, Y. Kamide, and G. Consolini, pp. 113–125, Elsevier B. V., Amsterdam, The Netherlands.
- McPherron, R. L., W. J. M., and H. T. S.) (2008), Response of the earth's magnetosphere to changes in the solar wind, *Journal of Atmospheric and Solar-Terrestrial Physics*, *70*, 303–315.
- McWilliams, K. A., et al. (2004), Simultaneous observations of magnetopause flux transfer events and of their associated signatures at ionospheric altitudes, *Annales Geophysicae*, *22*, 2181–2199.
- Mende, S., et al. (2000a), Far ultraviolet imaging from the IMAGE spacecraft: 1. system design, *Space Science Reviews*, *91*, 243–270.
- Mende, S., et al. (2000b), Far ultraviolet imaging from the IMAGE spacecraft: 2. wideband fuv imaging, *Space Science Review*, *91*, 271–285.
- O'Brien, T. P., S. M. Thompson, and R. L. McPherron (2002), Steady magnetospheric convection: Statistical signatures in the solar wind and AE, *Geophysical Research Letters*, *29*(7), 1130–1134.
- Parker, E. N. (1958), Dynamics of the interplanetary gas and magnetic fields, *Astrophysical Journal*, *128*, 664–676.
- Pytte, T., R. L. McPherron, E. W. Hones, and H. I. West (1978), Multiple-satellite studies of magnetospheric substorms: Distinction between polar magnetic substorms and convection driven negative bays, *Journal of Geophysical Research*, *83*, 663.
- Ruohoniemi, J. M., and K. B. Baker (1998), Large-scale imaging of high latitude convection with super dual auroral radar network hf radar observations, *Journal of Geophysical Research*, *103*(A9), 20,797–20,811.
- Ruohoniemi, J. M., and R. A. Greenwald (1996), Statistical patterns of high-latitude convection obtained from goose bay HF radar observations, *Journal of Geophysical Research*, *101*, 21,743–21,763.
- Russell, C. T. (1995), A brief history of solar-terrestrial physics, in *Introduction To Space Physics*, edited by M. G. Kivelson and C. T. Russell, chap. 1, pp. 1–26, Cambridge University Press.
- Russell, C. T., and R. L. McPherron (1973), Semiannual variations of geomagnetic activity, *Journal of Geophysical Research*, *78*(1), 92–107.
- Sergeev, V. A., R. J. Pellinen, and T. I. Pulkkinen (1995), Steady magnetospheric convection: A review of recent results, *Space Science Reviews*, *75*, 551–604.

- Smith, C., M. Acuna, L. Burlaga, J. LHeureux, N. Ness, and J. Scheifele (1998), The ACE magnetic fields experiment, *Space Science Reviews*, *86*, 611–632.
- Smith, E. J., B. T. Tsurutani, and R. L. Rosenberg (1978), Observations of interplanetary sector structure up to heliographic latitudes of 16-degrees - pioneer 11, *Journal of Geophysical Research*, *83*, 714 – 724.
- Svalgaard, L., E. W. Cliver, and A. G. Ling (2002), The semiannual variation of great geomagnetic storms, *Geophysical Research Letters*, *29*(16), doi: 10.1029/2001GL014145.
- Torr, M. R., et al. (1995), A far ultraviolet imager for the international solar-terrestrial physics mission, *Space Science Review*, *71*, 329–383.
- Walker, R. J., and C. T. Russell (1995), Solar-wind interactions with magnetized planets, in *Introduction To Space Physics*, edited by M. G. Kivelson and C. T. Russell, chap. 9, pp. 164–183, Cambridge University Press.
- Watanabe, M., G. Sofko, K. Kabin, R. Rankin, A. Ridley, C. Clauer, and T. Gombosi (2007), Origin of the interhemispheric potential mismatch of merging cells for interplanetary magnetic field B-Y-dominated periods, *Journal of Geophysical Research*, *112*, doi:10.1029/2006JA012179.
- Wolf, R. A. (1995), Magnetospheric configuration, in *Introduction To Space Physics*, edited by M. G. Kivelson and C. T. Russell, pp. 288–329, Cambridge University Press.